Clemson University
TigerPrints

All Dissertations | Dissertations

12-2012

Photo-thermal Processing of Semiconductor Fibers and Thin Films

Nishant Gupta
Clemson University, ngupta@g.clemson.edu

Follow this and additional works at: https://tigerprints.clemson.edu/all_dissertations

Part of the Electrical and Computer Engineering Commons

Recommended Citation

Gupta, Nishant, "Photo-thermal Processing of Semiconductor Fibers and Thin Films" (2012). *All Dissertations*. 1028.
https://tigerprints.clemson.edu/all_dissertations/1028

This Dissertation is brought to you for free and open access by the Dissertations at TigerPrints. It has been accepted for inclusion in All Dissertations by an authorized administrator of TigerPrints. For more information, please contact kokeefe@clemson.edu.

PHOTO-THERMAL PROCESSING OF SEMICONDUCTOR FIBERS AND THIN FILMS

A Dissertation
Presented to
the Graduate School of
Clemson University

In Partial Fulfillment
of the Requirements for the Degree
Doctor of Philosophy
Electrical Engineering

---

by
Nishant Gupta
December 2012

Accepted by:
Dr. Rajendra Singh, Committee Chair
Dr. Michael A. Bridgwood
Dr. W. Rod Harrell
Dr. Mica Grujicic

ABSTRACT

Furnace processing and rapid thermal processing (RTP) have been an integral part of several processing steps in semiconductor manufacturing. The performance of RTP techniques can be improved many times by exploiting quantum photo-effects of UV and vacuum ultraviolet (VUV) photons in thermal processing and this technique is known as rapid photo-thermal processing (RPP). As compared to furnace processing and RTP, RPP provides higher diffusion coefficient, lower stress and lower microscopic defects. In this work, a custom designed automated photo assisted processing system was built from individual parts and an incoherent light source. This photo-assisted processing system is used to anneal silica clad silicon fibers and deposit thin-films. To the best of our knowledge, incoherent light source based rapid photo-thermal processing (RPP) was used for the first time to anneal glass-clad silicon core optical fibers. X-ray diffraction examination, Raman spectroscopy and electrical measurements showed a considerable enhancement of structural and crystalline properties of RPP treated silicon fibers. Photons in UV and vacuum ultraviolet (VUV) regions play a very important role in improving the bulk and carrier transport properties of RPP-treated silicon optical fibers, and the resultant annealing permits a path forward to in situ enhancement of the structure and properties of these new crystalline core optical fibers.

To explore further applications of RPP, thin-films of Calcium Copper Titanate ($CaCu_3Ti_4O_{12}$) or CCTO and Copper (I) Oxide (Cu_2O) were also deposited using photo-assisted metal-organic chemical vapor deposition (MOCVD) on Si/SiO_2 and n-Si

substrate respectively. CCTO is one of the most researched giant dielectric constant materials in recent years. The given photo-assisted MOCVD approach provided polycrystalline CCTO growth on a SiO_2 surface with grain sizes as large as 410 nm. Copper (I) oxide (Cu_2O) is a direct band gap semiconductor with p-type conductivity and is a potential candidate for multi-junction solar cells. X-ray diffraction study revealed a preferred orientation, as (200) oriented crystals of Cu_2O are grown on both substrates. Also, electrical characterization of Cu_2O/n-Si devices showed the lowest saturation current density of $1.5x10^{-12}$ A/cm^2 at zero bias. As a result, photo-assisted thermal processing has the potential of making the process more effective with enhanced device performance.

DEDICATION

To my parents, without whose blessings, love and encouragement this task would have been impossible.

ACKNOWLEDGMENTS

I would like to express my deepest gratitude and appreciation to my advisor Dr. Rajendra Singh for his sincere guidance and support throughout my studies at Clemson University. He continually and convincingly conveyed a spirit of adventure in regard to research and scholarship, and an excitement in regard to teaching. Without his guidance and persistent help this dissertation would not have been possible.

I am thankful to Dr. Kelvin F. Poole, who lent invaluable support and advice on various technical issues. I would also like to thank Dr. Michael A. Bridgwood and Dr. Mica Grujicic for serving in my committee and his valuable inputs. I thank Dr. William R. Harrell for allowing me to use his laboratory for electrical measurements and for serving on my committee. I am also thankful to Dr. James E. Harriss for his continuous help and valuable discussions. I wish to thank Dr. Colin McMillen for his help in XRD measurements and study. I would like to thank respective research group of Dr. John Ballato (Silicon Fibers), Dr. A. M. Rao (Micro Raman Spectroscopy), and Dr. Shiou-Jyh Hwu (UV-Vis-NIR Spectroscopy) form Clemson University, Dr. Jagdish Narayan from NCSU (Transmission Electron Microscopy), and Dr. Glenn Teeter from NREL (Secondary Ion Mass Spectrometry) for measurements and analysis of my samples. I would also like to thank John Hicks and other staff members of ECE department for their help and time.

I am also thankful to my friends for keeping me in good humor throughout my stay at Clemson. Finally, I would like to express my deep felt gratitude to my wife

Priyanka for her constant encouragement and patience. I am also in debt to my family and each individual who helped in this dissertation.

TABLE OF CONTENTS

Page

TITLE PAGE i

ABSTRACT ii

DEDICATION iv

ACKNOWLEDGMENTS v

LIST OF TABLES ix

LIST OF FIGURES x

CHAPTER

I. INTRODUCTION 1

1.1 Techniques Used to Process Semiconductor Materials 1
1.2 Rapid Photo-thermal Processing 4
References 6

II. PHOTO ASSISTED THERMAL PROCESSING SYSTEM 10

2.1 Introduction 10
2.2 Photo-assisted Chemical Vapor Deposition 10
2.3 Theory of Photo-assisted Thermal Process 11
2.4 Photo-assisted Thermal Processing System 12
2.5 Evaporation of Metal Contacts 18
2.6 Results and Discussion 20
2.7 Conclusion 20
References 21

III. ANNEALING OF SILICON FIBERS 28

3.1 Introduction 29
3.2 Experimental 30
3.3 Results and Discussion 35
3.4 Conclusion 41
References 42

Table of Contents (Continued)

Page

IV. PHOTO-ASSISTED METAL-ORGANIC CHEMICAL VAPOR DEPOSITION OF HIGH DIELECTRIC CONSTANT THIN FILM 50

4.1 Introduction 50
4.2 Experimental Details 52
4.3 Results and Discussion 57
4.4 Conclusion 64
References 65

V. DEPOSITION AND CHARACTERIZATION OF NANOSTRUCTURED Cu_2O THIN-FILM FOR POTENTIAL PHOTOVOLTAIC APPLICATIONS 89

5.1 Introduction 89
5.2 Background Material 90
5.3 Experimental Details 92
5.4 Results and Discussion 95
5.5 Conclusion 99
References 100

VI. CONCLUSION 117

APPENDIX A: LabVIEW Automation 119

LIST OF TABLES

Table Page

4.1 Published Results at room temperature (300K) and 1KHz.......................... 69

4.2 Process gas and precursor oven parameters for sample P97........................ 70

4.3 Process parameters for the devices shown in Figure 4.4 71

4.4 Process parameters for sample P79 and P80... 72

4.5 Comparison of precursor flow rates used in various samples...................... 73

4.6 Capacitance measurements for P47C5P6 74

4.7 Adjusted capacitance for P47C5P6... 75

4.8 Capacitance calculations and measurements for Al/SiO_2/Si/SiO_2/Al structure.. 76

4.9 Capacitance measurements for Al/CCTO/SiO_2/Si/SiO_2 /CCTO/Al structure for (a) P94 and (b) P96... 77

LIST OF FIGURES

Figure Page

1.1 Spectrum comparison of various processing techniques 8

1.2 Reduced Activation Energy and Processing Temperature with RPP 9

2.1 Radiation energy as a function of light source frequency........................... 22

2.2 Boroelectric® heater 23

2.3 Effect of temperature on PG resistivity 24

2.4 Drawing of stainless steel heater holder 25

2.5 UV lamp connections to power supply and trigger transformer................. 26

2.6 MFCs setup configuration for 647B multi gas controller........................... 27

3.1 RPP system employed in this work for the ex-situ annealing of glass-clad silicon optical fibers 45

3.2 Longitudinal x-ray measurements for the as-drawn fiber (a) and RPP treated fiber (b).. 46

3.3 X-ray crystallography results at the same location (3 mm relative location) of silicon optical fiber 47

3.4 Schematic of the silicon optical fiber showing the locations where Raman spectra were collected 48

3.5 Current-voltage (I-V) characteristics for the Schottky barrier diode using as drawn and annealed fiber 49

4.1 Spectrum of Xenon Flash Lamp used in Photo-assisted MOCVD system.. 78

4.2 Photo-assisted MOCVD Process setup with computer control 79

4.3 Thermal cycle for the CCTO photo-assisted MOCVD process.................. 80

List of Figures (Continued)

Figure Page

4.4 Leakage current, typical capacitance vs. deposition time for the films deposited on silicon wafer with structure Al/Si/film/Al 81

4.5 XRD analysis of films deposited on silicon substrate 82

4.6 Comparison of XRD patterns of various samples 83

4.7 XRD for the CCTO thin film from sample P97 84

4.8 SEM image of the CCTO thin film 85

4.9 Electrical measurements setup and I-V characteristics 86

4.10 XRD for the thin film deposited on $Si/SiO_2/Pt$ (sample P98) 87

4.11 The effect of charging current in measurement of capacitance using DC method 88

5.1 Experimental set up of MOCVD system used for the deposition and in situ annealing of Cu_2O films 104

5.2 Process flow for Cu_2O thin film deposition on silicon and quart substrate 105

5.3 XRD pattern of the Cu_2O film deposited on n-Si substrate and quartz substrate 106

5.4 (a) Absorbance spectra of Cu_2O thin film deposited on quartz wafer; (b) $(\alpha \cdot h\nu)^2$vs. energy plot for optical band gap calculations. 107

5.5 Bright-field Cross-section TEM image of the individual islands 108

5.6 Size distribution Cu_2O islands/grains 109

5.7 Polycrystalline grains 110

5.8 Normalized SIMS depth profile for CO41 and C042 devices 111

List of Figures (Continued)

Figure Page

5.9 Comparison of J-V characteristics of Au-nSi device (Schottky diode) and Cu2O-nSi device.. 112

5.10 Current density-voltage (J-V) characteristics of Cu_2O/n-Si devices deposited at various substrate temperature.. 113

5.11 Effect of annealing time on Cu_2O/n-Si devices deposited at 750ºC and annealed in-situ at 500ºC... 114

5.12 J-V characteristic of the Cu_2O/p-Si samples... 115

5.13 Comparison of dark J-V characteristics of Cu_2O/n-Si diodes literature data [34, 35] and present work................................ 116

AX.1 Front panel of the ultimatereaderwithcontrol.vi 122

AX.2 Front panel of precursor delivery line heater control VI 123

AX.3 Front panel of UV lamp control with timer VI... 124

AX.4 Front panel of precursor deposition cycle VI for CCTO and Cu_2O.. 125

AX.5 Front panel of oxygen annealing VI 126

CHAPTER ONE

INTRODUCTION

In this chapter, we will review motivation behind the work presented in the thesis. Several techniques have been developed to process semiconductor devices and materials. Historically, furnace processing has been used in all over semiconductor industry. The main disadvantage of the furnace processing is high thermal budget which results in unwanted stress, defects, reliability issues etc. To overcome the disadvantages associated with furnace processing, industry adopted rapid thermal processing (RTP) which uses both furnace and incoherent light source based isothermal processing [1]. At present, single wafer RTP is used widely and has become one of the key processing techniques in the fabrication of semiconductor manufacturing because of faster wafer processing with excellent control of thermal budget. Due to the incoherent light, RTP has distinct effect on properties of the processed material. RTP systems can be designed to fully exploit quantum photo effects in a processing technique called rapid photo-thermal processing [2]. In this chapter, the advantages of photo-assisted processing have reviewed in comparison with other techniques used to process materials. At the end of the chapter, a brief description of each chapter has been given.

1.1 Techniques Used to Process Semiconductor Materials

1.1.1 Solid State Synthesis

Typical solid state reaction synthesis utilizes fine grain powders of starting reactants and this mixes them in ball mill grinders for hours. This mixing is followed by high temperature firing. The end product is generally in the form of a powder. This powder is further pelletized to perform electrical characterization. The advantage of solid state synthesis is lower cost and easy experiment setup. There are some inherent disadvantages from electronic application point of view which include chemical non-uniformity, large particle size and impurities introduced from ball milling. Also, this synthesis method cannot be used directly to deposit thin film of material.

1.1.2 Sputtering

Sputtering is one of the most common methods employed to deposit thin film on various substrates. Typical sputtering process uses a target of the material to be deposited and a source of charged particles. When bombarding charge particles and atoms of the target collide, atoms from the target are released on substrate due to exchange of momentum between the two. One of the major advantages of sputtering is that almost any material can be deposited as a film. But, thin film deposited with sputtering are found to result in poor step coverage, contamination and defects [3]. High temperature annealing is also required after the deposition. Several different energy sources such as dc, ac, magnetron, plasma, are being used to produce charged particles.

1.1.3 Pulsed LASER Deposition (PLD)

Since the invention in 1957, LASERs have been used in several applications. PLD uses a high power LASER beam housed in a vacuum chamber. The LASER beam is first focused and then pulsed on the target of desired material. The advantage of PLD over sputtering is lower contamination because the process is performed in a vacuum. But such as in sputtering, this technique requires a high temperature annealing after deposition to achieve the desired properties of the film. Some researchers also used a target prepared with solid state reaction for sputtering or PLD [4, 5]. As discussed before, high temperature processing may result in defects due to stress.

1.1.5 Chemical Vapor Deposition (CVD)

CVD has proven itself the most reliable and efficient process for thin film deposition of various materials in semiconductor manufacturing. CVD can be categorized depending on working pressure, physical nature of precursors, energy source etc. A typical CVD process requires heating the substrate temperature to such an extent that it can provide sufficient energy to start the reactions between precursors. For the very first time, Singh et al. exploited the advantages of photo-assisted CVD in their work published in 1991 [6]. Photon assisted CVD uses high energy photons in conjunction with low thermal energy to provide sufficient energy for the process and replaces the need for high thermal energy or high temperature. This combination of thermal and photo energy provide enough energy to complete the process at lower temperatures which results in high purity and improved performance material.

1.2 Rapid Photo-thermal Processing

In several areas of semiconductor manufacturing, rapid photo-thermal processing (RPP) has proved itself a superior technique for depositing dielectric thin films with very low leakage current, low defect density and good reliability at a low thermal budget [7-10]. This unique processing technique uses photo energy as an additional source of energy with thermal energy. From the electromagnetic spectrum, only the photons with wavelength more than about 800 nm contribute to thermal effects by increasing the vibration amplitude of the atoms which is the basic mechanism in furnace processing; while photons between 400 nm and 800 nm contribute to both thermal and quantum effects as shown in Figure 1.1 [11]. Photons with wavelength less than 400 nm provide a large number of electronic excited states which leads to stretched bonds and reduced activation energy and results in lower process temperature and cycle time as shown in Figure 1.2. Quantum effects have the following implications for the photo-assisted CVD process [12];

1. The bulk and surface diffusion coefficients are increased for a given temperature in processing.
2. The processing cycle time is reduced.
3. Due to lower microscopic defects, higher performance, better reliability and yield are achieved.

In chapter two, the details of the photo-assisted thermal processing system have been provided. I have discussed details of all the main components and described the

basic operation of the system. A brief description of automation of the system is also given in the chapter.

Chapter three is Ref [13]. This chapter describes photo-assisted annealing and characterization of silica clad silicon core fiber. The recent realization of silicon core optical fibers has the potential for novel low insertion loss rack-to-rack optical interconnects and a number of other uses in sensing and biomedical applications. The processed and unprocessed fibers were characterized with X-ray diffraction, Raman spectroscopy and the dark current-voltage by fabricating Schottky diode.

In chapter four, description of photo-assisted MOCVD of $CaCu_3Ti_4O_{12}$ (CCTO) thin film is presented. Calcium copper titanate ($CaCu_3Ti_4O_{12}$) or CCTO is one of the most researched giant dielectric constant materials in the recent years. The given photo-assisted MOCVD approach provided polycrystalline CCTO growth over a SiO_2 surface. Powder X-ray diffraction (XRD) and scanning electron microscopy (SEM) were performed to analyze structural and compositional properties of the CCTO thin film. Ellipsometric measurements indicated a refractive index of 3.03 of CCTO thin film.

Chapter five describes the deposition and characterization of copper (I) oxide thin-films. Copper (I) oxide or Cu_2O is a direct band gap semiconductor with p-type conductivity and is a potential candidate for multi-junction solar cells. Thin-films of Cu_2O are deposited using photo-assisted MOCVD on n-Si and quartz substrate. X-ray diffraction, UV-Vis-NIR spectroscopy, SIMS, TEM, and electrical characterization were used to study properties of Cu_2O thin-films.

References

[1] R. Singh, "Rapid isothermal processing", J. Appl. Phys., vol. 63, issue 8, pp. R59, 1988.

[2] R. Singh, S. V. Nimmagadda, V. Parihar, Y. Chen and K. F. Poole, "Role of rapid photothermal processing in process integration", IEEE Trans. Electron Devices, vol. 45, issue 3, pp. 643-654, 1998.

[3] D. M. Mattox, "Vacuum deposition processes equipment and applications", www.kolzer.com, 2004.

[4] A. Tselev, C. Brooks, S. Anlage, H. Zheng, L. Salamanca-Riba, R. Ramesh and M. Subramanian, "Evidence for power-law frequency dependence of intrinsic dielectric response in the CaCu3Ti4O12", Physical Review B, vol. 70, issue 14, article no. 144101, 2004 .

[5] M. Subramanian, "High dielectric constant in ACu3Ti4O12 and ACu3Ti3FeO12 phases", Journal of Solid State Chemistry, vol. 151, issue 2, pp. 323-325, 2000.

[6] R. Singh, S. Sinha, R. P. S. Thakur and N. J. Hsu, "Role of photoeffects in integrated rapid isothermal processing", MRS Proceedings, vol. 224, pp. 197, 1991.

[7] R. Singh and Y. Chen, "Role of high energy photons in dual spectral source rapid isothermal CVD", J Electron Mater, vol. 26, issue 10, pp. 1184 – 1188, 1997.

[8] Y. Chen, R. Singh, G. Li and G. H. Haertling, "A study of rapid photothermal annealing of sputtered lead lanthanum zirconia titanate thin films", J. Electrochem. Soc., vol. 145, issue 12, pp. 4317-4322, 1998.

[9] Y. Chen, R. Singh and J. Narayan, "Deposition of tantalum oxide films by dual spectral source assisted metalorganic chemical vapor deposition (MOCVD)", J Electron Mater, vol. 26, issue 4, pp. 350-354, 1997.

[10] A. Venkateshan, R. Singh, K. F. Poole, J. Harriss, H. Senter, R. Teague and J. Narayan, "High- gate dielectrics with ultra-low leakage current for sub-45 nm CMOS", Electron. Lett., vol. 43, issue 21, pp. 1130, 2007.

[11] R. Singh, R. Sharangpani, K. C. Cherukuri, Y. Chen, D. M. Dawson, K. F. Poole, A. Rohatgi, S. Narayanan and R. P. S. Thakur, "How Rapid Isothermal Processing Can be a Dominant Semiconductor Processing Technology in the 21st Century", MRS Proceedings, vol. 429, 81, 1996.

[12] R. Singh, M. Fakhruddin and K. F. Poole, "Rapid photothermal processing as a semiconductor manufacturing technology for the 21st century", Appl. Surf. Sci., vol. 168, issue 1-4, pp. 198-203, 2000.

[13] N. Gupta, C. McMillen, R. Singh, R. Podila, A. M. Rao, T. Hawkins, P. Foy, S. Morris, R. Rice, K. F. Poole, L. Zhu, and J. Ballato, "Annealing of silicon optical fibers", J. Appl. Phys., vol. 110, 093107, 2011.

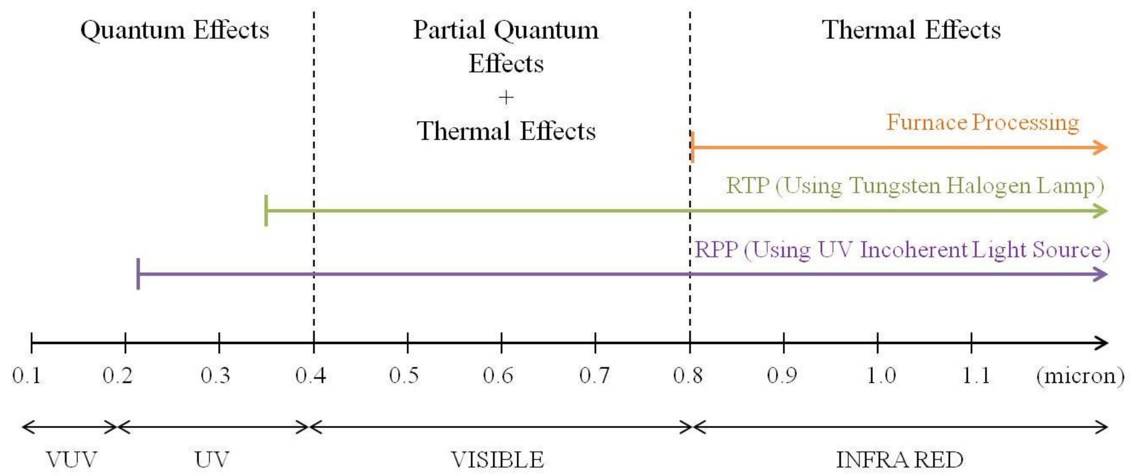

Figure 1.1: Spectrum comparison of various processing techniques [2]

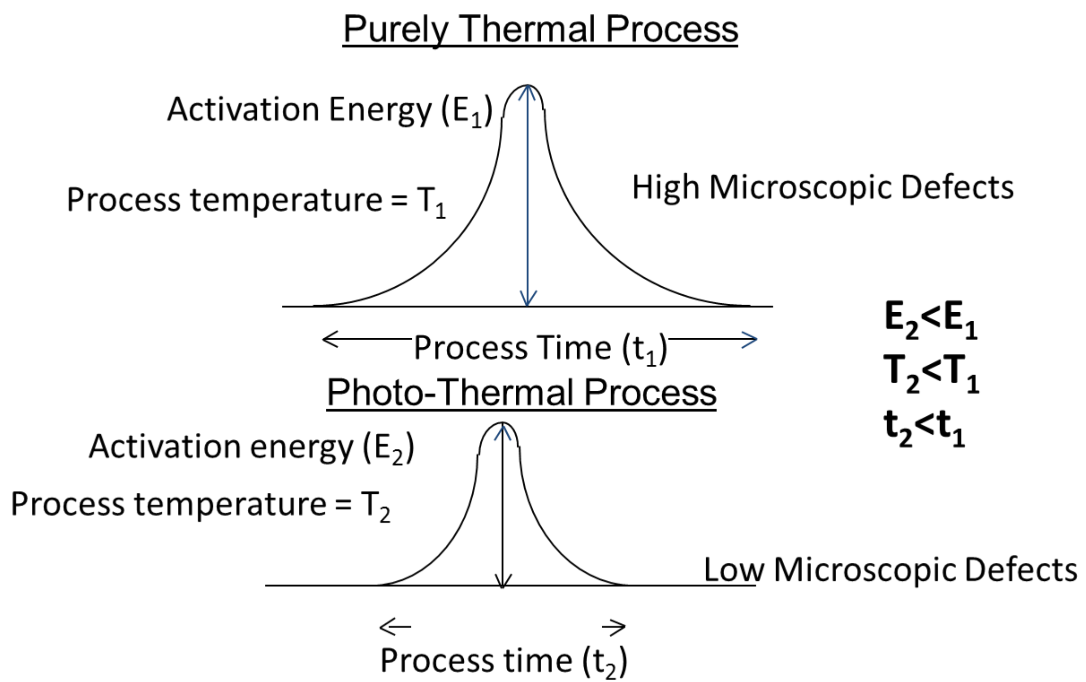

Figure 1.2: Reduced Activation Energy and Processing Temperature with RPP [2]

CHAPTER TWO

PHOTO ASSISTED THERMAL PROCESSING SYSTEM

2.1 Introduction

As discussed in the previous chapter, photo-assisted thermal processing has its unique advantages over thermal only processing. The system described in this chapter is custom designed home built system. This system is also previously used for atomic layer deposition of high κ dielectrics [1, 2]. The major advantage of this tool is that it can perform all the three processing steps, high temperature cleaning, deposition, and annealing; in-situ. The system was modified as required by the three processes described in Chapter 3, 4 and 5. However, overall configuration and operating procedure remains same. There are big advantages found between automated and manual process control. Therefore, the system is automated with LabVIEW modules. Separate LabVIEW modules were used for controlling UV radiation, deposition process and annealing. The system is also equipped with a diffusion pump which provides the capability to work in Ultra High Vacuum (UHV). However, diffusion pump is not used in this work.

2.2 Photo-assisted Chemical Vapor Deposition

Chemical Vapor Deposition (CVD) has been used for long time in semiconductor industry for producing high purity, high performance thin film of different materials. The basic concept behind the CVD is the reaction and/or decomposition of vapors of reactant materials over the heated substrate (wafer) to produce thin film of desired material.

Deposited film can be crystalline, poly-crystalline or amorphous depending on processing conditions. The substrate temperature is a critical parameter in the CVD process. The substrate temperature should be high enough to decompose the precursor vapors into its reactive component in order for a reaction to take place between the reactants.

The precursors used in the process can be elemental or compound. In this work, compound precursors were used. The major disadvantage with elemental precursors is low vapor pressure as compared to compound precursors. In given CVD process, compound precursors (AX and BY) were heated in respective ovens and transported to the heated substrate with the help of a carrier gas, where they react in the presence of a reactant gas (C) and make desired compound ABC. The stoichiometric composition of ABC can also be controlled by changing the flow rates of carrier gas. The example will be shown in Chapter 4.

2.3 Theory of Photo-assisted Thermal Process

Key to this unique processing technique is the use of UV radiation as an additional source of energy in conjunction to the thermal energy. To explain this phenomenon theoretically, the thermal power of radiation needs to be studied which is given by [3]

$$P = hf\Delta f\left\{\frac{1}{e^{hf/kT}-1}+\frac{1}{2}\right\}$$

Where, Δf is the frequency band occupied by the radiation mode, h is Planck's constant, k is Boltzmann constant, T is absolute temperature. The two parts of the above equation are plotted in Figure 2.1 (Δf=1 and T=300 K). The factor 1/2 in the above equation is due to the contribution of zero point energy. Zero point energy is the lowest possible energy of quantum mechanical physical system and is a quantum phenomenon. The other factor inside the curly bracket is the Bose–Einstein factor, which is the thermal part of the radiation. It is apparent from Figure 2.1 that in the lower frequency (higher wavelength) range, the thermal part is dominant but as the frequency goes up, quantum part of the energy dominates. Also in the past, Singh et al. has shown that only the photons with wavelength more than ~800 nm contribute to thermal effects, while photons between 400 nm and 800 nm contribute to both thermal and quantum effects [4]. Photons with wavelength less than 400 nm provide only quantum effects without any undesirable effect.

2.4 Photo-assisted Thermal Processing System

A general overview of photo-assisted thermal processing system used in this work is given in this section. The discussion of photo-assisted thermal processing system is divided into following sub-sections.

- Vacuum System
- Substrate Heating System
- UV and VUV Source
- Precursor Ovens and Control Valves

- LabVIEW Automation
- Mass Flow Controllers (MFCs) for Gas Flow Control

2.4.1 Vacuum System

As mentioned before, ultra high vacuum can be achieved in the system with the help of 6" Varian diffusion pump (Model type number: VHS-6, 0184) and Stoke's rotary vane pump (Special service, model: 900-013-241) roughing pump. But in this study, only Stoke roughing pump has been used for all processing steps. The main processing chamber is custom made stainless steel chamber with capability to house two UV lamps, gas inlets, high vacuum valve and roughing pump opening. Main processing chamber was also equipped with a quartz viewing window. The heater used the system could be mounted by two ways into the chamber either from the side opening or from the bottom opening as shown in Figure. In this work, heater was mounted from the side opening.

2.4.2 Substrate Heating System

Substrate heating system is a very critical part of the system. It consists of three components, substrate heater with connectors, power supply, and k-type thermocouple. The selection of heater for this system considers several points like maximum operable temperature, time to achieve maximum temperature, stability of heater material at high temperatures, etc. Heater used in this system is Boraelectric® heater manufactured by Momentive Performance Materials Inc and cataloged as HTR1002 or item# 2110071 as shown in Figure 2.2. The heater is made of two materials, one of them is a high purity

insulator called pyrolytic boron nitride (PBN) and other is thin-film (~ 50µ) of a conductor called pyrolytic graphite (PG) [5]. Both materials have unique electrical, chemical and thermal properties at high temperatures. Also due to unique thermal conductivity and anisotropy of both materials, heater provides excellent thermal uniformity over the substrate. The heater has an ultra fast response and power outputs that can exceed 300 watts/sq. inch (45 watts/ sq. cm) while losses to power leads and mechanical support components can be 20-30 watts each [6]. The resistivity of the PG conductive film in Boraelectric® heater decreases with temperature to about 40% of the room temperature value at around 1200ºC as shown in Figure 2.3. Since resistance decreases at higher temperatures, current also increases for given voltage. The advantage of this property is that high temperature can be achieved at lower voltage. Since the current at temperature of 900ºC is more than 10 Amps, a high current variac (15 Amps) is used to operate the heater in this work. Also, it is important to use low mass and fast response thermocouple which can quickly read the heater temperature. Therefore in this system, a bare wire 0.1" diameter k-type thermocouple is used with a temperature readout manufactured by Omega.

The heater is mounted on a custom designed stainless steel holder as shown in Figure 2.4. For the power connection, molybdenum nuts and bolts are used to connect the heater to the power lines with poly graphite (PG) washers to make low resistance connection between PG film and molybdenum nuts.

2.4.3 UV-VUV Source

A fused quartz arc lamp manufactured by Xenon corporation (part number: 890-1723) was used as UV-VUV source. To operate the lamp, a power supply RC-500 Pulsed UV curing system with a trigger transformer (TR-2081) was used. This lamp is 10” straight lamp and custom made for the system used in this work. The connection diagram for the lamp is shown in Figure 2.5. The UV-VUV source was controlled with LabVIEW as per requirement of the process.

2.4.4 Precursor Ovens and Control Valves

Each precursor was kept on a ceramic boat (Sigma-Aldrich Z247014-1EA) in individual precursor oven. A conflat “Tee” manufactured by Kurt J. Lesker (part# T-0275) was used as the precursor oven. The heating tapes (Omega STH051-040) were wrapped on the outer side of the precursor oven to heat the precursor to desired temperature. Also, precursor ovens were covered with aluminum foil to insulate them from outer environment and achieve higher temperature. In order to maintain desired vapor pressure of the precursor, a k-type thermocouple was used to control temperature inside the oven. The heating system on the ovens was controlled and monitored with LabVIEW module and will be discussed in detail later in appendices. A 316L stainless steel tube was connected directly to the chamber port for the delivery of the precursor, with the carrier gas line connecting to the top of the tee. The delivery line to the chamber was also heated (with tape heaters) and maintained at the temperature using LabVIEW to

prevent the gas from condensing along the wall of the tubing. A pneumatic ball valve was installed with this line for controlled operation through LabVIEW.

Three types of valves were mainly used in the system solenoid valve, pneumatic valve and manual ball valve. Solenoid valves and pneumatic valves are controlled by LabVIEW modules through solid-state relays (SSR).

2.4.5 LabVIEW Automation

LabVIEW is the most popular system design software with the tools required to create and deploy measurement and control systems through unique hardware integration [7]. LabVIEW stands for of Laboratory Virtual Instrumentation Engineering Workbench, uses a graphical language known as "G". LabVIEW initially developed for Apple Macintosh in 1986 but in later years, it was released for almost of all the operating systems. A major advantage of LabVIEW compared to other development environments is the extensive support for accessing measurement instruments and hardware. Drivers and abstraction layers for various instruments and busses are included with the package or available to add as required. The abstraction layers and driver interfaces make program development much faster as compared to other similar programs. Several libraries with a large number of functions for data acquisition, signal generation, mathematics, statistics, signal conditioning, analysis, etc., along with numerous graphical interface elements are provided in several LabVIEW package options [8].

LabVIEW has been very helpful in automation of the system. Control of temperature precursor ovens and delivery lines, valve control and deposition and

annealing cycle control was done through LabVIEW for reducing manual error. The user interface was designed to input new process parameters into the experiment as required. LabVIEW modules will be discussed in detail in appendix A.

2.4.6 Mass Flow Controllers (MFCs) for Gas Flow Control

Gas flow was controlled by individually calibrated MKS mass flow controllers (MFCs). Each MFC was further controlled using 647B MKS multi gas controller. 647B has eight channels and can be used to control eight different MFCs simultaneously or independently connected to each channel. Figure 2.6 shows details of MFCs connected to each channel. Since each process i.e. in-situ cleaning, deposition and in-situ annealing, uses different gas flow rates, it is tedious to control MFCs manually for each cycle. Therefore, 647B was interfaced using RS232 serial port with LabVIEW module to update gas flow set points and turning on-off each MFC during each cycle. Prior to interfacing with LabVIEW, 647B was setup for individual MFC by its range, calibrated gas and calibration coefficient etc. Following gases were used in typical processes developed during this work

1. Ultra High Purity (UHP) Nitrogen gas as carrier gas
2. Forming gas (80% UHP N_2 and 20% UHP H_2) for cleaning
3. Oxygen (UHP) as a reaction and annealing gas
4. Nitrous oxide gas as reaction gas

2.5 Evaporation of Metal Contacts

For electrical characterization, metal contacts were evaporated on the processed sample as required. Edward metal evaporator was used to evaporate required metal on the sample by suing shadow masks. Typical procedure to operate Edward metal evaporator is as following.

1. Turn on rotary pump.
2. Turn gauges ON.
3. Turn water chiller ON. Typical set point of water chiller is 15ºC.
4. When pressure on gauge 3 reaches below $3x10^{-03}$ torr, open backing valve.
5. Turn the diffusion pump ON and note the time. Typical warm up time for the diffusion pump heater is 30min.
6. Open the air admittance valve to bring the evaporation chamber to the atmosphere pressure.
7. Wait until whistle sound stops.
8. Remove outer plastic implosion guard of the bell and then remove the bell jar.
9. Remove the shields.
10. Check for the desired filament installed.
11. Load the filament with metal load.
12. Place the shadow mask and adjust the height of the mask as required.
13. Place the sample on the shadow mask.
14. Close the bell jar.
15. Place the shields back and then place the bell jar and implosion guard.

16. Close the backing valve and open the roughing valve. If the critical time has passed by now, the roughing valve can be kept open when the backing valve is closed for a period of 5min, if not then it can be kept open for a period of 2min.
17. When reading on gauge 2 is below $5x10^{-02}$ torr, turn OFF the roughing valve and open the backing valve.
18. Open the high vacuum valve slowly keeping the gauge 3 reading in 10^{-02} torr range.
19. Wait to reach standard pressure for evaporation i.e. $5x10^{-06}$ torr, on gauge 1.
20. Check shorting plug is in-place and variac is set at zero.
21. Turn ON the variac and perform the evaporation.
22. After evaporation, wait for few minutes to reach the pressure on the gauge 1 below $5x10^{-06}$ torr.
23. Close the high vacuum valve.
24. Open air admittance valve and bring the evaporation chamber to the atmosphere pressure.
25. Open the bell jar and remove the sample.
26. To shutdown the evaporator, close the bell jar and pump down the evaporator to $5x10^{-05}$ torr.
27. Close the backing valve and turn OFF diffusion pump, roughing pump, gauges and water chiller.

2.6 Results and Discussion

Using the photo-assisted thermal processing system described above was used to anneal silicon core silica fiber, deposit CCTO and Cu_2O thin film. The results obtained in each case will be discussed in subsequent chapters 4 and 5 respectively.

2.7 Conclusion

The system developed during this work was used to deposit high quality film CCTO and Cu_2O. The same system was also used to anneal silicon core silica clad fiber. RPP annealed silicon core silica fibers have shown enhanced structural and electrical properties as compared to thermal only annealed fiber.

References

[1] M. Fakhruddin, “Processing and Characterization of high performance gate dielectric materials by rapid photothermal process based atomic layer deposition system”, PhD Dissertation, Clemson University, Aug. 2003.

[2] A. Venkateshan, “Manufacturable process and tool for high performance metal/high-k gate dielectric stacks for sub-45 nm CMOS & related devices”, PhD Dissertation, Clemson University, Dec. 2003.

[3] R. Singh, M. Fakhruddin and K. F. Poole, “Rapid photothermal processing as a semiconductor manufacturing technology for the 21st century”, Appl. Surf. Sci., vol. 168, issue 1-4, pp. 198-203, 2000.

[4] R. Singh, R. Sharangpani, K. C. Cherukuri, Y. Chen, D. M. Dawson, K. F. Poole, A. Rohatgi, S. Narayanan and R. P. S. Thakur, “How Rapid Isothermal Processing Can be a Dominant Semiconductor Processing Technology in the 21st Century”, MRS Proceedings, vol. 429, 81, 1996.

[5] Momentive Materials, Available: http://momentive.com/Products/Main.aspx?id=22821&terms=heater.

[6] Boralectric heating elements, Available: http://www.tectra.de/heater.htm.

[7] LabView, Available: http://www.ni.com/labview/.

[8] LabView, Available: http://en.wikipedia.org/wiki/LabVIEW.

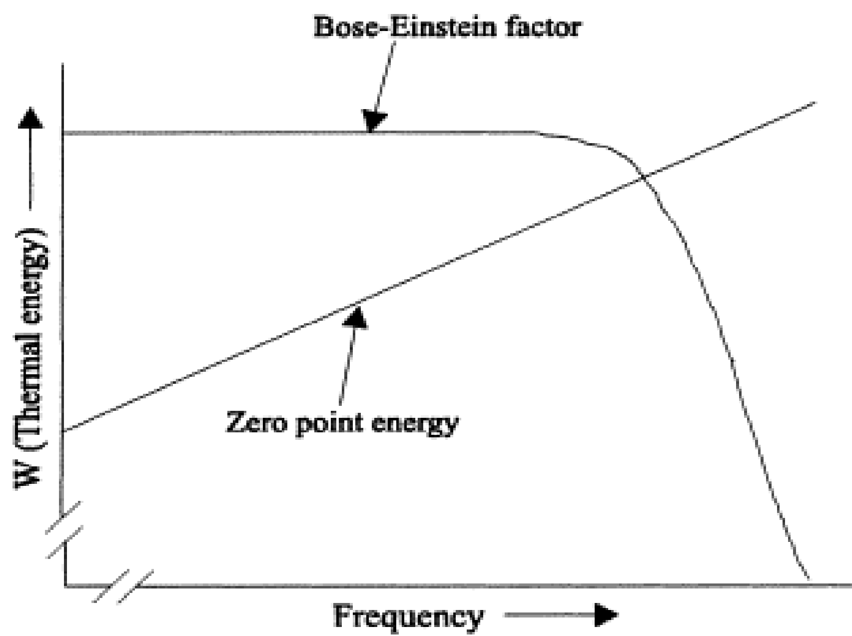

Figure 2.1: Radiation energy as a function of light source frequency [3]

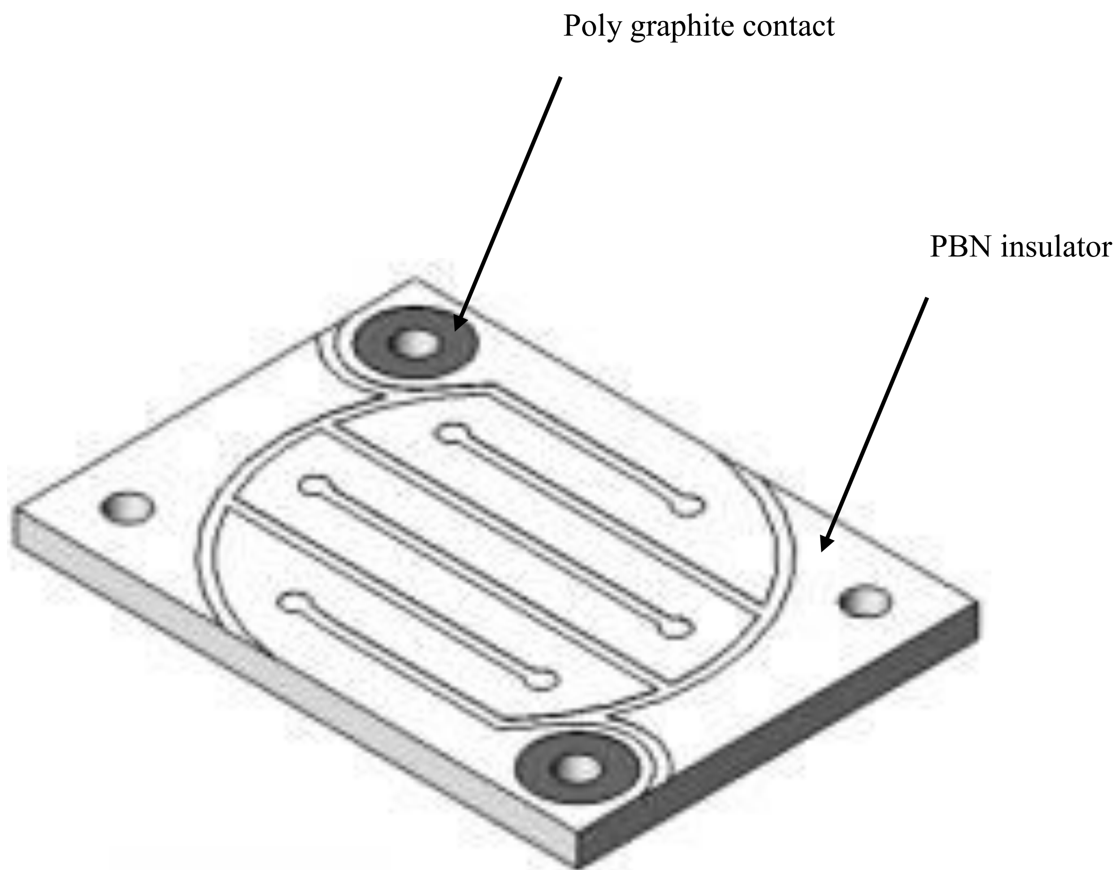

Figure 2.2: Boroelectric® heater [5]

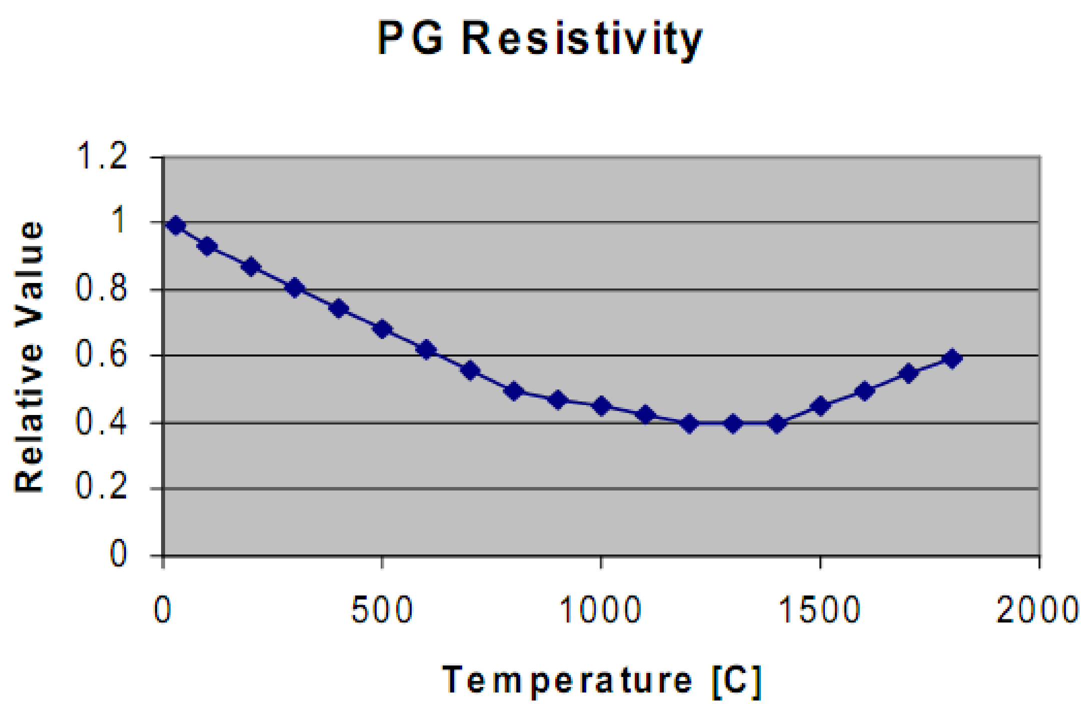

Figure 2.3: Effect of temperature on PG resistivity [6]

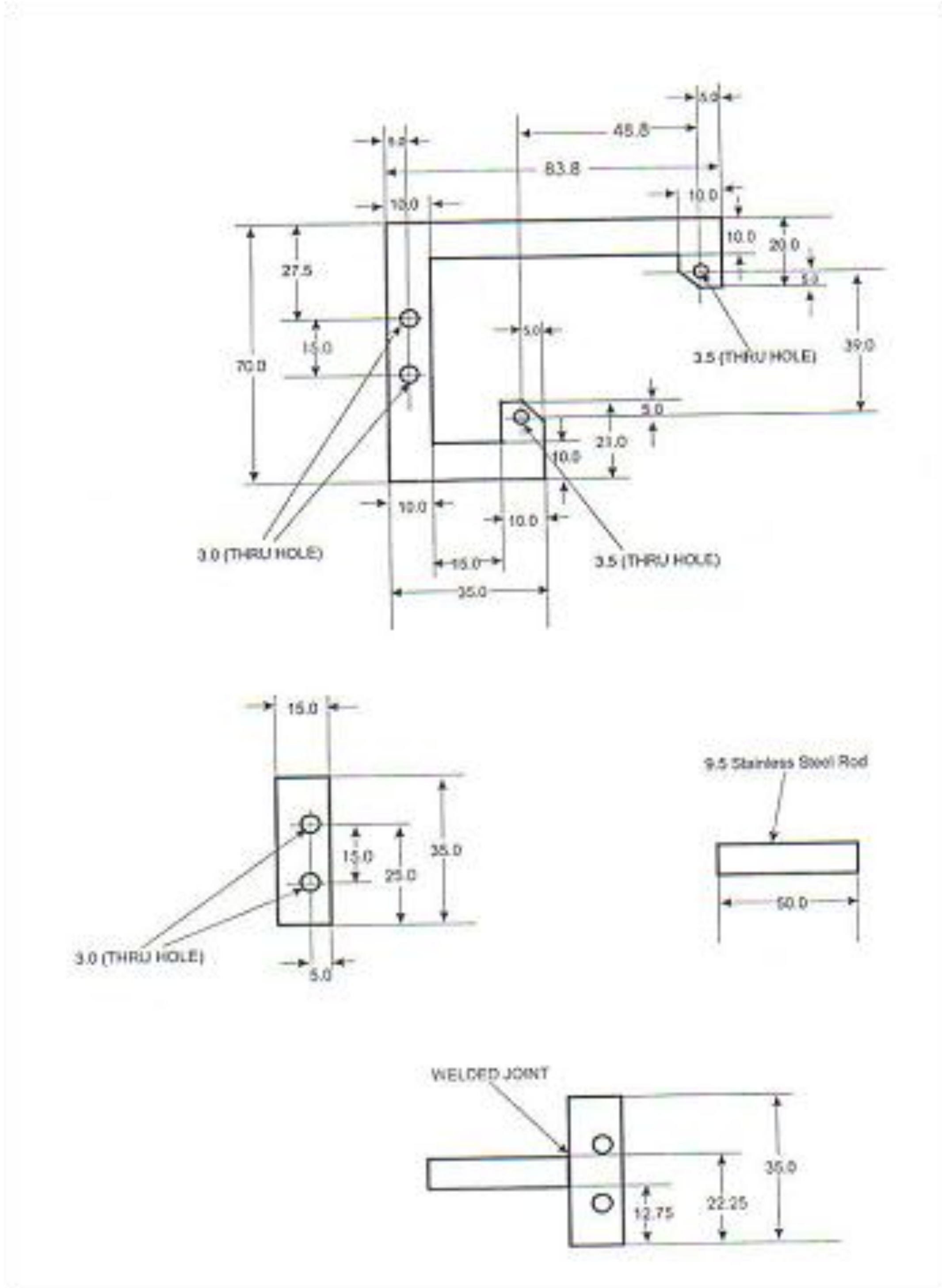

Figure 2.4: Drawing of stainless steel heater holder

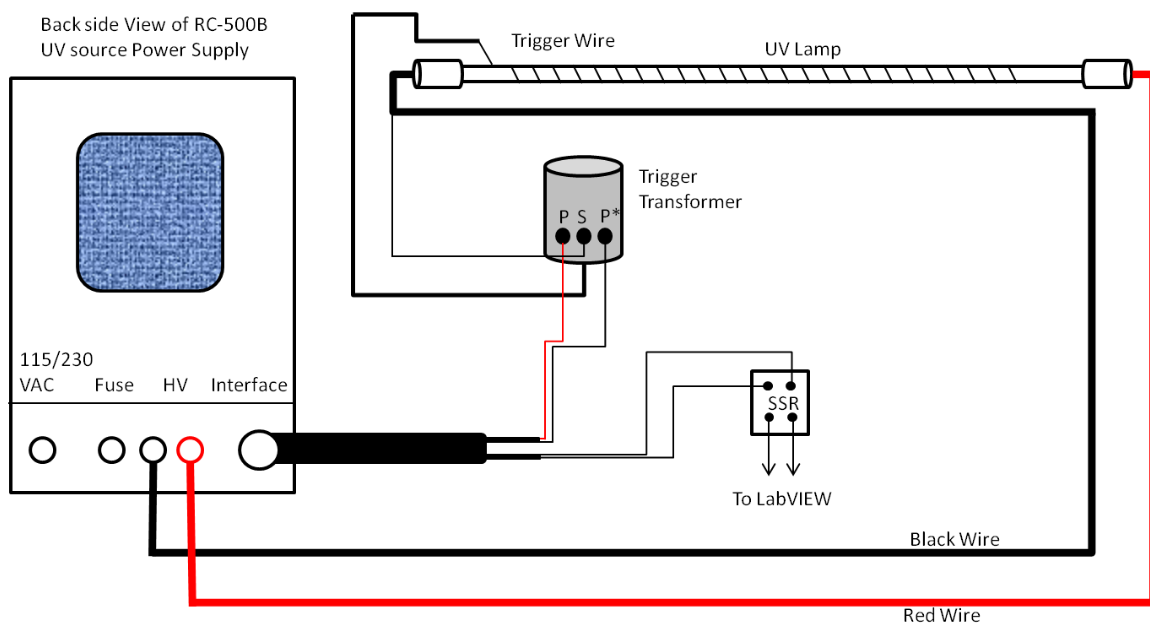

Figure 2.5: UV lamp connections to power supply and trigger transformer

CH	Model Number	Rated Gas	Flow Gas	Range (sccm)	Mode	GCF
1	1479A52CS1BM-S	H_2	N_2	500	Indp	1.000
2	1479A12CS1BM-S	HF	N_2	100	Indp	1.000
3	1179A12CS18V-S	H_2	Form Gas	100	Indp	0.990
4	1159B00500RV	N_2	O_2	500	Indp	1.000
5	1179AS2CS1BV-S	Ar	N_2O	500	Indp	0.518
7	1479A52CS1BA	TMB	N_2	100	Indp	0.330

Figure 2.6: MFCs setup configuration for 647B multi gas controller

CHAPTER THREE

ANNEALING OF SILICON OPTICAL FIBERS

This chapter is a journal article and reprinted with permission from N. Gupta, C. McMillen, R. Singh, R. Podila, A. M. Rao, T. Hawkins, P. Foy, S. Morris, R. Rice, K. F. Poole, L. Zhu, and J. Ballato, "Annealing of silicon optical fibers", J. Appl. Phys., vol. 110, 093107, 2011. © 2011 American Institute of Physics.

Abstract The recent realization of silicon core optical fibers has the potential for novel low insertion loss rack-to-rack optical interconnects and a number of other uses in sensing and biomedical applications. To the best of our knowledge, incoherent light source based rapid photothermal processing (RPP) was used for the first time to anneal glass-clad silicon core optical fibers. X-ray diffraction examination of the silicon core showed a considerable enhancement in the length and amount of single crystallinity post-annealing. Further, shifts in the Raman frequency of the silicon in the optical fiber core that were present in the as-drawn fibers were removed following the RPP treatment. Such results indicate that the RPP treatment increases the local crystallinity and therefore assists in the reduction of the local stresses in the core, leading to more homogenous fibers. The dark current-voltage characteristics of annealed silicon optical fiber diodes showed lower leakage current than the diodes based on as-drawn fibers. Photons in UV and vacuum ultraviolet (VUV) regions play a very important role in improving the bulk and carrier transport properties of RPP-treated silicon optical fibers, and the resultant

annealing permits a path forward to in situ enhancement of the structure and properties of these new crystalline core optical fibers.

3.1 Introduction

Silicon optical fibers, which only recently have been realized [1,2], have interesting optical properties that include Raman coefficient several orders of magnitude greater than the SiO_2 used in conventional optical fiber technologies and infrared transparency to about 7 µm. In addition, the availability of silicon as a feed-stock with 99.9999999% purity should make it possible to draw silicon fibers with almost no impurity related defects leading ultimately to low cost, low loss infrared fibers once extrinsic sources of loss are mitigated. Silicon fibers also provide a potential solution for rack-to-rack interconnects in integrated optoelectronic applications [3] as well as infrared power transmission at wavelengths associated with important atmospheric windows and novel nonlinear and Raman amplifiers [4, 5]. We have previously reported the fabrication of silicon [2], germanium [6, 7], and indium antimonide [8] optical fiber using commercially-accepted high-volume manufacturing processes; i.e., conventional optical fiber draw processes. Specifically, into a glass cladding tube is sleeved a rod of semiconductor that melts at the temperature where the glass cladding draws into fiber. In general, long lengths (> 100 meters) of crystalline semiconductor fiber were fabricated [6]. However, over distances of greater than a few centimeters, the crystal orientation is found to change; i.e., such fibers, overall, are polycrystalline. For completeness, it is worth noting that CVD processes have been employed to fabricate silicon [1, 9],

germanium [1, 9], and, more recently, ZnSe optical fibers [10]. Although such methods necessarily result in shorter lengths of fiber they permit high vapor pressure core materials, such as ZnSe, that would be more difficult to fabricate by the methods employed here.

The purpose of this work is to demonstrate the annealing of crystalline semiconductor optical fibers which, to the best of our knowledge, has not yet been reported. As compared to more conventional furnace-annealing, rapid thermal annealing provides better structural, electrical, optical and mechanical properties of low thermal mass materials [11], such as fibers. The output optical spectrum of the lamp that provides thermal and optical energy [12] plays an important role in the rapid thermal annealing process and, for this reason; it is appropriately called rapid photothermal processing (RPP) [13]. The objective of this work is to apply RPP to glass-clad silicon optical fibers and better understand the resultant crystallographic changes in order to obtain more homogenous crystalline microstructures.

3.2 Experimental

3.2.1 Fabrication of Glass-Clad Silicon Optical Fiber

Silicon rods that were 3 mm in diameter and 40 mm in length were placed into high purity silica cladding tubes (VitroCom, Inc., Mountain Lakes, NJ) with an outer diameter of 30 mm and inner diameter of slightly greater than 3 mm after one end of the cladding tube had been closed off. The resultant preform was drawn into about 1.6 mm fiber at about 1950 ℃ using an argon-purged carbon resistance furnace (Clemson

University, Clemson, SC). The choice of thick fiber was for ease of handling in the annealing experiments. The fiber was not coated because the subsequent RPP is conducted at a sufficiently elevated temperature where any polymer would degrade. Given that the melting temperature of silicon is 1414 ℃, the silicon is a fluent melt as the glass cladding is drawn into fiber [14], and no discontinuities occurred along the length [5].

3.2.2 Rapid Photothermal Annealing of Fibers

Commercial rapid thermal processing (RTP) employed in semiconductor manufacturing uses tungsten halogen (THL) lamps as the source of thermal and optical energy. Because the photo-spectrum of THL lamps lies in the visible and infrared (IR) region, at a given processing temperature, the diffusion coefficient of the participating atoms, molecules, dopants, and so on, is slightly higher than in furnace-only-based (photo-spectrum in the IR) processing [15]. Higher heating and cooling rates and higher diffusion coefficients of the participating species in solid state physical and chemical processes are the primary differences between conventional furnace processing (CFP) and RTP [15].

In previous work [16], the authors have shown that the use of ultraviolet (UV) and vacuum ultra violet (VUV) photons in RPP provide enhanced diffusion coefficients with respect to conventional CFP and RTP. Thus, in the case of rapid photothermal processing (RPP), other than thermal energy, the UV and VUV photons are used as an additional source of (optical) energy [17]. The RPP system, shown in Fig. 3.1, was used for ex situ

annealing of the silica-clad silicon optical fibers. The uncoated silica-clad silicon optical fibers were cleaved into crack-free pieces that were between 9 to 15 mm in length. The end-faces of the fibers were polished to a 0.5 μm finish in order to reduce roughness. Ex situ rapid photothermal annealing was performed under an ultrahigh-purity nitrogen environment at 950 °C for 10 min.

3.2.3 X-Ray Diffraction Measurements

Determination of the crystallographic orientation (and changes thereto) of the silicon relative to the fiber axis as a function of longitudinal position along the fiber was made using single crystal x-ray diffraction as has been described in detail previously [18]. Briefly, a Rigaku AFC8S diffractometer with Mo K_α radiation (λ = 0.71073 Å, 0.5 mm beam diameter) and a Mercury CCD area detector were used to collect 18 screening images in 1 mm increments along the length of silicon optical fiber. From these screening images the unit cell parameter was determined and the tilt and rotational angular orientations of several crystallographic directions of interest were determined relative to the longitudinal direction of the fiber. In this way the length of a single crystal grain could be determined by observing distinct changes in these angular orientations or localized regions containing many polycrystals where the unit cell parameter and crystallographic orientation could not be resolved.

Direct comparisons of the x-ray diffraction profiles were also performed at identical positions of a fiber before and after RPP treatment. Here, a position of the as-drawn fiber was selected such that one crystallographic orientation was dominant (where

the unit cell parameter and crystallographic orientation could both be determined and the diffraction intensities could be assigned (h k l) values based on this orientation), but where the diffraction profile also appeared to possess a greater number of diffraction spots having a some-what variable intensity. Thus, the position of interest likely contained multiple crystalline grains, with one being much larger than the smaller grain(s), and would be the most in-formative position as to whether this type of polycrystallinity could be improved by RPP. This polycrystallinity was observed to occur over about a 2 mm distance in the fiber analyzed. As before, 18 screening images were used to deter-mine the unit cell parameter and orientation. All observed diffraction intensities were tabulated according to their (h k l) assignments. The analyzed as-drawn fiber was then RPP treated, and the x-ray diffraction analysis was performed again at the exact longitudinal position on the treated fiber. It should be noted that the observed crystallographic orientation relative to the longitudinal axis of the fiber was the same before and after RPP with respect to the tilting angles of the orientations of interest. There was an observed (and consistent) bias in the rotational angles of the orientations of interest, as there was no reliable reference point available on the round fiber to exactly reposition it in that respect.

3.2.4 Micro-Raman Spectroscopy

Room temperature micro-Raman measurements were performed in a reflection mode using the 514.5 nm line of an Ar-ion laser incident on the fiber end. A Dilor XY triple grating monochromator equipped with Olympus IC 50X objective had a typical

spot radius of 1lm and a resolution of 0.1 cm^{-1} in the backscattering geometry. The Raman scattered signal from the samples was detected using a thermoelectric-cooled charge-coupled device (CCD). The incident laser power was limited to ~ 0.5 mW in order to avoid any possible heating of the sample. A Voigt line-shape was used to curve-fit the resultant spectra. The Voigt line-shape is a convolution of a Lorentizian line-shape (identical oscillators) and a Doppler line-shape (non-identical oscillators) and is employed when oscillators that would give a Lorenztian shape are inhomogeneously affected by an extrinsic influence, such as strain. For reasons noted below, this convolution aspect suggests that Voigt is appropriate for use in this work. Wafers of Si (100) and 300 nm SiO_2 on Si (MTI Crystals, Richmond, CA) were used as reference standards.

3.2.5 Diode Fabrication and Current-Voltage Characteristics

Aluminum, thermally evaporated onto both faces of the fibers, was used to make electrical contact. Prior to evaporating the metal onto the second fiber end, the first electrode was sintered at 475 °C for 20 min in nitrogen in order to form an ohmic contact to the silicon. The second fiber end-face was left unsintered in order to form a Schottky barrier. Electrical characterization then was carried out using an HP4140B pico-ammeter and voltage source and probe station.

3.3 Results and Discussion

3.3.1 X-Ray Diffraction Results

Comparison between the macroscopic single crystallinity of the RPP-treated and as-drawn fibers was first made along the longitudinal direction of separate lengths of fiber drawn under identical fabrication conditions as described previously. These results are shown in Fig. 3.2. The orientation of the untreated (as-drawn) fiber was found to be locally single crystalline at 4 of the 6 positions analyzed, with the longest continuous length of a single crystallographic orientation persisting for 2–3 mm of the fiber. The orientation of the RPP-treated fiber was analyzed at 10 positions, and all 10 exhibited the same crystallographic orientation, corresponding to a single crystal length of at least 9 mm.

In order to make a more direct comparison of the effects of the RPP treatment, the x-ray diffraction profiles were analyzed at a common position on a common fiber before and after treatment. Prior to RPP treatment (Fig. 3.3(a)) 70 unique reflections were observed, with intensities ranging from about 1000–220 000 counts. After RPP treatment (Fig. 3.3(b), middle) only 32 unique reflections were observed, with their intensities ranging from about 1000–100 000 counts. From this it is clear that there were fewer reflections having a much smaller scatter in their intensity values following the RPP treatment. These results are directly compared in Fig. 3.3(c), bottom.

To date, single crystalline x-ray orientation analysis of about 60 mm of as-drawn silicon fiber (using randomly-selected 10 mm segments) has been performed. Of these, the crystallographic orientation was determined to be about 70% of the individual

positions, identifying those 0.5 mm diameter regions as locally single crystalline. The longest continuous single crystal grain observed in the as-drawn fiber has been 5 mm in length (observed in two separate regions of fiber) before the orientation changes or many small polycrystals prevented the determination of the crystallographic orientation. It seems remarkable that the very first RPP-treated silicon fiber analyzed was not only locally single crystalline at every position analyzed, but in fact maintained the same orientation over the entire length of the fiber. This 9+ mm length nearly doubles the previous longest single crystal grain observed in silicon fibers and is suggestive that RPP plays a role in improving the long range crystallinity in these crystalline semiconductor core optical fibers. The direct comparison of the x-ray reflection profiles at a single common position before and after RPP similarly suggests improvement of the crystallinity on this smaller scale. It is expected that a region containing only one crystallographic orientation should have a simpler x-ray reflection profile than a region containing several polycrystals. In this study, significantly fewer unique x-ray reflections and a more even distribution of reflection intensities are observed after RPP compared with the as-drawn fibers. X-ray diffraction examination of the crystal structure of as-drawn fiber of 5 mm length showed a 3 mm stretch of single crystal silicon and 2 mm of polycrystalline material. On the other hand, the entire 10 mm length of the annealed sample was single crystalline. For completeness, it is worth noting that the oxygen content in these fibers is about 1–2 at. %, which, through process optimizations, is considerably reduced from the ~18% of the initial silicon fibers [2]. That said, oxide inclusions may induce defects that cannot be further removed by using RPP.

3.3.2 Raman Spectroscopy

Figure 3.4 provides the first- and second-order Raman scattering spectrum of crystalline silicon, consisting of three degenerate optical phonons present at about 521 cm^{-1} (Ref. 19), along with differences observed in the Raman spectra collected from various locations on the as-drawn and RPP-treated fibers.

Renucciet al. [20] observed non-linear dispersion of the 520 cm^{-1} peak as a function of stress. Later, several reports used such observable shifts in the Raman frequency of silicon to probe localized stress fields in Si systems [21–24]. Figure 3.4(b) shows the Raman spectra collected from various locations (Fig. 3.4(a)) across the as-drawn fiber. Interestingly, the Raman shift seems to vary with the location, indicating the existence of stresses across the fiber core. Specifically, the Raman spectrum collected at spot B exhibits a two-peak structure (~520 cm^{-1} and 527 cm^{-1}), suggesting the presence of local stress. It should be noted that inhomogeneous nucleation of dislocations may occur in the as-drawn fiber due to local temperature and pressure gradients during the fiber drawing process [22]. The presence of such inhomogeneous dislocations results in a non-uniform distribution of the residual stresses. Further, any crystal anharmonicity or symmetry lowering introduced by such a local stress field also can lift the degeneracy of longitudinal and transverse optical phonons leading to two peaks (spectrum B; Fig. 3.4(a)) in the Raman spectrum. In addition, the enhancement of the second-order Raman spectra at spots B and C is consistent with the existence of such anharmonicity or symmetry lowering (Fig. 3.4(c)). To better understand the local stress in the as-drawn fiber, Raman spectra were collected from other spots, as shown in Fig. 3.4(a). The first-

and second-order micro-Raman spectra with in the vicinity of spot B also exhibit features similar to B (Figs. 3.4(d) and 3.4(e)) confirming the existence of local stress in the sample. Anastassakis et al. [19] assumed an in-plane stress model in order to derive a relation between change in Raman frequency ($\delta\omega = \omega_{sample} - \omega_{single\ crystal}$) and the stress ($\sigma$) [22, 23] as $\sigma(\mathrm{MPa}) = -250\ (\mathrm{MPa} \cdot \mathrm{cm}) \times \delta\omega\ (\mathrm{cm}^{-1})$. Figure 3.4(f) provides the stress distribution of the as-drawn fiber obtained using this equation based on the measured Raman shifts across the silicon core. The magnitude of the stress field in the as-drawn fibers is similar to the dislocation/grain boundary stress observed in polycrystalline silicon [21–24].

Raman spectra (Fig. 3.4(g)) also were collected from various locations on the RPP-treated fiber. As expected, the observed shifts in silicon Raman frequency in the as-drawn fiber were no longer present in the RPP-treated fiber. Such results are corroborated by the x-ray diffraction measurements, indicating that the RPP treatment increases the local crystallinity and therefore assists in the reduction of the local stress fields in the samples, leading to a more homogenous fiber.

3.3.3 Schottky Diode Characteristics

Dark current-voltage characteristics of Schottky barrier diodes are shown for as-drawn and RPP-treated fiber in Fig. 3.5. The decrease in reverse leakage current is very significant from as-drawn fiber to RPP-treated fiber. The origin of leak-age current in semiconductor devices is directly related to defects in the semiconductor crystal structure and the reduction in leakage current implies an improved crystalline structure of silicon

core arising from the RPP treatment, as will be discussed in greater detail in what follows. It is worth noting that the leakage current of the annealed samples treated here is an order of magnitude lower than that for the silicon fiber reported in Ref. 9. Further, the core size of the fibers reported previously is 5 μm [9], whereas the core size in this work was 100 μm. The lower leakage current density observed should improve the performance and reliability of transistors based on the larger core size silicon optical fibers.

Transport properties of semiconductors are highly de-pendent on impurities and defects in the crystal lattice. The diode characteristics shown in Fig. 3.5 are in concert with the structural homogeneity of RPP-treated fibers as observed by x-ray diffraction and Raman microscopy. In a recent paper [25], it was shown that the use of UV and VUV photons in RPP, relative to CFP and RTP, enhances the diffusion coefficient of dopants by many orders of magnitude. As noted previously, in the case of rapid photothermal processing (RPP), other than thermal energy, the VUV photons are used as an additional source of optical energy. The thermal factor leads to the excitation (vibration) of atoms and the optical energy leads to additional electron excitation. The optical energy contribution is explained by the “deformed molecule” model proposed for the explanation of the decreasing of the defect energy formation in the crystal lattice of semiconductors [26]. The principal advantages of RPP over other thermal processing techniques are as follows: (i) reduced density of defects, (ii) reduced process variations, (iii) enhanced throughput, and (iv) lower processing temperatures [15]. With continued and further process optimization, it is expected that even higher degrees of structural

homogeneity of semiconductor optical fibers are possible, with an important first step reported here.

3.3.4 *A Comment on Optical Transmission*

An appropriate question raised by these results would be whether or not the optical attenuation of the silicon optical fiber improved with annealing, given the observed improvements in single crystallinity and stress uniformity and reduction in conductivity. For these initial experiments, transmission measurements were not attempted because the samples would have to be removed from any attenuation measurement apparatus to be annealed (or electroded) and, hence, the launch conditions could not be replicated with certainty. It is well-known that, for highly multimoded wave-guides—especially ones of relatively short length as were used here—different eigen-modes are excited, depending upon how the input light is coupled into the core. For example, if a focused Gaussian beam is launched into the center of the core, the fundamental and lowest order modes will be principally excited, assuming there is not much scattering. However, if light is launched close to the core/clad interface then many high order modes will be excited, leading to quite different effective attenuation values.

That said, in future efforts, the loss of samples before and after processing will be measured and attempts will be made to make *in situ* transmission measurements during annealing. Further, while the silicon optical fibers were *ex situ* annealed in this work, it is reasonable given the process conditions that on-line annealing during the draw can be performed.

3.4 Conclusion

On the basis of the evidence from single crystal x-ray diffraction, Raman spectroscopy, and Schottky diodes, *ex situ* rapid photothermal annealing is shown to enhance the structural homogeneity of silicon optical fibers. Photons in UV and VUV regions play an important role in improving the bulk and surface carrier transport properties of RPP-treated silicon fibers. Optimization of annealing parameters can further improve the structural homogeneity of silicon fibers, thereby further advancing their optoelectronic performance and moving semiconductor core optical fiber technology closer to practical device implementation.

References

[1] B. Jackson, P. Sazio, J. Badding, "Single-crystal semiconductor wires integrated into microstructured optical fibers", Adv. Mater., vol. 20, pp. 1135–1140, 2008.

[2] J. Ballato, T. Hawkins, P. Foy, R. Stolen, B. Kokuoz, M. Ellison, C. McMillen, J. Reppert, A. M. Rao, M. Daw, S. Sharma, R. Shori, O. Stafsudd, R. R. Rice, and D. R. Powers, "Silicon optical fiber", Optics Express, Vol. 16, Issue 23, pp. 18675-18683, 2008.

[3] R. Singh, N. Gupta, J. A. Sadie, K. F. Poole, J. Ballato, and S. J. Hwu, "Challenges and opportunities of manufacturing the next generation of integrated photonics", Proc. of SPIE, Vol. 7591, pp.75910N1-75910N8, 2010.

[4] D. Graham-Rowe, "Fibres get functional", Nature Photonics, vol. 5, pp. 66-67, 2011.

[5] J. Ballato, T. Hawkins, P. Foy, B. Yazgan-Kokuoz, C. McMillen, L. Burka, S. Morris, R. Stolen, and R. Rice, "Advancements in semiconductor core optical fiber", Opt. Fiber Technol., vol. 16, pp. 399-408, 2010.

[6] J. Ballato, T. Hawkins, P. Foy, B. Yazgan-Kokuoz, R. Stolen, C. McMillen, N. K. Hon, B. Jalali, and R. Rice, "Glass-clad single-crystal germanium optical fiber", Opt. Express, vol. 17, pp. 8029-8035, 2009.

[7] J. Ballato, T. Hawkins, P. Foy, S. Morris, N. K. Hon, B. Jalali, and R. Rice, "Silica-clad crystalline germanium core optical fibers", vol. 36, issue 5, pp. 687-688, 2011.

[8] J. Ballato, T. Hawkins, P. Foy, C. McMillen, L. Burka, J. Reppert, R. Podila, A. Rao, and R. Rice, "Binary III-V semiconductor core optical fiber", Opt. Express, vol.18, pp. 4972-4979, 2010.

[9] C. Finlayson, A. Amezcua-Correa, P. Sazio, N. Baril, and J. Badding, "Electrical and Raman characterization of silicon and germanium-filled microstructured optical fibers", Appl. Phys. Lett., vol. 90, article no. 132110, 2007.

[10] J. Sparks, R. He, N. Healy, M. Krishnamurthi, A. Peacock, P. Sazio, V. Gopalan, and J. Badding, "Zinc Selenide Optical Fibers", Adv. Mater., vol. 23, issue 14, pp. 1647-1651, 2011.

[11] R. Singh, "Rapid Isothermal Processing", J. Appl. Phys., vol. 63, R59, 1988.

[12] R. Singh, "Rapid Isothermal Processing," Chapter 9 in Handbook of Compound Semiconductors: Growth, Processing, Characterization, and Devices, P. Holloway and G. McGuire, editors, Noyce Publishers (New York), pp. 442 – 517, 1995.

[13] R. Singh, M. Fakhruddin and K. F. Poole, “Rapid photothermal processing as a semiconductor manufacturing technology for the 21st century”, Appl. Surf. Sci., vol. 168, issue 1-4, pp. 198-203, 2000.

[14] J. Ballato and E. Snitzer, “Fabrication of fibers with high rare-earth concentrations for Faraday isolator applications”, Appl. Opt., vol. 34, pp. 6848-6854, 1995.

[15] R. Singh, S. Sinha, R.P.S. Thakur, and P. Chou, “Some photoeffect roles in rapid isothermal processing”, Appl. Phys. Lett., vol. 58, article no. 1217, 1991.

[16] R. Singh, K.C. Cherukuri, L. Vedula, A. Rohatgi, J. Mejia, and S. Narayan, “Enhanced diffusion and improved device performance using dual spectral source rapid thermal processing”, J. Electron. Materials, vol. 26, pp. 1422-1427, 1997.

[17] R. Singh, V. Parihar, Y. Chen, K.F. Poole, S. Nimmigadda, and L. Vedula, “Importance of rapid photothermal processing in defect reduction and process integration”, IEEE Trans. Semicond. Manufac., vol. 12, issue 1, pp. 36-43, 1999.

[18] C. McMillen, T. Hawkins, P. Foy, D. Mulwee, J. Kolis, R. Stolen, R. Rice, J. Ballato, “On crystallographic orientation in crystal core optical fibers”, Opt. Mater., vol. 32, issue 9, pp. 862-867, 2010.

[19] E. Anastassakis and E. Liarokapis, “Polycrystalline Si under strain: Elastic and lattice-dynamical considerations”, J. Appl. Phys., vol. 62, article no. 3346, 1987.

[20] J. Renucci, R. Tyte, and M. Cardona, “Resonant Raman scattering in silicon”, Phys. Rev. B, vol. 11, issue 10, pp. 3885-3895, 1975.

[21] I. D. Wolf, H. E. Maes and S. K. Jones, “Stress measurements in silicon devices through Raman spectroscopy: Bridging the gap between theory and experiment”, J. Appl. Phys., vol. 79, issue 9, article no. 7148, 1996.

[22] G. Sarau, M. Becker, S. Christiansen, M. Holla, and W. Seifert, “Micro-raman mapping of residual stresses at grain boundaries in multicrystalline block cast silicon solar cell material:their relation to the grain boundary microstructure and recombination activity”, Proc. 24th European Photovoltaic Solar Energy Conference, Hamburg, Germany, Sep. 21st -25th, 2009, pp. 969-973.

[23] H. Talaat, S. Negm, H. E. Schaffer, G. Kaltsas, A. G. Nassiopoulou, “Micro-Raman analysis of polysilicon membranes deposited on porous silicon channels”, J. Non-Crystal. Solids, vol. 266-269, part 2, pp. 1345-1349, 2000.

[24] V. Paillard, P. Puech, M. A. Laguna, P. Temple-Boyer, B. Caussat, J. P. Couderc, and B. deMauduit, “Resonant Raman scattering in polycrystalline silicon thin films”, Appl. Phys. Lett., vol. 73, issue 12, article no. 1718, 1998.

[25] S. Shishiyanu, R. Singh, T. Shishiyanu, S. Asher, and R. Reedy, “The Mechanism of Enhanced Diffusion of Phosphorus in Silicon During Rapid Photothermal Processing of Solar Cells,” Electron Devices, IEEE Transactions on , vol.58, no.3, pp.776-781, 2011.

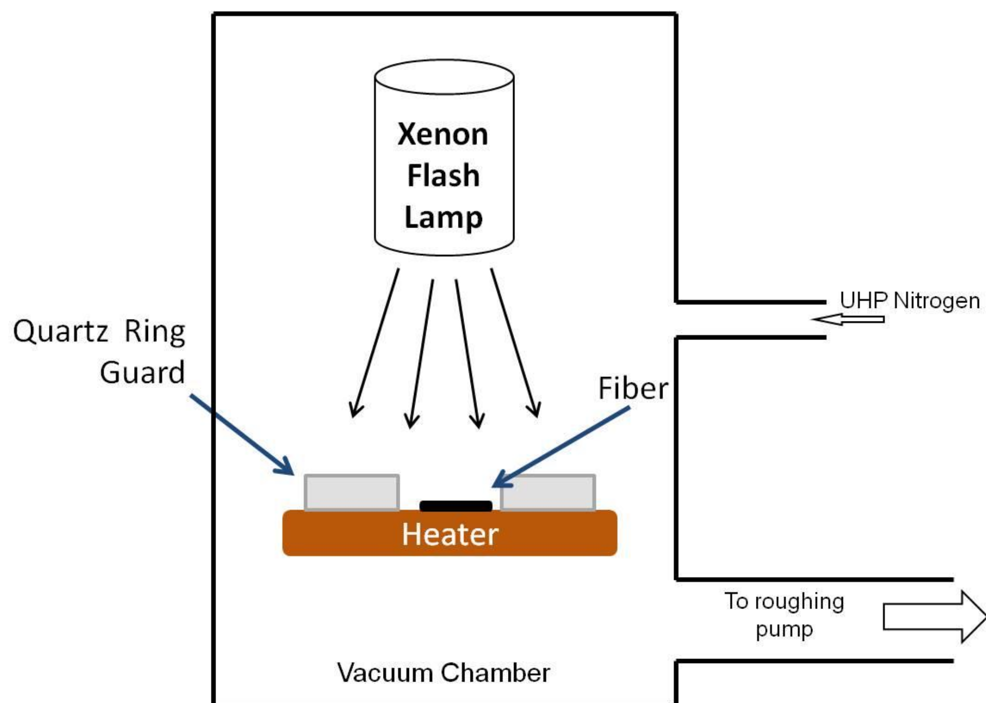

Figure 3.1: (Color online) Rapid photothermal processing (RPP) system employed in this work for the *ex situ* annealing of glass-clad silicon optical fibers.

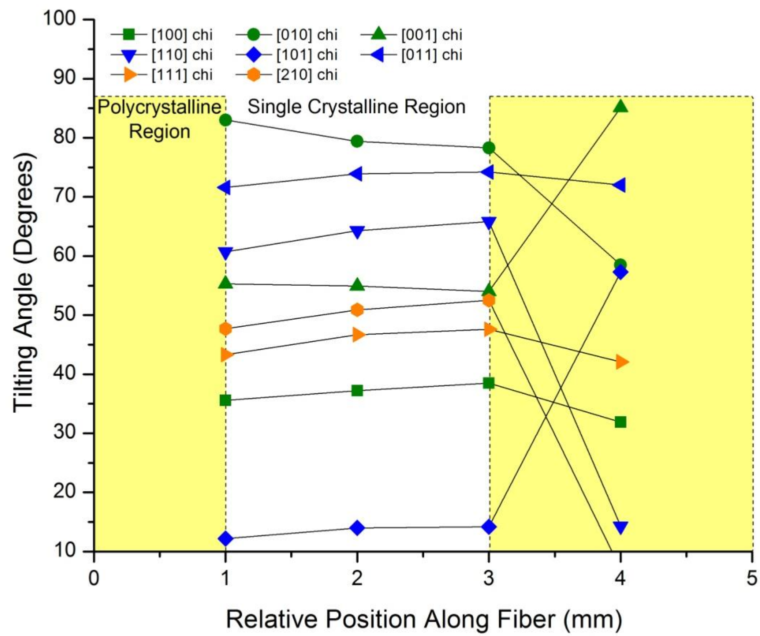

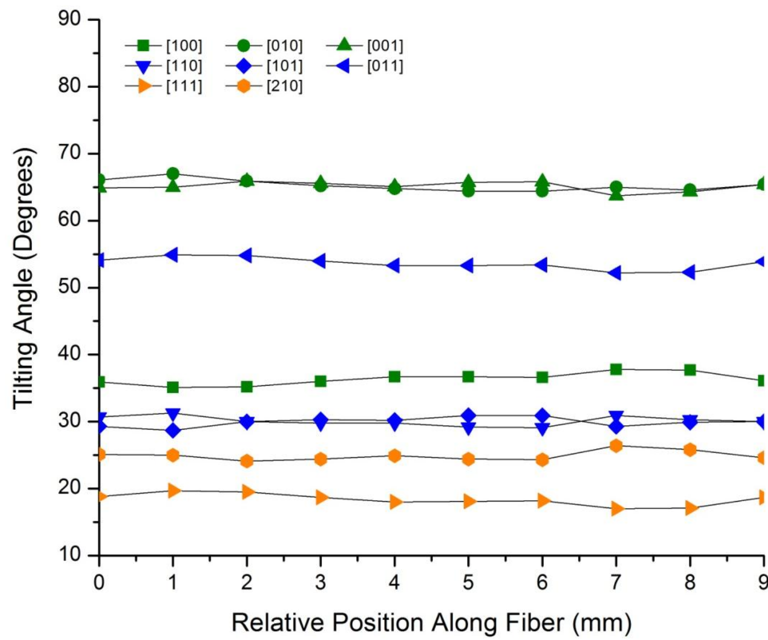

Figure 3.2: (Color online) Longitudinal x-ray measurements for the as-drawn fiber (a) and rapid photothermal processing (RPP)-treated fiber (b).

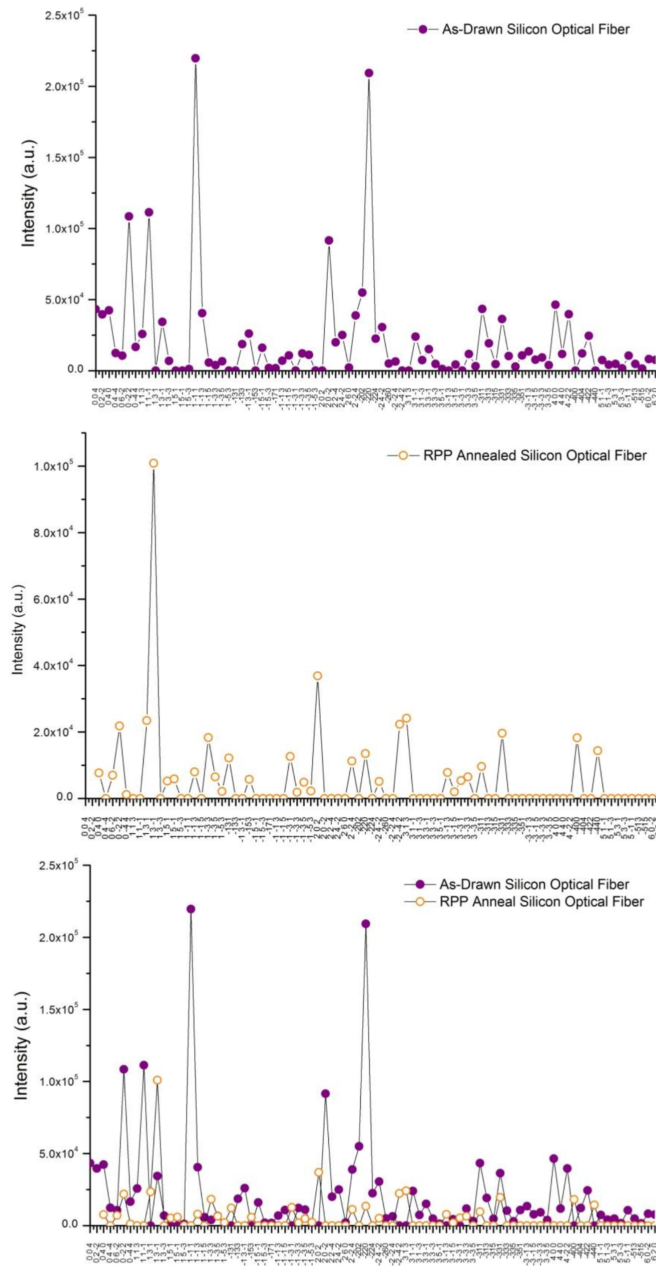

Figure 3.3: (Color online) X-ray crystallography results at the same location (3 mm relative location) of silicon optical fiber: as-drawn (a), RPP-annealed (b), and combined for direct comparison (c). The abscissa denotes the (h k l) Miller indices and values of zero added when no reflections were observed for a given orientation.

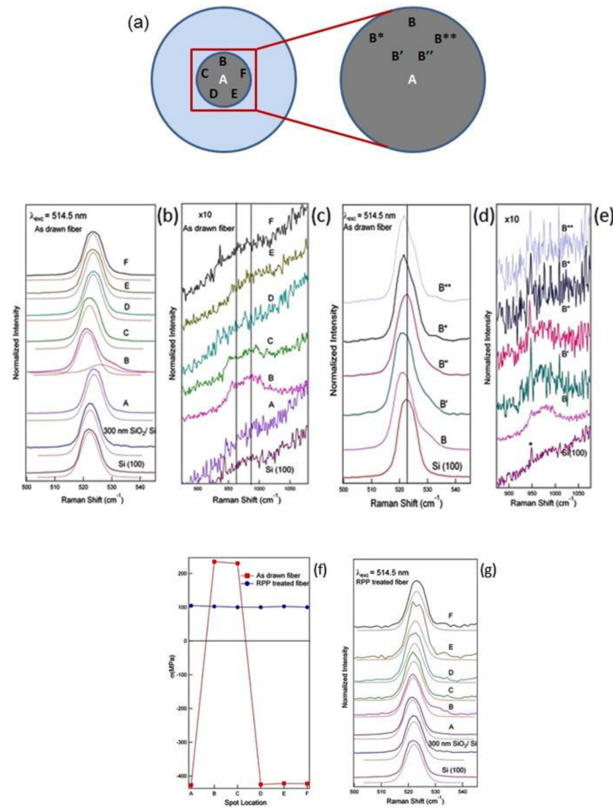

Figure 3.4: (Color online) (a) Schematic of the silicon optical fiber showing the locations where Raman spectra were collected. (b) First order spontaneous Raman scattering spectra for the as-drawn fiber; the dotted red curves represent the de-convoluted peaks obtained using a Voigt curve-fit. (c) Second order Raman spectra collected at the spots shown in (a); locations B and C clearly show the 2 TO-LO phonon modes ~ 975 cm^{-1}. First (d) and second order (e) Raman spectra corresponding to the locations shown in (a). The starred peaks in (e) indicate a plasma line associated with the laser. (f) The in-plane stress present at the noted locations across the as-grown and annealed silicon optical fiber obtained using the relative Raman shifts (see text). (g) Raman spectra collected from noted positions across the annealed (RPP treated) fiber; the dotted red curves represent the de-convoluted peaks obtained from curve fitting using a Voigt line shape.

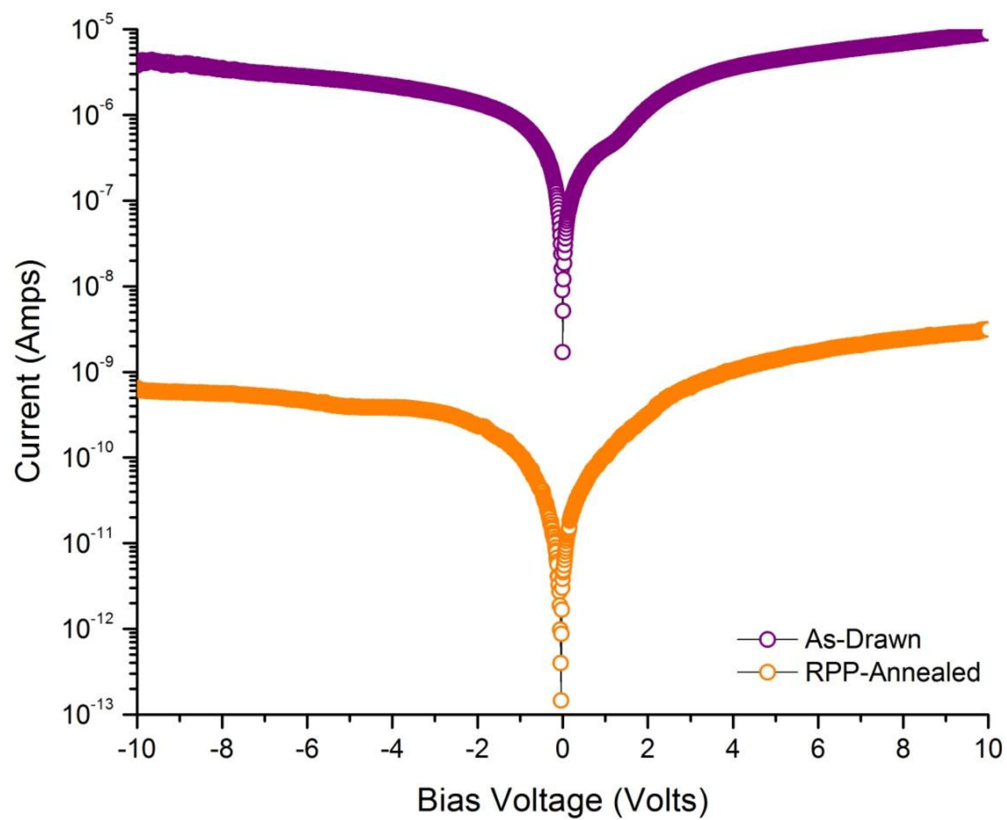

Figure 3.5: (Color online) Current-voltage (I-V) characteristics for the Schottky barrier diode fabricated using the as-drawn and annealed (RPP-treated) silicon optical fiber.

CHAPTER FOUR

PHOTO-ASSISTED METAL-ORGANIC CHEMICAL VAPOR DEPOSITION OF HIGH DIELECTRIC CONSTANT THIN FILM

This chapter is based on a journal article submitted for publication as *N. Gupta and C. McMillen "Photo-Assisted Metal-Organic Chemical Vapor Deposition of $CaCu_3Ti_4O_{12}$ (CCTO) Thin Film"*.

4.1 Introduction

Since the invention of the first capacitor in the 1700's, researchers have suggested several high dielectric constant materials including $BaSrTiO_3$, $PbLaZrTiO_3$, etc., to create energy storage capacitors with high energy density. However, commercial available capacitors use highest dielectric constant of 25 in Ta_2O_5 based tantalum capacitor. Table 4.1 shows the highest dielectric constant published in open literature for various dielectric materials. In recent years, one of the most researched materials with giant dielectric constant is calcium copper titanate ($CaCu_3Ti_4O_{12}$) or CCTO which is a perovskite-like structure ceramic. CCTO does not carry any toxic element, therefore there are no environmental or health issues associated. Also, fair temperature stability has been shown for CCTO over wide temperature range for lower frequencies [1]. The high dielectric constant of CCTO (10,286 at 100 KHz) was reported for the first time by Subramanian et al. in 2000 [2]. Subsequently, several methods were explored to synthesize this material in bulk as well as in thin films on various substrates. These methods include solid state

synthesis [2], chemical method [3], sol-gel [4], Pulse Laser Deposition (PLD) [5], and metalorganic chemical vapor deposition (MOCVD) [6]. Highest dielectric constant published for CCTO is $1x10^{06}$ reported for Nb doped $CaCu_3Ti_4O_{12}$ (CCTO) [7]. It is worth mentioning that recently, Khumpaitool et. al. reported a dielectric constant of $7.25x10^6$ for 0.2 wt.% Al_2O_3 doped $Li_{0.30}Cr_{0.02}Ni_{0.68}O$ with loss factor (tan δ) of 2.37 at 1 KHz [8].

The origin of the very high dielectric constant in CCTO is still in debate among researchers. The possible mechanisms for the very high dielectric constant in CCTO are partly explained by the internal barrier layer capacitance (IBLC) model, consisting of grain boundary effects and the Maxwell-Wagner effect, focusing on sub-grain boundaries [6]. However, IBLC does not explain completely this effect on a single crystal material. In 2005, Wu et al. reported another model similar to IBLC for single crystal CCTO [9]. At the same time, several researchers have also asserted that physical, structural, and stoichiometric properties of the dielectric film, including defects cause different dielectric properties [10, 11]. Thus, the origin of the very high dielectric constant in CCTO is still not apparent. However, the value of the dielectric constant of un-doped CCTO is variously reported from 200 to $8x10^4$ to 200 [12, 13]. This variation of the dielectric constant implies a strong dependence of dielectric properties of CCTO on the fabrication process. Almost every electronic material's properties depend on the fabrication method.

In several areas of semiconductor manufacturing, rapid photothermal processing (RPP) has proved itself a superior technique for depositing dielectric thin films with very low leakage current, low defect density and good reliability at low thermal budget [14-

17]. For the very first time, Singh et al. exploited the advantages of photo-assisted CVD in their work published in 1991[18]. This unique processing technique uses photo energy as an additional source of energy with thermal energy. From the electromagnetic spectrum, only the photons with wavelength more than about 800 nm contribute to thermal effects, while photons between 400 nm and 800 nm contribute to both thermal and quantum effects [19]. Photons with wavelength less than 400 nm provide quantum effects without any undesirable effect. The quantum effects have the following implications for the photo-assisted CVD process [20]; (i) The bulk and surface diffusion coefficients are increased for a given processing temperature, (ii). The processing cycle time is reduced, (iii) Due to lower microscopic defects, higher performance, better reliability and yield are achieved.

The Xenon flash lamp used in this work emits photons with wavelength from 200 nm to more than 1000 nm, as shown in Figure 4.1 [21]. The spectrum emitted from the Xenon flash lamp provides both thermal and quantum effects and produces high quality thin film of the material being deposited.

4.2 Experimental Details

4.2.1 Photo-assisted MOCVD System

A custom-designed non-commercial MOCVD system with an incoherent light source, as illustrated in Figure 4.2, was used to deposit high quality CCTO thin films on Si/SiO_2 substrates. Prior to depositing CCTO on Si/SiO_2 substrate, several other substrates were tried. A detailed discussion will be given later in the chapter. The

substrates were prepared by growing silicon dioxide on p-type (100) silicon wafers in a furnace using wet oxidation at 1050 ºC for four hours, to achieve an oxide thickness of about 500 nm. For the photo-assisted MOCVD process, the calcium and copper precursors ($Ca(TMHD)_2$ and $Cu(TMHD)_2$) were purchased from Strem chemicals while the Titanium precursor, Titanium(IV) isopropoxide ($C_{12}H_{28}O_4Ti$), was purchased from Alfa Aesar. In the past, we have used 2,2,6,6-tetramethyl-3,5-heptanedionato (TMHD) to create several high quality films [22], [23]. All the precursors used in this work were used as purchased without any modifications. Except for the nitrous oxide, all gases used in the process were ultra-high purity (UHP). Based on our previous experience of depositing dielectric films using CVD, nitrous oxide and UHP oxygen were used as the reaction gases [23]. UHP nitrogen was used as the carrier gas to transport precursor vapors from the precursor oven to the deposition chamber. MKS mass flow controllers (MFC) were used to control gas flow rates for all the gases. All the precursors were kept in heated stainless steel ovens and connected by a heated delivery line to the deposition chamber as shown in Figure 4.2. The temperature of delivery line was maintained at 180ºC for all the experiments. The temperatures in the precursor ovens and delivery lines were monitored with K type thermocouples and controlled with LabView modules. The UV source, MFCs and solenoid gas valves were also controlled with LabView Modules to improve process effectiveness. Table 4.2 shows a summary of optimized process parameters, as used for sample no. P97, including precursor temperatures and flow rates for different gases used in the process. The base pressure and deposition pressure for the process was $2x10^{-2}$ torr and 1.2 torr, respectively.

4.2.2 Process Flow of Photo-assisted MOCVD

A thermally oxidized p-type (100) Si wafer was loaded into the MOCVD deposition chamber. The substrate was cleaned in-situ in forming gas (20% UHP H_2 and 80% UHP N_2) at 925 ºC for five minutes. Ca and Cu precursors were heated in vacuum at 230ºC and 120ºC respectively, while the Ti precursor was used at room temperature. After cleaning the substrate in-situ, the substrate was brought to the deposition temperature of 750 ºC and the deposition process was carried out for 15 min. After deposition, the deposited film was then annealed at the deposition temperature in an atmosphere of UHP O_2 for 5min. N_2O and carrier gas flow was switched off during the annealing cycle. After which, the substrate was allowed to cool to room temperature in vacuum. The UV light source was kept on during in-situ cleaning, deposition and annealing. The thermal cycle for CCTO thin film MOCVD deposition process is shown in Figure 4.3.

4.2.3 Stepwise Deposition Process

Following is the process steps for CCTO deposition on Si/SiO_2 substrate.

1. Turn on the rotary pump and open the vacuum valve of the chamber.
2. Turn on pressure gauge.
3. Turn on the computer and MKS647B MFC controller.
4. Open gas cylinder and gas lines (on the wall) valves required for the process.
5. Run the LabVIEW programs: ultimate reader with control.vi and valve sequence.vi.

6. Open V1, VMFC5, VMFC6 from valve sequence.vi and O_2 manual valve.
7. Wait to reach the vacuum in 10^{-03} Torr range.
8. Open the back air admittance valve.
9. Open the cover of the deposition chamber.
10. Load the oxidized silicon wafer in the deposition chamber.
11. Close the deposition chamber.
12. Check the precursor oven to refill any precursor required.
13. Start roughing the main chamber.
14. Wait till, when vacuum reaches $3x10^{-03}$. While waiting, run VIs for precursor oven and delivery line heaters and check set points. But, do not turn on these heaters.
15. Close O_2 valve manually and V1, and VMFC5 form LabVIEW.
16. To start the cleaning process, open UV control with timer.vi and enter desired cleaning time in seconds.
17. Turn on channel 3 from MFC controller to flow forming gas.
18. Set the variac to cleaning temperature and heat wafer to desired cleaning temperature.
19. Turn on UV lamp power supply.
20. When cleaning temperature is reached, start flowing UV cooling gas (N_2).
21. Run the UV control with timer.vi and start UV lamp manually from UV lamp power supply. Start heating precursor ovens and delivery lines

22. When the cleaning cycle will be completed the UV lamp will turn off automatically. Turn off wafer heater and UV cooling gas.
23. When substrate temperature reaches below 300 ^{o}C, turn off VMFC6 form LabVIEW and forming gas flow from MFC controller.
24. When precursor oven reaches desired temperature, turn on wafer heater for deposition temperature.
25. Open VI for deposition process and enter deposition time in seconds.
26. Make sure all the channels in MFC controller have the correct process flow rates.
27. Rough the titanium oven using roughing pump.
28. When substrate is at deposition temperature, run deposition vi and follow the instructions. Also, start flowing UV lamp cooling gas.
29. Wait to finish deposition cycle.
30. After deposition cycle, LabVIEW will automatically close the MFCs, UV lamp and valves.
31. Turn off all the precursor oven heaters and delivery line heater.
32. If annealing is being done at same temperature as deposition; therefore do not turn off the substrate heater.
33. Also, start flowing UV lamp cooling gas. Open and run O_2 annealing vi for desired time.
34. After annealing cycle, close all the LabVIEW programs, UV cooling flow gas and substrate heater. Also, close all the process gas cylinders and follow lab shutdown procedure.

35. When wafer reaches room temperature, take the wafer further measurements.

4.2.4 Characterization Details

Powder X-ray diffraction (XRD) measurements were performed using an angle dispersive diffractometer (Rigaku Ultima IV) with monochromated Cu-Ka (λ = 1.540 Å) radiation at 40 kV. Data was collected at a rate of 1.2º 2Θ per minute in 0.2º 2Θ steps. Surface morphology was analyzed using FEI Nova Nanolab 200 scanning electron microscope (SEM). The CCTO film thickness and refractive index were measured with ellipsometry using Sopra GES5 variable angle spectroscopic ellipsometer (Sopra Inc., Palo Alto, CA) and the accompanying GESPack software package. For electrical characterization, two aluminum rectangles of 5mm by 4.75mm were deposited through a shadow mask in a metal evaporator at separation of 0.5mm. A Kiethely 4200 Semiconductor Characterization System was used to perform current-voltage measurements.

4.3 Results and Discussion

4.3.1 Deposition Runs on Si substrate

Si/SiO_2 substrate is not an ideal substrate for measurement of electrical properties due to silicon oxide buffer layer. Therefore prior to depositing CCTO films on Si/SiO_2 substrate, preliminary depositions were performed on silicon substrate and XRD was used to confirm the growth of CCTO. Since as discussed earlier in this chapter, the highest dielectric constant is reported for Nb doped CCTO; therefore, $Nb(TMHD)_4$ was

also used as a dopant with precursor oven of 220 ºC. Capacitance and loss were measured with Agilent E4980a Precision LCR Meter with 10mV of 1 KHz frequency and DC bias of 1.0V. The measured values of samples for various deposition times are shown in Figure 4.4 and process parameters are shown in Table 4.3 for these devices. However, no CCTO peak was found in these devices.

On the closer observation of XRD of the film deposited on Si substrate, few peaks of Ca – Si compounds were observed as shown in Figure 4.5 P79 and 80. In Table 4.4, the deposition process parameters are given for sample P79 and P80. At the same time, it was found in the literature review that the formation of CCTO occurs on high temperatures (typically more than 750 ºC) [6]. But at higher temperatures, the formation of Ca – Si compounds was consuming the Ca from the reactant flow. To overcome this problem, silicon wafer was oxidized with 500 nm SiO_2 layer with thermal oxidation for future experiments.

4.3.2 CCTO thin film Deposition and XRD analysis on Si/SiO_2 substrate

As discussed in previous section, oxidized silicon wafer was used as a substrate due to reaction between Ca and Si. The final process parameters were decided by comparing XRD patterns of various samples as shown in Figure 4.6, for material composition and purity. Table 4.5 compares flow rates used to prepare samples labeled P93 through P97. In sample P93, the peak heights for CuO and Cu_2O were generally comparable to those of CCTO, indicating that the flow of copper precursor should be reduced to improve CCTO formation. Improved relative peak height for CCTO to CuO

was observed for sample P94 where the flow rate of copper precursor was reduced from 200 SCCM to 100 SCCM while maintaining the same flow rate for other precursors. On further reducing the flow rate of copper precursor to 50 SCCM in P95, formation of CuO was completely eliminated while again improving the relative ratio of CCTO to Cu_2O. Further reduction in the Cu precursor flow rate resulted in the formation of TiO_2 (samples P96 and P97).

Figure 4.7 shows the powder XRD pattern for the CCTO film deposited following the optimized conditions of sample P97 on Si/SiO_2 substrate. In the XRD pattern, CCTO is the major phase present in the film with (211), (220), (310), (321), (400) and (422) reflections (as compared to ICDD Card No 00-021-0140). In general, the nature of the CCTO film is polycrystalline. However, peaks for rutile TiO_2, Cu_2O and silicon substrate are also clearly visible on the XRD pattern. Even after optimizing the process by varying the precursor flow rates, these other phases were still present, though at lower levels than in preliminary experiments. It is also worth noting that use of commercially available precursors enhances the commercial viability of the process. In addition, the film thickness has been achieved in a very short deposition time of 15min.

In ellipsometry of CCTO thin films, the sample was scanned from 200 nm to 800 nm using an incident angle of 70° and an analyzer angle at 45°. The thickness of the CCTO film was calculated via the regression method in the Sopra WinElli software package (version 4.07). The thicknesses of CCTO and SiO_2 were about 190nm and 500nm, respectively. Ellipsometric measurements of CCTO thin films indicated a

refractive index of 3.03±0.06 which is very close to previously published results in reference [24, 25].

4.3.3 Surface Morphology Analysis of CCTO thin film on Si/SiO$_2$ substrate

Figure 4.8 shows the SEM image of the CCTO film on Si/SiO$_2$ substrate. The largest grain size present in the film is around 410 nm. However, the size distribution of grains is not uniform. A comparison of surface morphology of CCTO film on SiO$_2$ surface in the present work with previously published work will be of importance. Fang et. al. deposited CCTO thin films on SiO$_2$ thin layer at 700 ºC using PLD technique and found that SiO$_2$ surface has significant effect on the surface morphology of deposited CCTO thin film [26]. They also concluded that SiO$_2$ surface act as an initial nucleation layer for CCTO films and results in better crystallinity. Further the work published in Ref. [27], CCTO thin film was deposited using MOCVD process on Si/SiO$_2$ substrate at the same deposition temperature (750 ºC) as this work but for longer time (45 min vs. 15 min of this work) with grain size varying from 80 nm to 300 nm. Authors of Ref. [27] also reported some interaction between CCTO and SiO$_2$ layer at the interface.

4.3.4 Sheet Resistance Measurements of CCTO thin film on Si/SiO$_2$ substrate

Electrical characterization was done by depositing two aluminum metal pads on the CCTO thin film and applying electrical bias as shown in Figure 4.9 (a). The two metal electrodes were separated by 0.5mm. Current-voltage (I-V) measurements taken for a film thickness of about 190 nm is shown in Figure 4.9 (b). I-V measurement shows a

surface current of 6.44nA at 1V on the CCTO thin film. To estimate sheet resistance of the CCTO thin film, electrical potential of 5V was applied to one metal pad, while the other metal pad was connected to common. Sheet resistance (R_s) of the film is given by [28],

$$R_s = \frac{V}{I} \cdot \frac{w}{d}$$

where, w is the width of metal electrodes and d is the separation between two electrodes. Using above formula, the calculated sheet resistance of sample (P97) is 1.61×10^9 Ω per square or sheet conductivity is 6.21×10^{-10} S per square. To estimate measurement error for given electrode structure, we also measured surface resistance on two other substrates, a corning glass microscope slide and a glass-reinforced epoxy FR4 board. On each substrate, two different electrode structures were used. One of the two electrode structures was two rectangular metal pads as described in the Figure 4.9(a), and the other one was two concentric circular electrodes. The measurement results were consistent within order of magnitude for both electrode structures on respective substrates. Therefore, the sheet resistance for the CCTO thin film can be estimated to be 10^9 Ω per square.

4.3.5 Deposition Runs on Si/SiO_2/metal substrate

The major disadvantage of Si/SiO_2 substrate is that we could not calculate dielectric constant using a direct technique such as LCR meter or Q-V curve analysis. As

described in earlier section of this chapter, Si substrate was reacting with Ca precursor for Ca-Si-O compounds. Therefore in this work, we also tried to deposit CCTO film on platinum substrate. To prepare platinum substrate, platinum was thermally evaporated on same Si/SiO_2 substrate using Edward thermal evaporator. The optimized deposition process as given in Table 4.2 was used for the experiment and XRD analysis was performed to verify the film composition. Figure 4.10 shows XRD pattern of sample P98 which is a Si/SiO_2/Pt substrate. In the XRD pattern of P98, no CCTO peak was found. However, few peaks of $CaTiO_2$ and CuO were present. Several samples were tried after that, but no samples could show CCTO peak.

4.3.6 Dielectric Constant Measurements Techniques

Since CCTO thin films deposition discussed in this chapter, is performed on Si/SiO_2 substrate, dielectric constant measurements could not be made. However, two measurement techniques were explored on film deposited on silicon substrate to measure capacitance and to calculate dielectric constant. The first technique uses LCR meter (Agilent Technologies E4980A) to measure capacitance. LCR meter measures impedance by applying an AC signal at a given frequency and calculates capacitance. It is critical to use correct settings of the instrument before performing the measurements, otherwise measurements could be misleading. On the process of capacitance measurement, LCR meter gives capacitance value as well as loss factor. Loss factor is a measure of charge holding capability of a capacitor. Ideally, a capacitor should have a zero loss factor. Therefore for lower loss factor, the capacitor can hold the charge for longer time. If the

capacitor is very leaky, capacitance varies for different frequencies. The minimum frequency of LCR meter is 20 Hz and there is no option for DC (zero frequency) capacitance measurements.

The second technique uses DC current source and measures change in voltage over time. For DC capacitance measurement, a current source given in Kiethely 4200 Semiconductor Characterization System was used. The main advantage of Kiethely system is that operator can set a voltage limit (compliance) for the constant current source. The basic principle of this method is $C = \Delta Q / \Delta V$ where, C is capacitance, ΔQ is the charge supplied, and ΔV is rise in voltage. Further ΔQ is product of current supplied from constant current source and time to charge the capacitor with ΔV. All these values can be easily read directly from the instrument. Selection of charging current is an important factor in this measurement. It is highly recommended that prior to capacitance measurement, I-V measurement should be done on the same device to select the charging current. The charging current must be several times of the leakage current at given voltage to avoid error due to charge leakage while capacitor is charging. For example, Table 4.6 shows possible combinations of leakage current and charging current for a device P47 C5P6. This device was a test run (Al/Si/film/Al) and did not have any CCTO peak. The process parameters for P47 are given in Table 4.3 with deposition time for 6 min. To minimize the error in calculations, the leakage charge (or current) can be subtracted from the supplied charge (or current) as shown in Table 4.7. Figure 4.11 shows a Q vs. V curve for a capacitor measured with Keithely system using DC method for above device, where the capacitance could be measured directly from the slope of the

curve. It is interesting to note that as the leakage current is increasing the number of measurement points in the curve are reducing. This method is a direct DC measurement technique can be used to calculate capacitance and then dielectric constant.

To confirm above measurement techniques, capacitance of SiO_2 film were measured using the device structure shown in Figure 4.9. The structure Al/SiO_2/Si/SiO_2/Al contains two capacitors of Al/SiO_2/Si and Si/SiO_2/Al in series. Each metal pad was used as an electrode in the measurement. The calculated and measured values of capacitance for above structure are shown in Table 4.8. Similar measurements were performed on sample P94 and P96 to estimate CCTO capacitance as shown in Table 4.9. As mentioned earlier, there is possibility of interaction between CCTO film and SiO_2 layer too [27]. Therefore, it is difficult to estimate the dielectric constant from these calculations. The ideal device structure to estimate dielectric constant will be metal/insulator/metal.

4.4 Conclusion

We deposited CCTO thin film on the Si/SiO_2 substrate using a photo-assisted MOCVD process in a custom designed non-commercial automated system. The process was optimized by controlling the flow rate of precursors, process temperatures, and deposition time. The optimized process still had some impurities of rutile TiO_2 and Cu_2O, but high energy photon assisted MOCVD has showed CCTO grains with grain sizes as large as 410 nm. The CCTO film has been characterized with ellipsometry, powder XRD, and SEM techniques. Ellipsometry indicates the refractive index of the film is 3.03±0.06.

References

[1] R. K. Grubbs, E. L. Venturini, P. Clem, J. J. Richardson, B. A. Tuttle and G. A. Samara, "The very large dielectric constant of $CaCu_3Ti_4O_{12}$: An inhomogeneous semiconductor", Science for National Security Needs, Sandia National Lab, 2004.

[2] M. A. Subramanian, D. Li, N. Duan, B. A. Reisner and A. W. Sleight, “High dielectric constant in $ACu_3Ti_4O_{12}$ and $ACu_3Ti_3FeO_{12}$ phases”, Journal of Solid State Chemistry 151(2), pp. 323-325. 2000.

[3] W. Lu, L. Feng, G. Cao and Z. Jiao, “Preparation of $CaCu_3Ti_4O_{12}$ thin films by chemical solution deposition”, J. Mater. Sci., vol. 39, issue 10, pp. 3523-3524, 2004.

[4] S. Jin, H. Xia, Y. Zhang, J. Guo and J. Xu, “Synthesis of $CaCu_3Ti_4O_{12}$ ceramic via a sol-gel method”, Mater Lett, vol. 61, issue 6, pp. 1404-1407, 2007.

[5] W. Si, E. M. Cruz, P. D. Johnson, P. W. Barnes, P. Woodward and A. P. Ramirez, “Epitaxial thin films of the giant-dielectric-constant material $CaCu_3Ti_4O_{12}$ grown by pulsed-laser deposition”, Appl. Phys. Lett., vol. 81, issue 11, article no. 2056, 2002.

[6] R. Lo. Nigro, R. G. Toro, G. Malandrino, M. Bettinelli, A. Speghini and I. L. Fragalà, “A Novel Approach to Synthesizing Calcium Copper Titanate Thin Films with Giant Dielectric Constants”, Adv Mater, vol. 16, issue 11, pp. 891-895, 2004.

[7] G. Cao, L. Feng and C. Wang, “Grain-boundary and subgrain-boundary effects on the dielectric properties of $CaCu_3Ti_4O_{12}$ ceramics”, J. Phys. D, vol. 40, issue 9, pp. 2899-2905, 2007.

[8] B. Khumpaitool and J. Khemprasit, “Improvement in dielectric properties of Al2O3-doped $Li_{0.30}Cr_{0.02}Ni_{0.68}O$ ceramics”, Mater Lett, vol. 65, issue 6, pp. 1053-1056, 2011.

[9] L. Wu, Y. Zhu, S. Park, S. Shapiro, G. Shirane and J. Tafto, “Defect structure of the high-dielectric-constant perovskite $CaCu_3Ti_4O_{12}$”, Physical Review B, vol. 71, issue 1, article no. 014118, 2005.

[10] P. Lunkenheimer, S. Krohns, S. Riegg, S. G. Ebbinghaus, A. Reller and A. Loidl, “Colossal dielectric constants in transition-metal oxides”, The European Physical Journal - special topics, vol. 180, no. 1, pp. 61-89, 2010.

[11] M. C. Ferrarelli, D. C. Sinclair, A. R. West, H. A. Dabkowska, A. Dabkowski and G. M. Luke, “Comment on the origin(s) of the giant permittivity effect in $CaCu_3Ti_4O_{12}$ single crystals and ceramics”, Journal of Materials Chemistry, vol. 19, issue 33, pp. 5916-5919, 2009.

[12] P. Fiorenza, R. Lo Nigro, A. Sciuto, P. Delugas, V. Raineri, R. G. Toro, M. R. Catalano and G. Malandrino, “Perovskite $CaCu_3Ti_4O_{12}$ thin films for capacitive applications: From the growth to the nanoscopic imaging of the permittivity”, J. Appl. Phys., vol. 105, issue 6, article no. 061634, 2009.

[13] W. X. Yuan and Z. J. Li, “Microstructures and dielectric properties of $CaCu_3Ti_4O_{12}$ ceramics via combustion method”, The European Physical Journal Applied Physics, vol. 57, issue 1, article no. 11302, 2012.

[14] Y. Chen, R. Singh, G. Li and G. H. Haertling, “A study of rapid photothermal annealing of sputtered lead lanthanum zirconia titanate thin films”, J. Electrochem. Soc., vol. 145, issue 12, pp. 4317-4322, 1998.

[15] Y. Chen, R. Singh and J. Narayan, “Deposition of tantalum oxide films by dual spectral source assisted metalorganic chemical vapor deposition (MOCVD)”, J Electron Mater., vol. 26, issue 4, pp. 350-354, 1997.

[16] A. Venkateshan, R. Singh, K. F. Poole, J. Harriss, H. Senter, R. Teague and J. Narayan, “High- gate dielectrics with ultra-low leakage current for sub-45 nm CMOS”, Electron. Lett., vol. 43, issue 21, pp. 1130-1131, 2007.

[17] R. Singh and Y. Chen, “Role of high energy photons in dual spectral source rapid isothermal CVD”, J Electron Mater, vol. 26, issue 10, pp. 1184-1188, 1997.

[18] R. Singh, S. Sinha, R. P. S. Thakur and N. J. Hsu, “Role of photoeffects in integrated rapid isothermal processing”, MRS Proceedings, vol. 224, pp. 197-201, 1991.

[19] R. Singh, R. Sharangpani, K. C. Cherukuri, Y. Chen, D. M. Dawson, K. F. Poole, A. Rohatgi, S. Narayanan and R. P. S. Thakur, “How rapid isothermal processing can be a dominant semiconductor processing technology in the 21st century”, MRS Proceedings, vol. 429, pp. 81-94, 1996.

[20] R. Singh, M. Fakhruddin and K. F. Poole, “Rapid photothermal processing as a semiconductor manufacturing technology for the 21st century”, Appl. Surf. Sci., vol. 168, issue 1-4, pp. 198-203, 2000.

[21] Ratnakaran, V., vratnakaran@xenoncorp.com (2012) Spectrum. [email] Message to Gupta, N. (ngupta@g.clemson.edu). Sent 16th Feb.

[22] R. Singh, L. Vedula and C. Gong, "Dependence of activation energy of mass transport limited region on the photospectrum of photons participating in rapid photothermal assisted chemical vapor deposition", J Electron Mater, vol. 27, issue 3, pp. L13-L16, 1998.

[23] R. Singh and V. Parihar, "rapid photothermal processing of dielectrics", In: H. S. Nalwa (Ed.), Handbook of low and high dielectric constant materials and their applications; ch. 2, pp. 1-59, 1999.

[24] T. Ning, C. Chen, Y. Zhou, H. Lu, D. Zhang, H. Ming and G. Yang, "Large optical nonlinearity in $CaCu_3Ti_4O_{12}$ thin films", Applied Physics A, vol. 94, issue 3, pp. 567-570, 2009.

[25] G. Li, Z. Yin and M. Zhang, "Study on optical and dielectric properties of $CaCu_3Ti_4O_{12}$ by first-principles calculation", Materials Science and Engineering: B, vol. 150, issue 3, pp. 163-167, 2008.

[26] L. Fang, M. Shen, J. Yang, Z. Li, J. Phy. D: Appl. Phys., vol. 38, pp. 4236 – 4240, 2005.

[27] R. Lo Nigro, R. G. Toro, G. Malandrino, I. L. Fragalà, P. Fiorenza and V. Raineri, "Chemical stability of $CaCu_3Ti_4O_{12}$ thin films grown by MOCVD on different substrates", Thin Solid Films, vol. 515, issue 16, pp. 6470-6473, 2007.

[28] J.W. Mayer, S.S. Lau, In: D. Johnstone (Ed.), Electronic Materials Science: For Integrated Circuits in Si and GaAs, Mcmillan Publishing Company, New York, U.S.A., 1990, p. 35.

[29] G. Arlt, D. Hennings and G. de With, "Dielectric properties of fine-grained barium titanate ceramics", J. Appl. Phys. 58(4), pp. 1619, 1985.

[30] S. Q. Zhang, W. L. Li, L. D. Wang, N. Li and W. D. Fei, "Enhanced dielectric and ferroelectric properties of $Pb_{1-3x/2}La_x(Zr_{0.5}Ti_{0.5})O_3$ thin films with low lanthanum substitution", Appl. Surf. Sci. 257(9), pp. 4021-4025, 2011.

[31] X. Kuang, C. Bridges, M. Allix, J. B. Claridge, H. Hughes and M. J. Rosseinsky, "Internal barrier layer capacitance effect in hexagonal perovskite $Ba_4YMn_3O_{11.5}$ ceramics", Chemistry of Materials 18(21), pp. 5130-5136, 2006.

[32] X. Q. Liu, Y. J. Wu and X. M. Chen, "Giant dielectric response and polaronic hopping in charge-ordered $Nd_{1.75}Sr_{0.25}NiO_4$ ceramics", Solid State Commun. 150(37-38), pp. 1794-1797, 2010.

[33] Z. Wang, X. M. Chen, L. Ni, Y. Y. Liu and X. Q. Liu, "Dielectric relaxations in $Ba(Fe_{1/2}Ta_{1/2})O_3$ giant dielectric constant ceramics", Appl. Phys. Lett. 90(10), pp. 102905, 2007.

[34] S. Sarkar, P. K. Jana, B. K. Chaudhuri and H. Sakata, "Copper (II) oxide as a giant dielectric material", Appl. Phys. Lett. 89(21), pp. 212905, 2006.

[35] P. K. Jana, S. Sarkar and B. K. Chaudhuri, "Low loss giant dielectric and electrical transport behavior of $K_xTi_yNi_{1-x-y}O$ system", Appl. Phys. Lett. 88(18), pp. 182901, 2006.

[36] C. Pecharroman, F. Esteban-Betegon, J. F. Bartolome, S. Lopez-Esteban and J. S. Moya, "New percolative $BaTiO_3$-Ni composites with a high and frequency-independent dielectric constant (εr ≈ 80000)", Adv. Mater. 13(20), pp. 1541-1544, 2001.

[37] M. M. Ahmad and K. Yamada, "Superionic $PbSnF_4$: A giant dielectric constant material", Appl. Phys. Lett. 91(5), article no. 052912, 2007.

[38] K. Majhi, B. Shri Prakash and K. B. R. Varma, "Extreme values of relative permittivity and dielectric relaxation in Sr_2SbMnO_6 ceramics", J. Phys. D 40(22), pp. 7128-7135, 2007.

[39] S. Saha, "Observation of giant dielectric constant in an assembly of ultrafine Ag particles", Physical Review B 69(12), 2004.

Table 4.1: Published Results at room temperature (300K) and 1KHz

Material	Dielectric Constant	Synthesis Route	Reference
$BaTiO_3$	$4.6x10^2$	Solid State	[29]
PLZT	$1.75x10^3$	Sol-Gel	[30]
$Ba_4YMn_3O_{11.5}$	$1.0x10^4$	Solid State	[31]
$Nd_{1.75}Sr_{0.25}NiO_4$	$1.0x10^4$*	Solid State	[32]
$Ba(Fe_{1/2}Ta_{1/2})O_3$	$2.0x10^4$	Solid State	[33]
CuO	$2.0x10^4$	Solid State	[34]
$K_{0.05}Ti_{0.02}Ni_{0.93}O$	$2.0x10^4$	Solid State	[35]
Ni doped $BaTiO_3$	$6.5x10^4$	Wet Processing	[36]
$PbSnF_4$	$1.0x10^5$	Solid State	[37]
Sr_2SbMnO_6	$1.87x10^5$	Solid State	[38]
$CaCu_3Ti_{3.8}Nb_{0.2}O_{12}$	$1.0x10^6$	Solid State	[7]
Al_2O_3-doped $Li_{0.30}Cr_{0.02}Ni_{0.68}O$	$7.25x10^6$	Sol Gel Process	[8]
Ultrafine Ag Particles	10^{10}	Electrochemical	[39]

* at 10KHz

Table 4.2: Process gas and precursor oven parameters for sample P97

Precursor/Process Gas	Gas Flow Rate (sccm)	Precursor Oven Temperature
$Ca(TMHD)_2$	200	230 ºC
$Cu(TMHD)_2$	50	120 ºC
$C_{12}H_{28}O_4Ti$	25	25 ºC
Forming Gas (20% H_2 – 80% N_2)	20	--
UHP O_2	80	--
N_2O	40	--

Table 4.3: Process parameters for the devices shown in Figure 4.4 for (a) in-situ cleaning cycle, (b) deposition cycle, and (c) annealing cycle

(a) Cleaning Cycle

Temperature	Time	Cleaning Gas	Flow Rate
950 ºC	6 min	Forming Gas	20 sccm

(b) Deposition Cycle

Precursor/Process Gas	Gas Flow Rate (sccm)	Precursor Oven Temperature
$Ca(TMHD)_2$	5	220 ºC
$Cu(TMHD)_2$	5	165 ºC
$C_{12}H_{28}O_4Ti$	5	40 ºC
$Nb(TMHD)_4$	5	220 ºC
UHP O_2	6	--
N_2O	20	--
Deposition Temperature	400 ºC	

(c) Annealing Cycle

Temperature	Time	Annealing Gas	Flow Rate
750 ºC	20 min	UHP O_2	40 sccm

Table 4.4: Process parameters for sample P79 and P80

Precursor/Process Gas	Gas Flow Rate (sccm)	Precursor Oven Temperature
$Ca(TMHD)_2$	150	230 ºC
$Cu(TMHD)_2$	50	120 ºC
$C_{12}H_{28}O_4Ti$	1	25 ºC
Forming Gas (20% H_2 – 80% N_2)	20	--
UHP O_2	40	--
N_2O	20	--

Table 4.5: Comparison of precursor flow rates used in various samples

Sample	Ca Precursor Flow Rate (sccm)	Cu Precursor Flow Rate (sccm)	Ti Precursor Flow Rate (sccm)
P93	200	200	50
P94	200	100	50
P95	200	50	50
P96	200	25	50
P97	200	50	25

Table 4.6: Capacitance measurements for P47C5P6; Device area: 0.00785 cm^2

Compliance (V)	Leakage Current (A/cm^2)	Charging Current (A)	Capacitance calculated (F/cm^2)
-.1	-8.11×10^{-10}	-100p	9.53×10^{-07}
-.2	-1.00×10^{-09}	-200p	9.36×10^{-07}
-.4	-5.08×10^{-09}	-450p	9.32×10^{-07}
-.5	-1.31×10^{-08}	-1n	9.16×10^{-07}
-.6	-3.48×10^{-08}	-3n	8.93×10^{-07}
-.7	-8.68×10^{-08}	-10n	8.8×10^{-07}
-.8	-1.74×10^{-07}	-15n	8.73×10^{-07}
-.9	-4.19×10^{-07}	-10n	8.99×10^{-07}
-1.0	-8.32×10^{-07}	-10n	9.39×10^{-07}

Table 4.7: Adjusted capacitance for P47C5P6; Device area: 0.00785 cm^2

Compliance (V)	Capacitance before ($Q-Q_L$) (F/cm^2)	Capacitance after ($Q-Q_L$) (F/cm^2)
-0.1	9.53×10^{-07}	9.71×10^{-07}
-0.2	9.36×10^{-07}	9.48×10^{-07}
-0.4	9.32×10^{-07}	9.10×10^{-07}
-0.5	9.16×10^{-07}	9.38×10^{-07}
-0.6	8.93×10^{-07}	8.74×10^{-07}
-0.7	8.8×10^{-07}	8.62×10^{-07}
-0.8	8.73×10^{-07}	8.52×10^{-07}
-0.9	8.99×10^{-07}	8.41×10^{-07}
-1.0	9.39×10^{-07}	8.27×10^{-07}

Table 4.8: Capacitance calculations and measurements for $Al/SiO_2/Si/SiO_2/Al$ structure

Capacitance Calculations for $Al/SiO_2/Si$	Capacitance Measurement with LCR meter	Capacitance Measurement with DC Technique
Area (A) = 5 mm x 4.75 mm	$C_{LCR} = 671 pF$	Charging Current = -1 nA
$\kappa = 3.9$		Compliance Voltage = 1V
$\varepsilon_0 = 8.854 \times 10^{-12}$ F/m		Leakage Current @ -1V < -1 pA
Thickness (d) = 566 nm		$C_{DC} = 742\ pF$
Capacitance $C = \frac{\varepsilon_0 \kappa A}{d} =$ 1.4489 nF		
For two capacitors in series $Al/SiO_2/Si/SiO_2/Al$:		
$C_s = \frac{C}{2} = 724.5\ pF$		

Table 4.9: Capacitance measurements for Al/CCTO/SiO_2/Si/SiO_2/CCTO/Al structure for (a) P94 and (b) P96

(a) P94

Capacitance Measurement with LCR meter	Capacitance Measurement with DC Technique
$C_{LCR} = 471pF$	Charging Current = -1 nA
Loss = 0.04	Compliance Voltage = 1V
	Leakage Current @ -1V = - 89 pA
	$C_{DC} = 876\ pF$

(b) P96

Capacitance Measurement with LCR meter	Capacitance Measurement with DC Technique
$C_{LCR} = 571\ pF$	Charging Current = -10 nA
Loss = 0.03	Compliance Voltage = 1V
	Leakage Current @ -1V = - 7.1 nA
	$C_{DC} = 1.04\ nF$

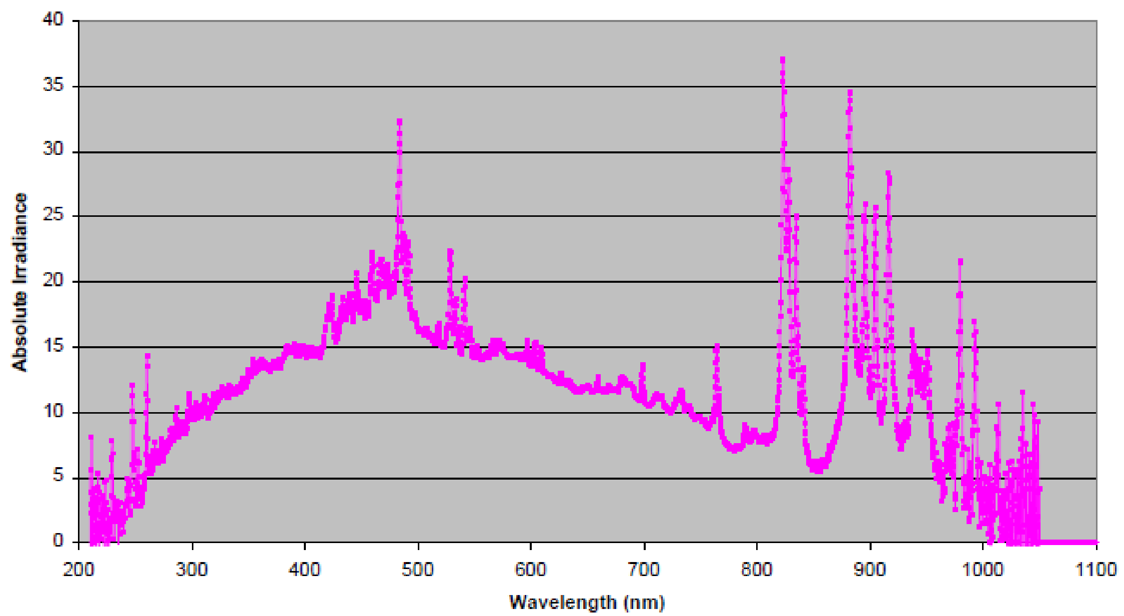

Figure 4.1: Spectrum of Xenon Flash Lamp used in Photo-assisted MOCVD system [21]

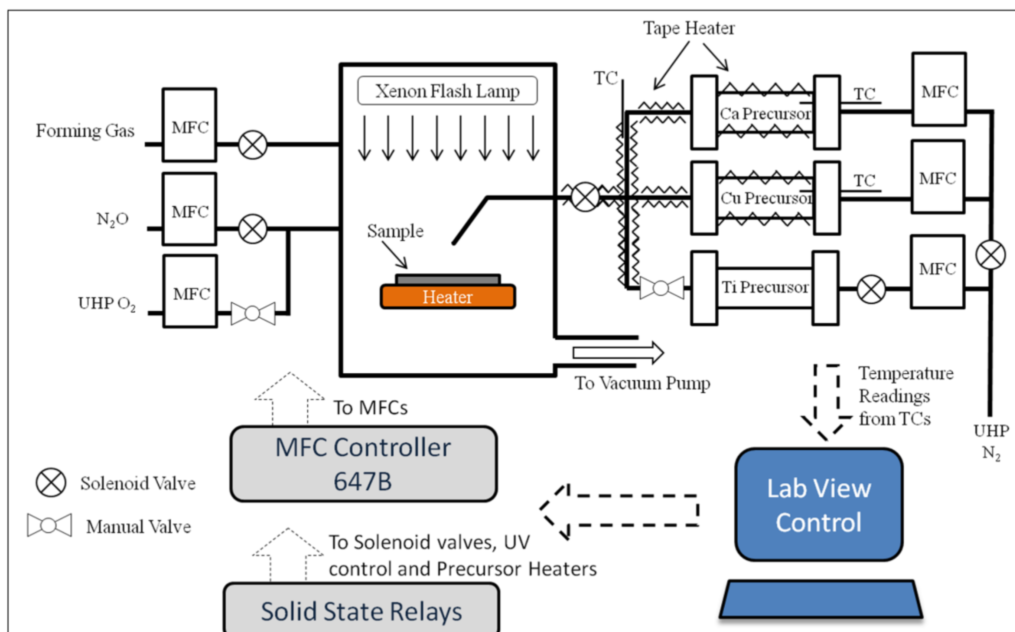

Figure 4.2: Photo-assisted MOCVD Process setup with computer control

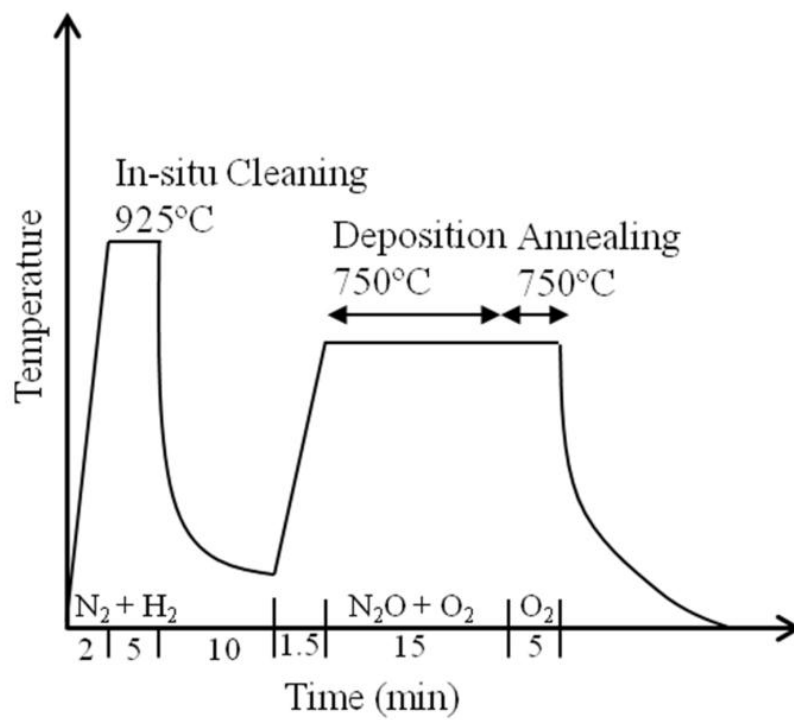

Figure 4.3: Thermal cycle for the CCTO photo-assisted MOCVD process. For the In-situ cleaning, deposition and annealing cycles, incoherent light source was ON.

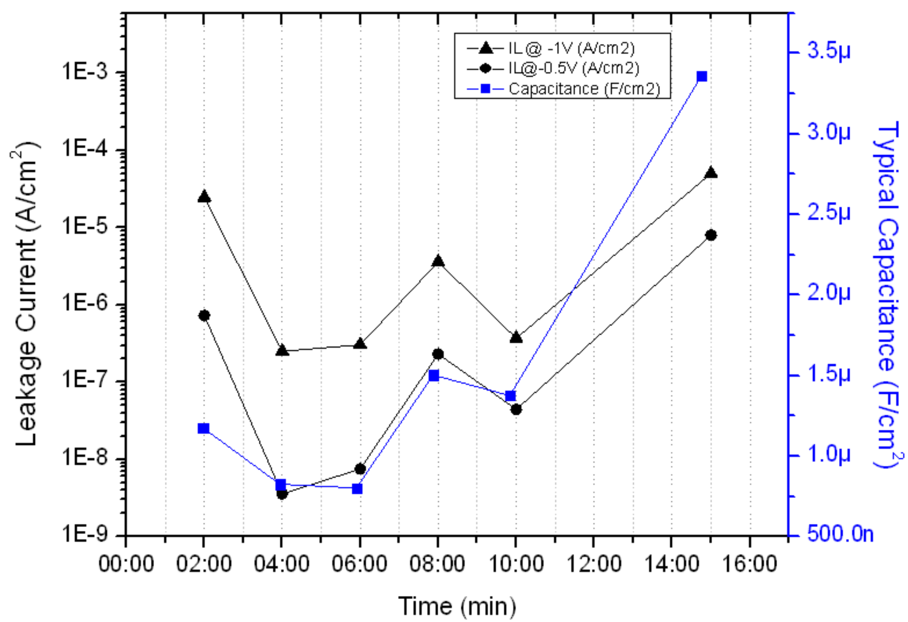

Figure 4.4: Leakage current, typical capacitance vs. deposition time for the films deposited on silicon wafer with structure Al/Si/film/Al; Device area: 0.00785 cm^2

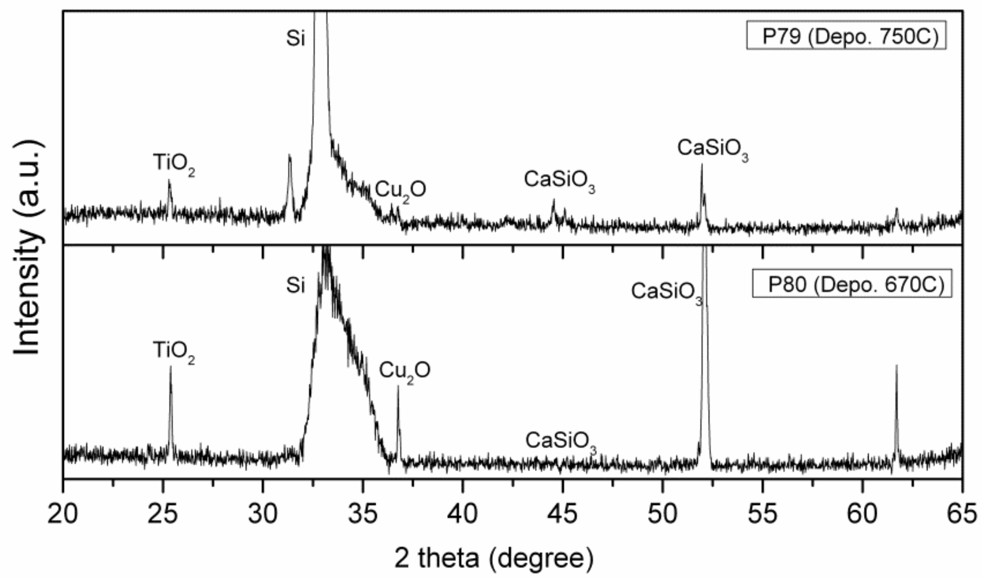

Figure 4.5: XRD analysis of films deposited on silicon substrate.

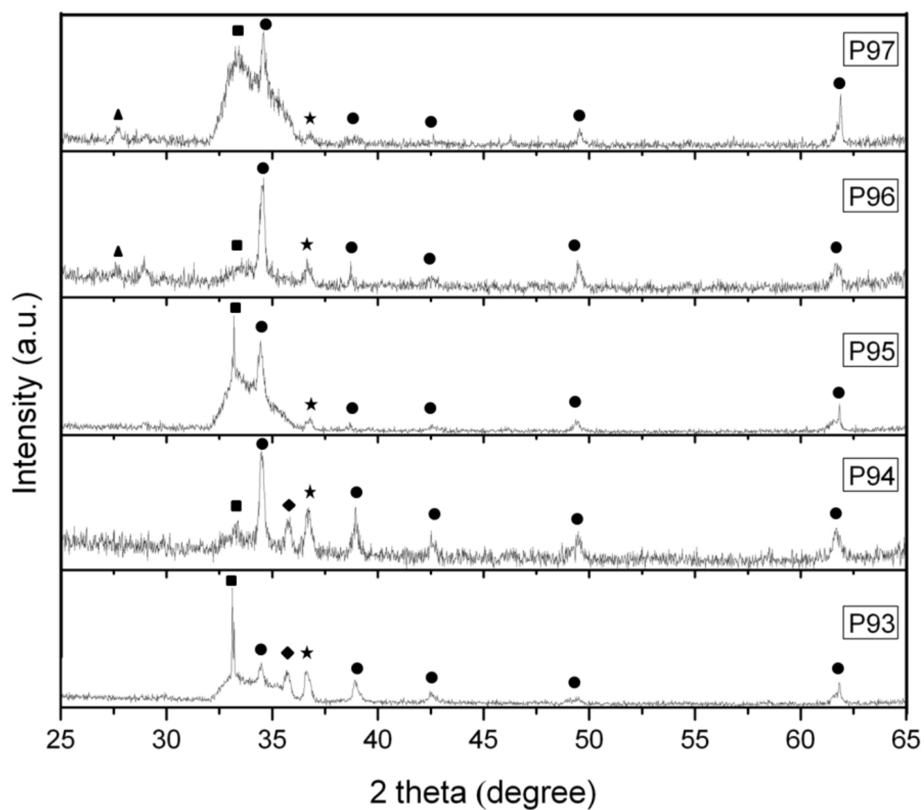

Figure 4.6: Comparison of XRD patterns of various samples. Where, CCTO, CuO, Cu_2O, TiO_2, Substrate (Si) are labeled as ●, ♦, ★, ▲ and ■ respectively.

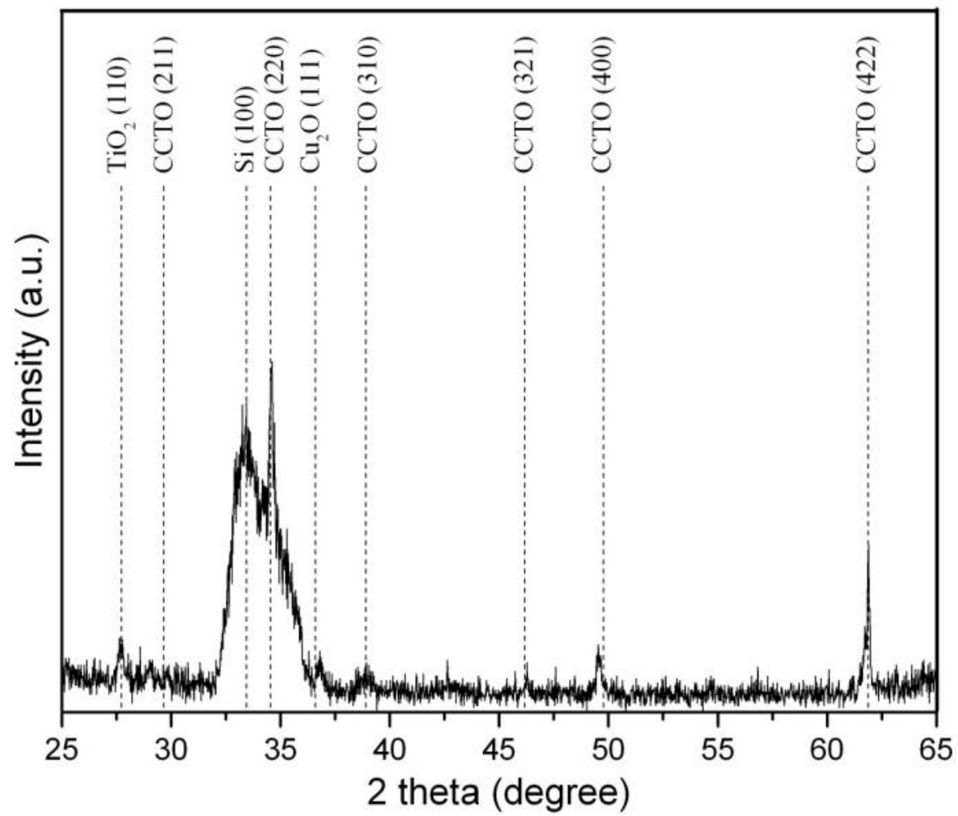

Figure 4.7: XRD for the CCTO thin film from sample P97.

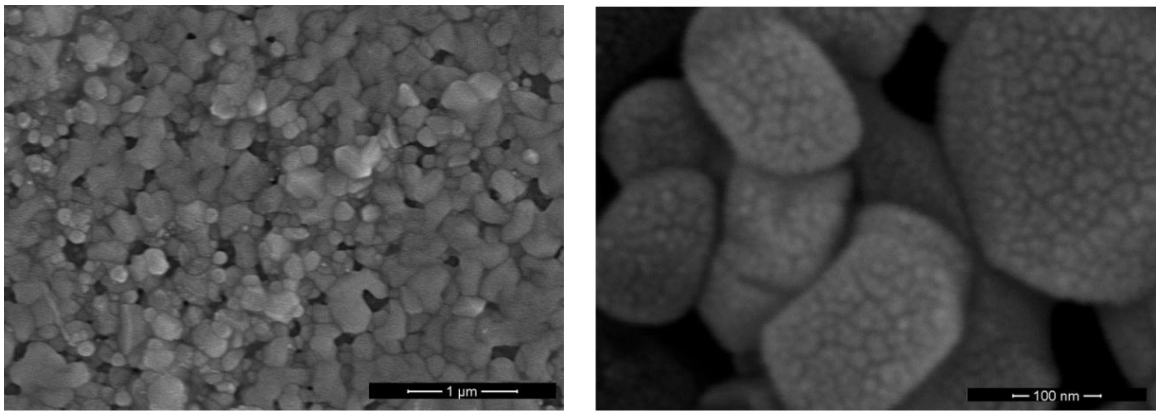

Figure 4.8: SEM image of the CCTO thin film

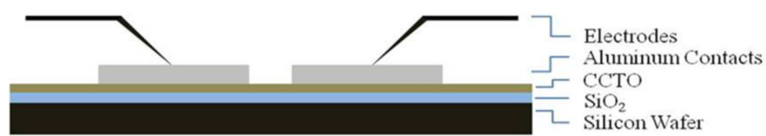

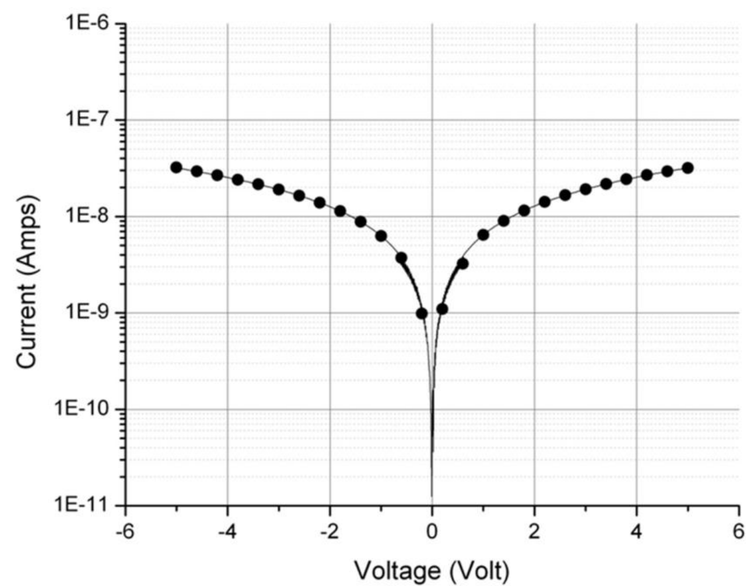

Figure 4.9: Electrical measurements setup (Top) and Current-Voltage characteristics (Bottom)

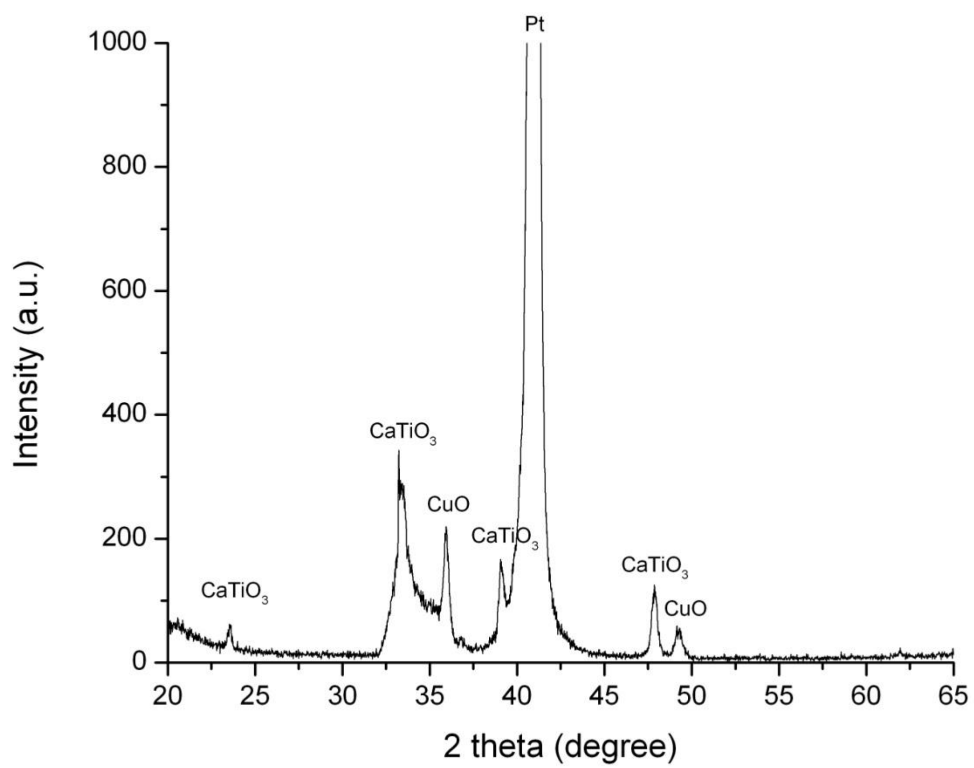

Figure 4.10: XRD for the thin film deposited on $Si/SiO_2/Pt$ (sample P98).

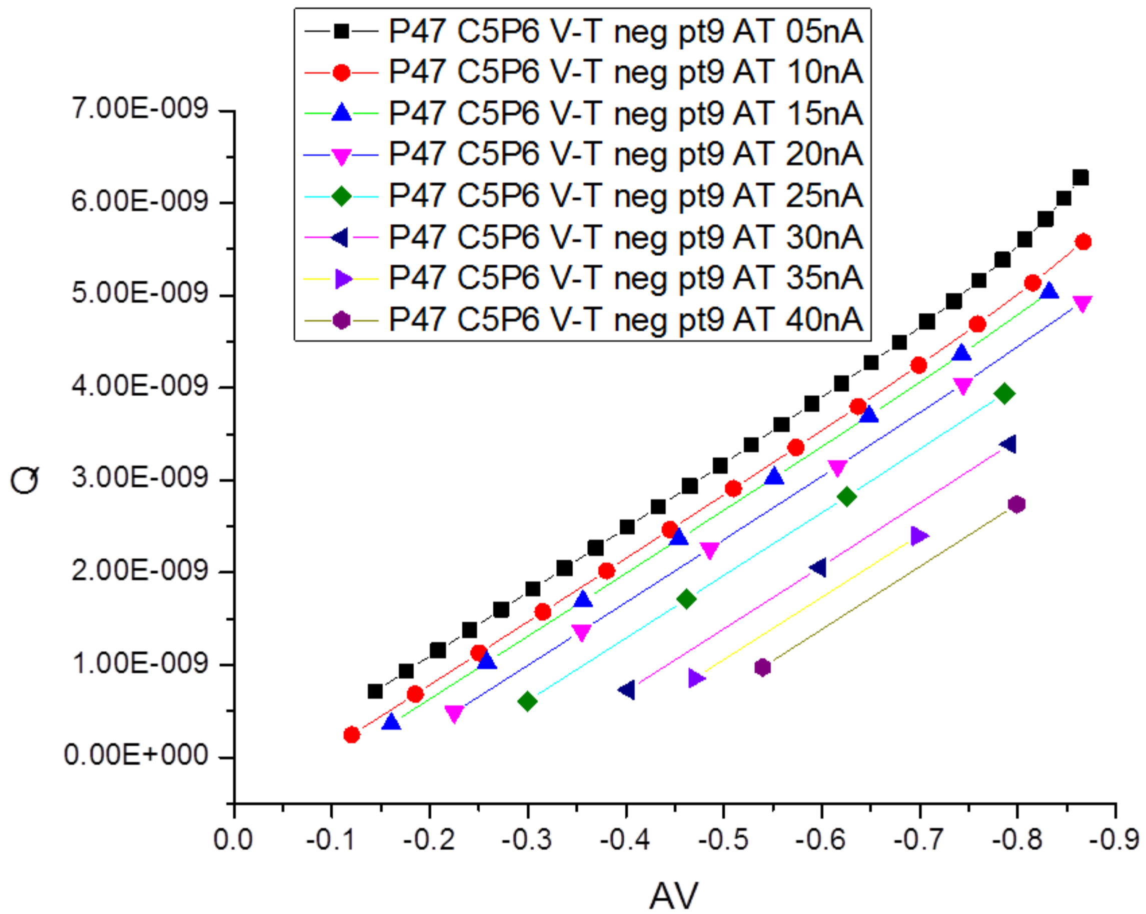

Figure 4.11: The effect of charging current in measurement of capacitance using DC method

CHAPTER FIVE

DEPOSITION AND CHARACTERIZATION OF NANOSTRUCTURED Cu_2O THIN-FILM FOR POTENTIAL PHOTOVOLTAIC APPLICATIONS

This chapter is based on a journal article submitted for publication as *N. Gupta, R. Singh , F. Wu, J. Narayan, C. McMillen, G. F. Alapatt, K. F. Poole, S.-J. Hwu, D. Sulejmanovic, M. Young, G. Teeter and H. S. Ullal, "Deposition and Characterization of Nanostructured Cu_2O Thin-film for Potential Photovoltaic Applications".*

.

5.1 Introduction

The cost of photovoltaic (PV) modules in the last five decades has decreased exponentially. The growth rate of the global PV market was about 70% per year from 2007 to 2011 [1]. In 1980, one of us [2] published a paper on the economic requirements for new materials for solar cells and predicted that silicon was the best choice for terrestrial applications of solar cells. Over the last 32 years this prediction has been correct, since about 90% solar cells manufactured currently are made out of bulk silicon. Highest demonstrated AM1.5G efficiency of a passivated emitter with rear locally-diffused (PERL) crystalline silicon solar cells is 25% [3]. Using commercial-grade p-type silicon wafers, recent work of Wang et al. [4] has led to the development of a commercial version of the PERL cell with a record production-level AM1.5G efficiency of 20.3%. Without the use of trackers, further increase in the efficiency of bulk silicon solar cells will be achieved by the use of multi-junction solar cells [5]. For the new

materials, the cost of the raw materials and their atomic concentration in the earth's crust can give a good indication of the relative cost of that material in a large-scale application. For generating PV electricity at lower cost ($/ kWH) than conventional energy sources, the following criteria must be used in choosing appropriate PV module manufacturing technology (a) no material supply constraints, (b) lowest cost of ownership, (c) lowest production cost, (d) the prospect of further cost reduction, and (e) environmental safety and health issues (ESH) and green manufacturing [2, 6-8].

Low-cost is the driver of growth and can happen only for the solar cells manufactured with most abundant raw materials [2, 6-8]. Like silicon, copper is also one of the most abundant and non-toxic element in the earth crust with annual global production of about 16.1 million tons [9] and has the potential to be used in solar cell manufacturing. In this work, we have investigated copper (I) oxide films deposited on a silicon substrate using photo-assisted metal-organic chemical vapor deposition for potential photovoltaic applications.

5.2 Background Material

The best bulk silicon solar cell efficiency reported to date is about 25%, and the maximum single junction theoretical efficiency is about 33% [10]. Further significant increases in efficiency of silicon solar cells are unlikely to take place without the use of multi-junction device structures capable of converting a larger fraction of the spectrum into useful electrical energy. Considering the simplest case of a multi junction cell, a two-

junction cell with silicon as the bottom layer, the highest efficiency calculated from the black body limit is 44% when the band gap of the top material is 1.8 eV. If realized, this increase in efficiency will further reduce the cost of PV-generated power. Semiconductors consisting of abundant materials can be used as the top layer to boost the efficiency of silicon solar cells. The reported band gap of the Cu_2O film ranges from 1.7 eV to 2.6 eV [11-13]. Therefore, Cu_2O fits reasonably well as a promising top layer semiconducting material. Assuming Cu_2O band gap of about 2.0 eV, the theoretical calculations have shown maximum AM1 efficiency for Cu_2O solar cell is approximately 22% with a required leakage current density at zero bias (J_0) of 4×10^{-28} A/cm^2 while to achieve a practical efficiency of 9 - 11% with a required J_0 of about 10^{-17} A/cm^2 [14].

Copper (I) oxide (Cu_2O) is a direct band gap semiconductor with p-type conductivity. Photovoltaic effect based on copper (I) oxide or Cu_2O device was first observed in 1917 by Kennard and Dieterich [15]. Cu_2O has several excellent properties such as very high absorption coefficient (in the range of 10^5 cm^{-1}) for above-band gap wavelengths, good majority-carrier mobility (≈ 90 cm^2/V.s) and minority carrier diffusion length of the order of 3.5 μm [16]. After the invention of silicon and germanium diodes, interest in copper (I) oxide based devices declined. Renewed interest started after energy crisis of 1973, and several researchers investigated Cu_2O again as a potential PV material. Several methods such as thermal oxidation [17], pulsed laser deposition [18], chemical vapor deposition (CVD) [19], electrochemical deposition [20], thermal evaporation [21], and sputtering [22] etc., have been investigated to fabricate Cu_2O based

solar cells. However, to date the maximum efficiency of only 2% has been reported for copper (I) oxide solar cells under AM1.5G spectrum [17].

As a thermal processing technique, rapid photothermal processing (RPP) has proved to be a superior technique [23-26]. The operating mechanisms are described in references [23] and [27]. The quantum effects associated with photons with wavelength below about 800 nm have the following implications for the photo-assisted CVD process;

1. At a given processing temperature, the bulk and surface diffusion coefficients are enhanced.
2. The processing cycle time is reduced.
3. Due to lower microscopic defects, devices and circuits with higher performance, better reliability and yield are obtained.

5.3 Experimental Details

5.3.1 Photo-assisted MOCVD System

A custom-designed non-commercial MOCVD system with Xenon flash lamp as the source of incoherent UV photons, (Figure 5.1), was used to deposit Cu_2O thin film on n-type Si <100> substrate. Bis(2,2,6,6 tetramethyl 3,5-heptanedionato)copper(II) [$Cu(TMHD)_2$] with purity of 99% was used as the precursor for the deposition of copper oxide films. The precursor used in this work was used as purchased from Strem Chemicals without any modifications. Based on our previous experience of depositing high quality thin films of oxides, nitrous oxide and ultra-high purity (UHP) oxygen were used as the reaction gases [23]. As shown in Figure 5.1, the precursor was kept in a

heated stainless steel oven and connected by a heated line to the deposition chamber. The temperature in the precursor oven were monitored with a K type thermocouple and controlled with LabVIEW modules. The UV photon source, mass flow controllers (MFCs) and solenoid gas valves were also controlled with LabVIEW modules to improve process effectiveness. The base pressure and deposition pressure for the process was about $2x10^{-2}$ torr and $8.1x10^{-1}$ torr respectively.

5.3.2 Process Flow of Photo-assisted MOCVD

A typical process flow of Cu_2O thin film deposition is shown in Figure 5.2. First of all, the n-type <100> Si wafer was cleaned ex-situ in diluted HF solution for one minute and then, loaded into the deposition chamber. The substrate was cleaned in-situ in 20 standard cubic centimeter (sccm) flow of forming gas (20% UHP H_2 and 80% UHP N_2) at 900 ºC for five minutes. Copper precursor was heated in vacuum at 140 ºC. After in-situ cleaning, the substrate was brought to the deposition temperature of 750 ºC; using 200 sccm of UHP N_2 the deposition process was performed for 60 minutes. In addition, N_2O and UHP O_2 were supplied at 80 sccm during the deposition. After deposition, the substrate was allowed to cool to room temperature in vacuum. The UV light source was kept on during in-situ cleaning and the deposition process. The same process was also used to deposit Cu_2O thin-film on p-Si and quartz substrates. Only for quartz substrate, the substrate was ex-situ cleaned using RCA cleaning instead of HF cleaning. The deposited film on silicon substrates was uniform in one centimeter diameter due to

limitation of nozzle position in our experimental setup. All the measurements were done on this one centimeter diameter circle.

5.3.3 Characterization Details

X-ray diffraction (XRD) measurements were performed on the as-grown films as well as on clean substrate materials using an angle dispersive diffractometer (Rigaku Ultima IV) with monochromatic Cu-Kalpha (λ = 1.540 Å) radiation at 40 kV. XRD data were collected at a rate of 1.2º 2Θ per minute in 0.2º 2Θ steps. An optical reflectance spectrum of Cu_2O film deposited on a quartz wafer was obtained by using a PC-controlled Shimadzu UV-3101 UV−Vis-NIR spectrometer equipped with an integrating sphere. A blank quartz wafer was used as a reflectance standard. The UV−Vis-NIR diffuse reflectance spectrum of the blank quartz wafer and the Cu_2O-coated wafer were acquired in the range of 250 nm (5 eV) to 2100 nm (0.6 eV) in reflectance (%R) mode. Absorption data was calculated from the reflectance data using the Kubelka-Munk function [28]. The thickness of Cu_2O thin film was measured with a DekTak III profilometer with software package version 1.2. To prepare cross-section TEM samples, Argon ion milling procedure was utilized with incidence angle of 3 degrees at 3 KeV. A JEOL-2010F field emission TEM was used to study the microstructure and determine crystal structure by selected-area diffraction techniques.

For electrical characterization measurements, aluminum and gold metal dots were evaporated as back and front contact respectively on both n-Si and p-Si devices. Prior to evaporating the gold front contact, the aluminum contact was sintered at 475 ºC for 20

minutes in a nitrogen environment to form an ohmic contact to silicon. After sintering the back ohmic contact, 1.0 mm diameter gold dots were evaporated as front metal contact to Cu_2O. The area of the device was measured to be equal to 0.00785 cm^2. A Kiethely 4200 Semiconductor Characterization System was used to perform current-voltage measurement.

5.4 Results and Discussion

5.4.1 XRD of Cu_2O Thin-film

The XRD analysis of the films deposited by photo-assisted MOCVD is shown in Figure 5.3. The X-ray data indicate that highly crystalline Cu_2O films were deposited on both quartz and Si substrates. In general, we note a preferred orientation, as (200)-oriented crystals, occurs on both substrates. This is similar to Cu_2O films more commonly grown on c-axis ZnO by MOCVD [29] and others grown by sputtering techniques [30], but a departure from the (111) oriented films typically grown by electrochemical means [31]. A small polycrystalline contribution from (111)-oriented crystals is observed for our films grown on the quartz substrate, but it is not the primary orientation. In the case of the Si substrate, a very small amount of CuO is formed, and (111) Cu_2O is not observed. There is a broad weak silicon peak at 2θ equal to 33 degrees for Cu_2O/n-Si device due to about 150 nm thick Cu_2O film.

5.4.2 Energy Gap of Cu_2O Thin-film

Figure 5.4(a) shows absorbance spectra of Cu_2O thin-film deposited on a 2" quartz wafer. To calculate the optical band gap of the Cu_2O thin film, Tauc's relationship is used which is given by $\alpha \cdot h\nu = \alpha_0 (h\nu - E_g)^n$, where, α is absorption coefficient, hν is photon energy, α_0 is a constant, E_g is the band gap, and n is 0.5 for a direct band gap material [32]. Further, absorption coefficient of the Cu_2O thin film is given by α = 2.303 (A/d), where d is the thickness of the film and A is optical absorbance [33]. The thickness of the Cu_2O film on quartz was about 15 nm as measured with the DekTak profilometer. As shown in Figure 5.4(b), the optical band gap is estimated by extrapolating the linear portion of $(\alpha \cdot h\nu)^2$ vs. hν plot to the hν axis. According to this analysis, the estimated band gap of the film was 2.44 eV on quartz substrate.

5.4.3 Transmission Electron Microscopy

The Cu_2O film grows as in the form of three-dimensional islands by Volmer-Weber growth on SiO_2/Si(100) substrate, as shown in Figure 5.5. This growth mode requires: σ_s(low) < σ_f (low) + σ_{sf} (high), where (σ_s) is the free energy of the substrate, (σ_f) is the free energy of the film, and (σ_{sf}) is the interfacial energy. Figure 5.6 shows the size distribution with islands in the size range of 100-200 nm. The microstructure of these grains shows that these islands are composed of smaller nanocrystlline grains in the range of 10-20 nm contain some defects and their clusters, as shown in the bright-field and dark-field images of Figure 5.7. The corresponding selected-area diffraction pattern shows spots from Si <110> orientation and faint rings from nanocrystalline Cu_2O film. In

which, the bright spots correspond to Si substrate, while the faint ring corresponds to the polycrystalline Cu_2O film.

5.4.4 Secondary Ion Mass Spectrometry Analysis

Figure 5.8 shows the depth profile of SIMS of the Cu_2O films grown on Si and SiOx/Si substrate marked as C041 and C042 respectively, with the depth in micron as the abscissa and the normalized signal intensity as the ordinate. It is difficult to conclude from the data whether the apparent diffusion of Cu and O into the Si is real or a function of the film's roughness limiting the depth resolution. It also seems that the SiO_x barrier layer had no effect upon the diffusion. Of course, it is also possible that Cu and O tail into the Si substrate is from poor depth resolution.

5.4.5 Cu_2O-Si Hetrojunction Electrical Characterstics

In this section, the electrical characterization of Cu_2O/nSi devices fabricated under various processing conditions are described. To begin with, a sample without Cu_2O film was prepared and current density-voltage (J-V) characteristics were measured to verify Schottky junction formation between gold and the silicon substrate. Figure 5.9 shows that Cu_2O-nSi device has leakage current five orders magnitude lower than Au-nSi Schottky diode. This effect can only result from the high quality interface between the two materials i.e. Cu_2O/nSi. Figure 5.10 shows dark J-V characteristics of Cu_2O/n-Si devices fabricated at 750 ºC, 700 ºC and 650 ºC. The device fabricated at 750ºC shows the lowest dark leakage current as compared to devices deposited at 700 ºC and 650 ºC.

Therefore, 750 ºC was chosen as the deposition temperature for rest of the work. To see the effect of annealing on Cu_2O/n-Si devices, the devices fabricated at 750 ºC were annealed in a nitrogen environment at 500ºC for various time intervals. Figure 5.11 shows that the dark leakage current density of the devices remains relatively unchanged for 5 and 10 minutes annealing and adverse results are obtained for 20 minutes annealing time. Based on the results of Figure 5.11, annealing was not included in the optimum cycle. As shown in Figure 5.12, the Cu_2O thin film was also deposited on the p type silicon wafer. The electrical characteristic for Cu_2O/p-Si device is found to be ohmic. The lowest leakage current density at zero bias is 1.5×10^{-12} A/cm^2 for the Cu_2O/n-Si device which is an indicator of low surface recombination velocity (SRV).

Four samples were fabricated using optimal processing parameters described in the experimental section. Four dots were measured on each sample to determine descriptive statistics for leakage current density at zero bias. A 95% prediction interval for absolute value of the leakage current density at zero bias lies between 0.54×10^{-12} and 12.08×10^{-12} A/cm^2. While, 95% confidence interval for absolute value of the leakage current density at zero bias lies between 4.86×10^{-12} and 7.74×10^{-12} A/cm^2. We have also compared our dark J-V characteristics with the results reported in the literature [34, 35]. As shown in Figure 5.13, our dark J-V is many orders of magnitudes lower than data reported in the literature. Our results showing lower dark leakage current indicates low defect density of Cu_2O films and suitability for potential PV applications. Use of high

purity precursor (99% purity precursor used in this study) will further reduce the defects of copper oxide films and improve the device electrical characteristics.

5.5 Conclusion

Cu_2O thin films have been deposited on n-type and p-type silicon substrates. Cu_2O/n-Si device shows a rectifying junction behavior while Cu_2O/p-Si shows ohmic current-voltage characteristics. The XRD analysis revealed a single major peak of Cu_2O. Based on UV-Vis-NIR spectroscopy measurements, the calculated optical band gap is about 2.44 eV. TEM spectroscopy showed nanocrystalline growth of the film. Electrical characterization of Cu_2O/nSi devices showed the lowest leakage current density at zero bias of 1.5×10^{-12} A/cm^2 which is a major indicator of low surface recombination velocity and indicates the potential of photovoltaic material.

References

[1] "Solar markets: Overall growth & size by country", Avaialable: http://solarcellcentral.com/markets_page.html, June, 2012.

[2] R. Singh and J. D. Leslie, "Economic requirements for new materials for solar photovoltaic cells", Solar Energy, vol. 24, no. 6, pp. 589-592, 1980.

[3] M. A. Green, "The Path to 25% Silicon Solar Cell Efficiency: History of Silicon Cell Evolution", Prog. Photovolt. Res. Appl., vol. 17, issue 3, pp. 183-189, 2009.

[4] Z. Wang, P. Han, H. Lu, H. Qian, L. Chen, Q. Meng, N. Tang, F. Gao, Y. Jia, J. Wu, Y. Fei, W. Wu, H. Zhu, J. Ji, Z. Shi, A. Sugianto, L. Mai, B. Hallam, and S. Wenham, "Advanced PERC and PERL production cells with 20.3% record efficiency for standard commercial p-type silicon wafers", Prog. Photovolt. Res. Appl., vol. 20, issue 3, pp. 260-268, 2012.

[5] R. Singh and G. F. Alapatt, " Innovative Paths for Providing Green Energy by the Use of Photovoltaics for Sustainable Global Economic Growth", Proc. SPIE conference on Innovation, 2012, In Press.

[6] R. Singh, N. Gupta and K. F. Poole, "Global green energy conversion revolution in 21st century through solid state devices", Proc. 26th International Conference on Microelectronics, Nis, Serbia, May 11-14, 2008, vol. 1, pp. 45-54, IEEE, New York, NY.

[7] R. Singh, "Why Silicon is and Will Remain the Dominant Photovoltaic Material", Journal of Nanophotonics, vol. 3, issue 01, article no. 032503, 2009.

[8] R. Singh, G. F. Alapatt and K. F. Poole, "Photovoltaics: Emerging role as a dominant electricity generation technology in the 21st century", Proc. 28th International Conference on Microelectronics, Nis, Serbia, May 13-16, 2012, pp. 53-63, IEEE, New York, NY.

[9] "Abundance of elements in Earth's crust", Available: http://en.wikipedia.org/wiki/Abundance_of_elements_in_Earth's_crust.

[10] W. Shockley and H. J. Queisser, "Detailed balance limit of efficiency of p-n junction solar cells," J. Appl. Phys., vol. 32, issue 3, pp. 510, 1961.

[11] S. B. Ogale, P. G. Bilurkar, N. Mate, S. M. Kanetkar, N. Parikh and B. Patnaik, "Deposition of copper oxide thin films on different substrates by pulsed excimer laser ablation", J. Appl. Phys., vol. 72, issue 8, pp. 3765, 1992.

[12] J. F. Pierson, A. Thobor-Keck and A. Billard, "Cuprite, paramelaconite and tenorite films deposited by reactive magnetron sputtering", Appl. Surf. Sci., vol. 210, issue 3-4, pp. 359-367, 2003.

[13] B. Balamurugan and B. R. Mehta, "Optical and structural properties of nanocrystalline copper oxide thin films prepared by activated reactive evaporation", Thin Solid Films, vol. 396, issue 1-2, pp. 90-96, 2001.

[14] L. C. Olsen, F. W. Addis and W. Miller, "Experimental and theoretical studies of Cu2O solar cells", Solar Cells, vol. 7, issue 3, pp. 247-279, 1982.

[15] E. Kennard and E. Dieterich, “An effect of light upon the contact potential of selenium and cuprous oxide”, Physical Review, vol. 9, no. 1, pp. 58-63, 1917.

[16] F. Biccari, “Defects and doping in Cu2O”, Ph.D. dissertation, Dept. of Physics, Sapienza – University of Rome, Rome, Italy, Dec. 2009.

[17] A. Mittiga, E. Salza, F. Sarto, M. Tucci and R. Vasanthi, “Heterojunction solar cell with 2% efficiency based on a Cu2O substrate”, Appl. Phys. Lett., vol. 88, no. 16, article no. 163502, 2006.

[18] M. F. Jawad, R. A. Ismail and K. Z. Yahea, “Preparation of nanocrystalline Cu2O thin film by pulsed laser deposition”, J. Mater. Sci. : Mater. Electron., vol. 24, no. 9, pp. 1244-1247, 2011.

[19] T. Maruyama, “Copper oxide thin films prepared by chemical vapor deposition from copper dipivaloylmethanate”, Solar Energy Mater. Solar Cells, vol. 56, no. 1, pp. 85-92, 1998.

[20] J. A. Switzer, R. Liu, E. W. Bohannan and F. Ernst, “Epitaxial electrodeposition of a crystalline metal oxide onto single-crystalline silicon”, The Journal of Physical Chemistry B, vol. 106, no. 48, pp. 12369-12372, 2002.

[21] L. S. Huang, S. G. Yang, T. Li, B. X. Gu, Y. W. Du, Y. N. Lu and S. Z. Shi, “Preparation of large-scale cupric oxide nanowires by thermal evaporation method”, J. Cryst. Growth, vol. 260, no. 1-2, pp. 130-135, 2004.

[22] S. Ghosh, D. K. Avasthi, P. Shah, V. Ganesan, A. Gupta, D. Sarangi, R. Bhattacharya and W. Assmann, “Deposition of thin films of different oxides of copper by RF reactive sputtering and their characterization”, Vacuum, vol. 57, no. 4, pp. 377- 385, 2000.

[23] R.Singh and V. Parihar, ”Rapid Photothermal Processing (RPP) of Dielectrics”, Chapter of the Hand book of Low and High Dielectric Constant Materials and Their Applications, edited by H. S. Nalwa, published by Academic Press, Vol. 2, 1999, pp. 1- 59.

[24] R. Singh, S. V. Nimmagadda, V. Parihar, Y. Chen and K. F. Poole, “Role of rapid photothermal processing in process integration”, IEEE Trans. Electron Devices, vol. 45, issue 3, pp. 643-654, 1998.

[25] S. Venkataraman, R. Singh, V. Parihar, K.F. Poole, and A. Rohatgi, “Effect of Ultraviolet and Vacuum Ultraviolet Photons in Rapid Photothermal Processing on the Minority Carrier Life Time of Silicon Wafers”, J. Electronic Mat., vol. 26, pp. 1394-1398, 1999.

[26] A. Venkateshan, R. Singh, K. F. Poole, J. Harriss, H. Senter, R. Teague and J. Narayan, “High- gate dielectrics with ultra-low leakage current for sub-45 nm CMOS”, Electron Lett., vol. 43, no. 21, pp. 1130, 2007.

[27] S. Shishiyanu, R. Singh, T. Shishiyanu, S. Asher and R. Reedy, “The Mechanism of Enhanced Diffusion of Phosphorus in Silicon During Rapid Photothermal Processing of Solar Cells”, IEEE Transaction of Electron Devices, vol. 58, pp. 776-781, 2011.

[28] G. Kortüm, W. Braun, and G. Herzog, “Principles and Techniques of Diffuse-Reflectance Spectroscopy”, Angew. Chem. Int. Ed. Engl., vol. 2, pp. 333-404, 1963.

[29] S. Jeong and E. S. Aydil, “Heteroepitaxial growth of Cu2O thin film on ZnO by metal organic chemical vapor deposition”, J. Cryst. Growth, vol. 311, issue 17, pp. 4188-4192. 2009.

[30] K. Akimoto, S. Ishizuka, M. Yanagita, Y. Nawa, G. K. Paul and T. Sakurai, “Thin film deposition of Cu2O and application for solar cells”, Solar Energy, vol. 80, issue 6, pp. 715-722. 2006.

[31] M. Izaki, T. Shinagawa, K. Mizuno, Y. Ida, M. Inaba and A. Tasaka, “Electrochemically constructed p-Cu2O/n-ZnO heterojunction diode for photovoltaic device”, J. Phys. D, vol. 40, issue 11, pp. 3326-3329, 2007.

[32] J. Tauc, R. Grigorovici and A. Vancu, “Optical properties and electronic structure of amorphous germanium”, Physica Status Solidi (b), vol. 15, issue 2, pp. 627-637, 1966.

[33] H. M. Pathan, J. D. Desai and C. D. Lokhande, "Modified chemical deposition and physico-chemical properties of copper sulphide (Cu2S) thin films", Appl. Surf. Sci., vol. 202, issue 1-2, pp. 47-56, 2002.

[34] F. Drobny, and D. Pulfrey, "The photovoltaic properties of thin copper oxide films," 13th IEEE Photo-voltaic Specialists Conference- 1978, Washington, DC, USA, 180, 1978.

[35] R.A. Ismail, "Characteristics of p-Cu2O/n-Si Heterojunction Photodiode made by Rapid thermal Oxidation", J. of Semiconductor Technology and Science, vol. 9, pp. 51-54, 2009.

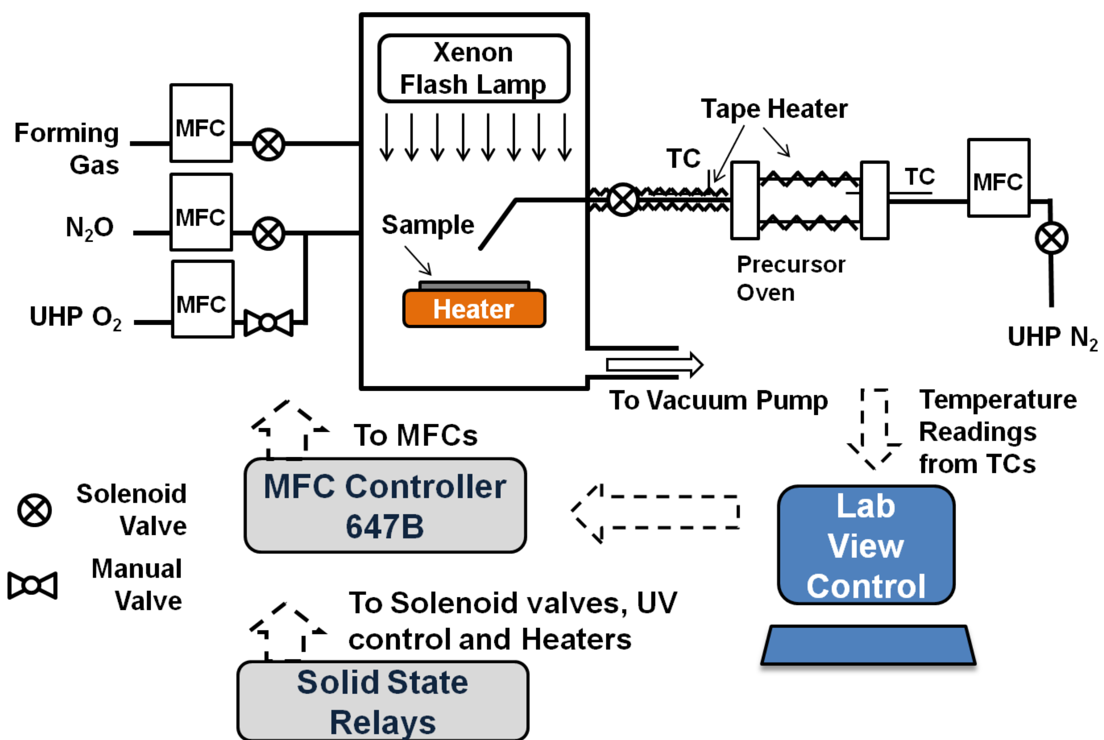

Figure 5.1: Experimental set up of MOCVD system used for in-situ cleaning, deposition and in-situ annealing of Cu_2O films.

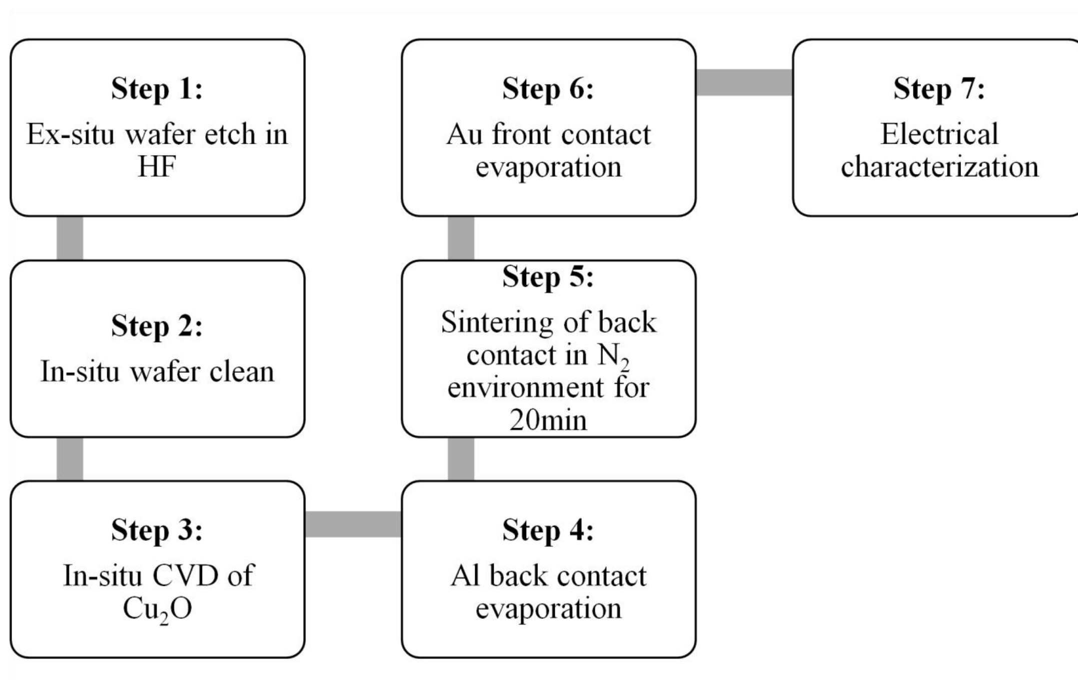

Figure 5.2: Process flow for the deposition of Cu_2O thin films on silicon and quartz substrates.

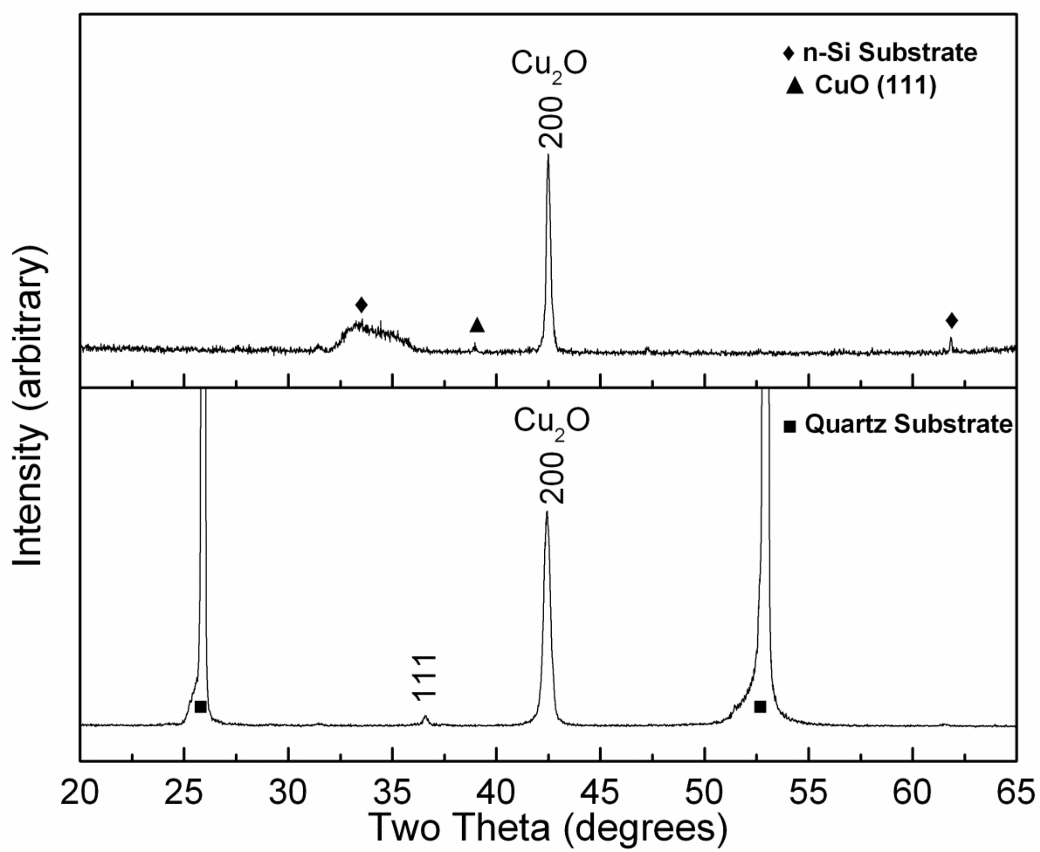

Figure 5.3: XRD pattern of the Cu_2O films deposited on n-Si substrate (Top) and Quartz substrate (Bottom).

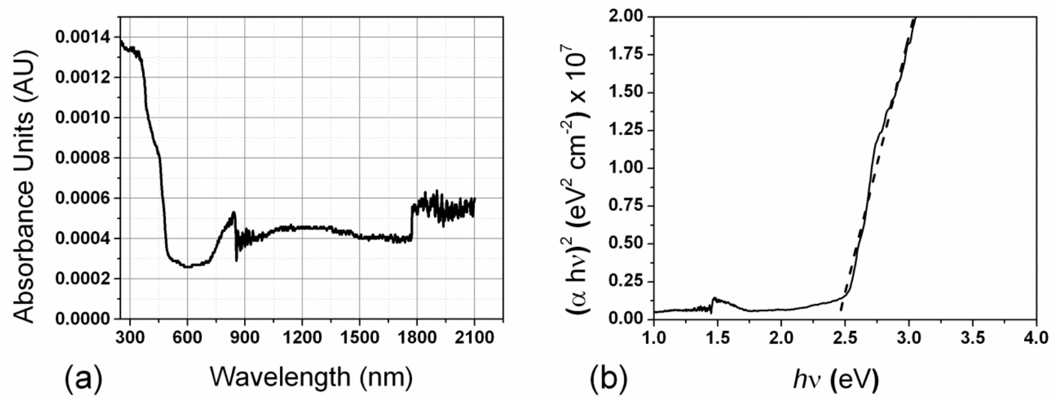

Figure 5.4: (a) Absorbance spectra of Cu_2O thin film deposited on quartz wafer; (b) $(\alpha \cdot h\nu)^2$ vs. energy plot for optical band gap calculations.

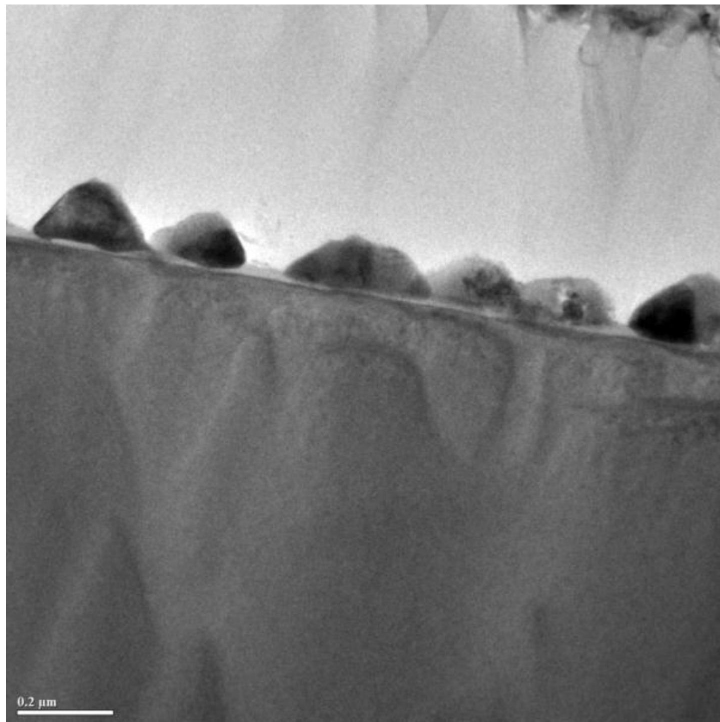

Figure 5.5: Bright-field Cross-section TEM image of the individual islands.

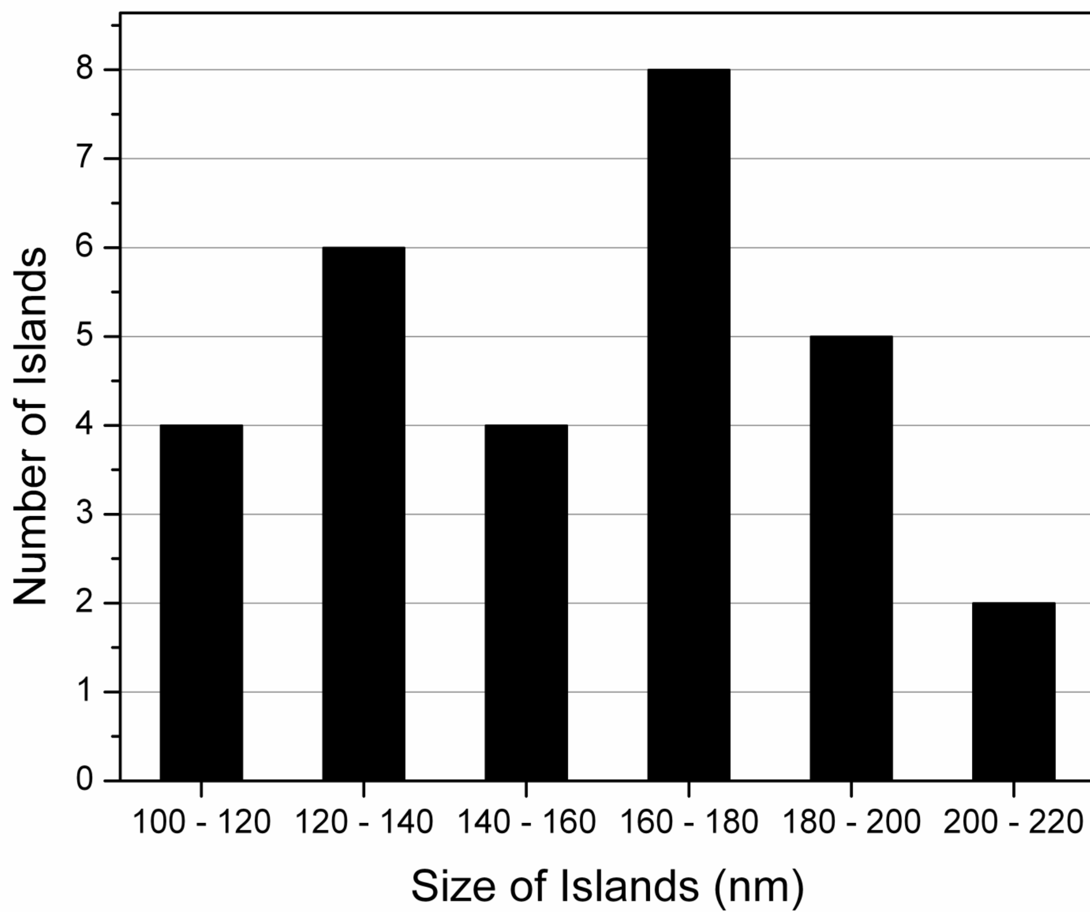

Figure 5.6: Size distribution Cu_2O islands/grains.

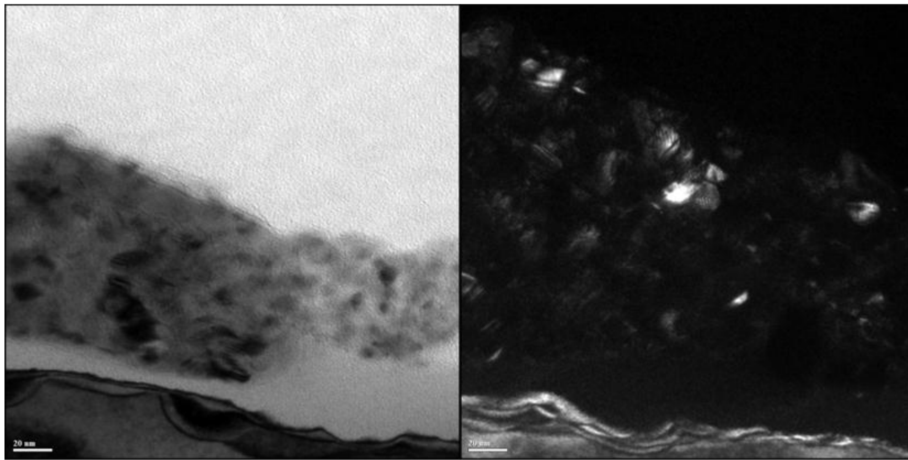

(a) (b)

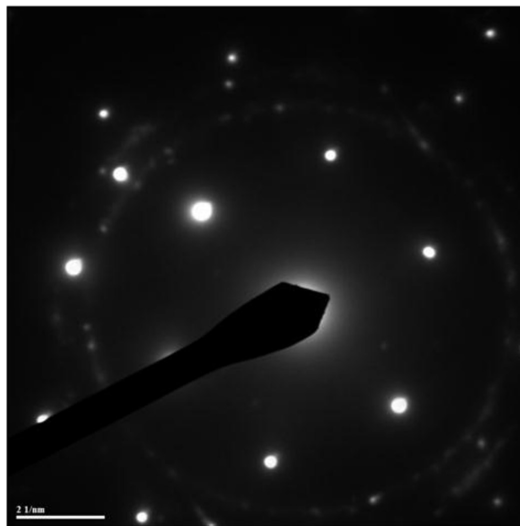

(c)

Figure 5.7: Polycrystalline grains: (a) cross-section bright-field; (b) cross-section dark-field; and (c) selected-area diffraction pattern.

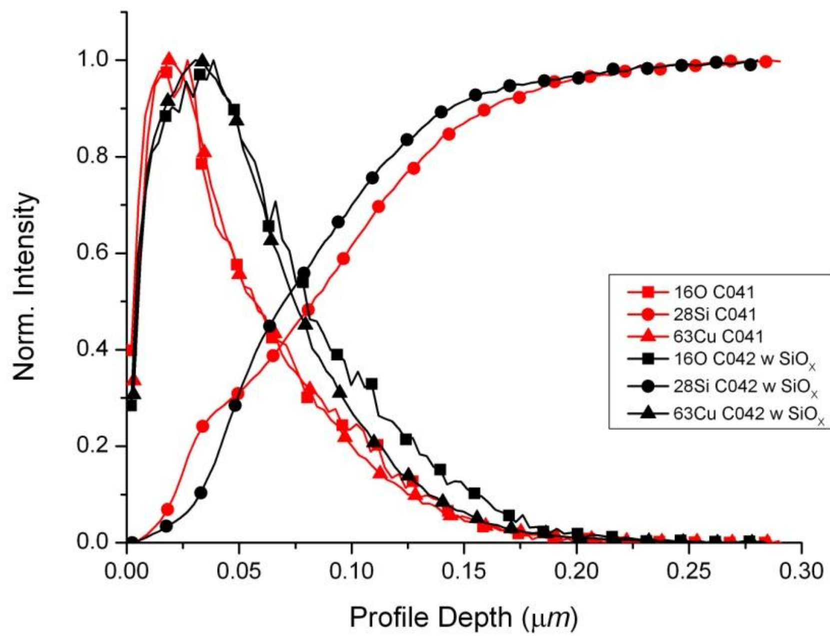

Figure 5.8: Normalized SIMS depth profile for CO41 and C042 devices

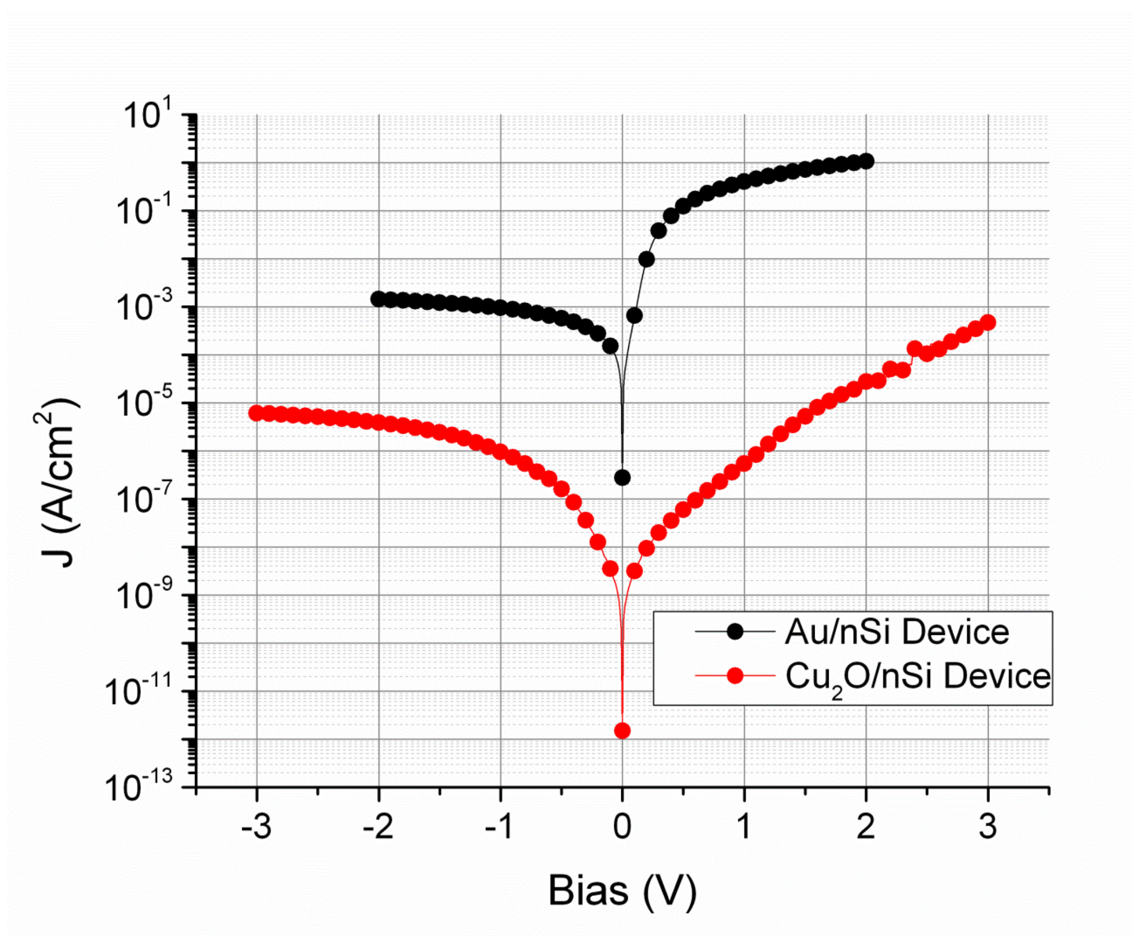

Figure 5.9: Comparison of J-V characteristics of Au-nSi device (Schottky diode) and Cu_2O-nSi device.

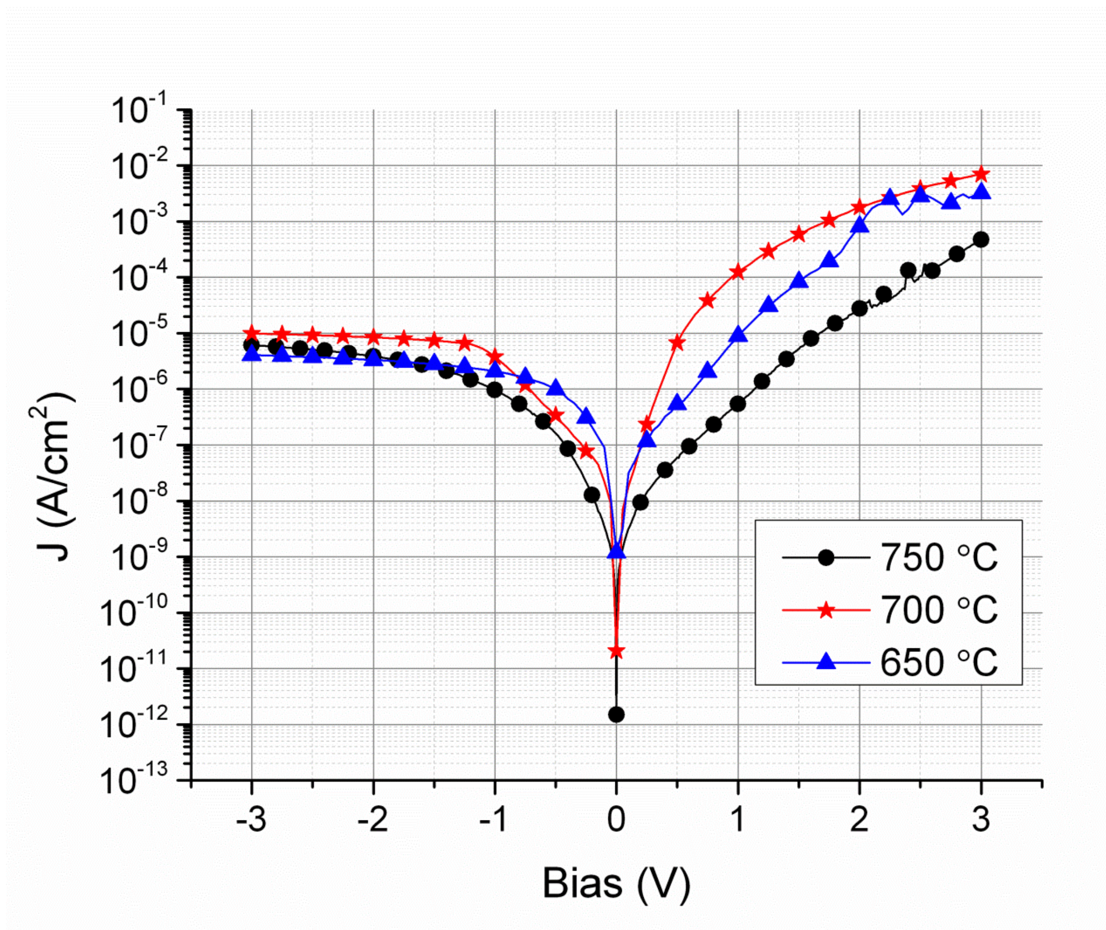

Figure 5.10: Current density-voltage (J-V) characteristics of Cu_2O/n-Si devices deposited at various substrate temperatures.

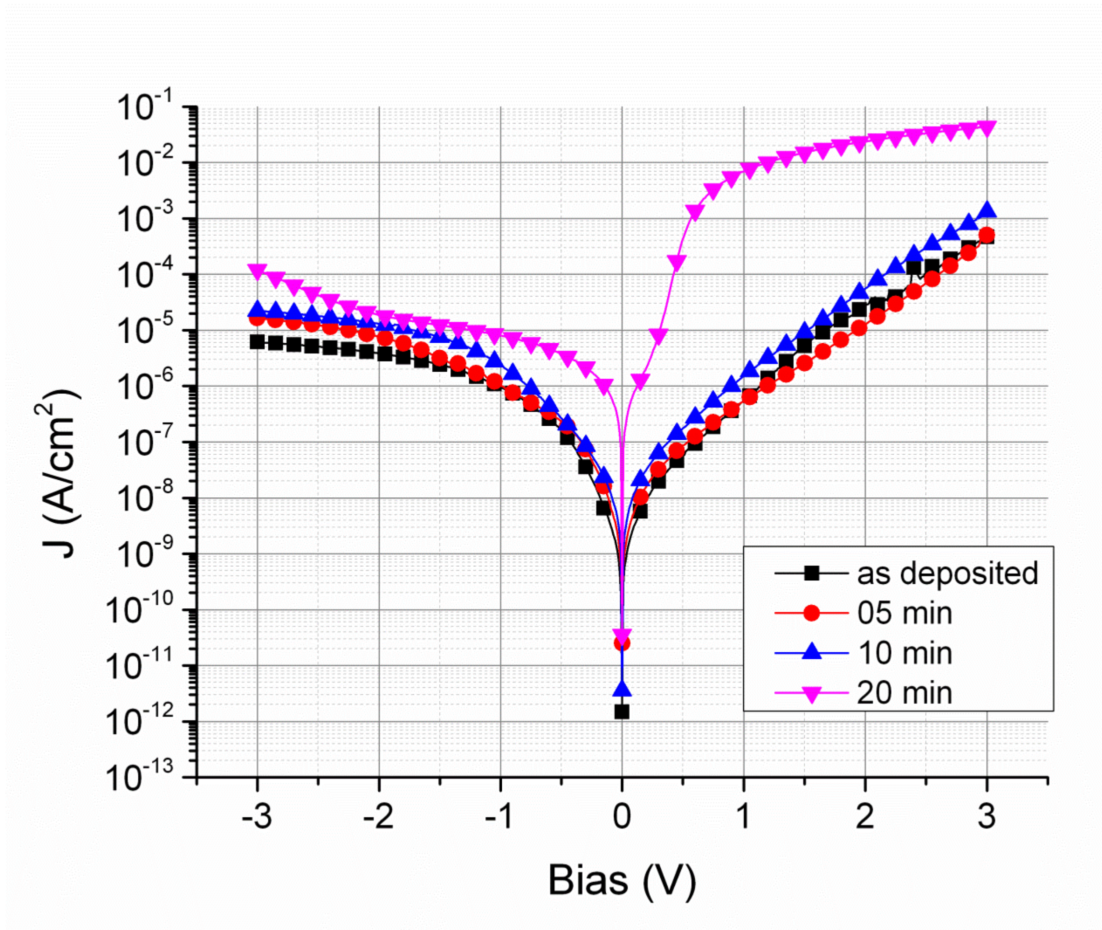

Figure 5.11: Effect of annealing time on J-V characteristics of Cu_2O/n-Si devices deposited at 750ºC and annealed in-situ at 500ºC.

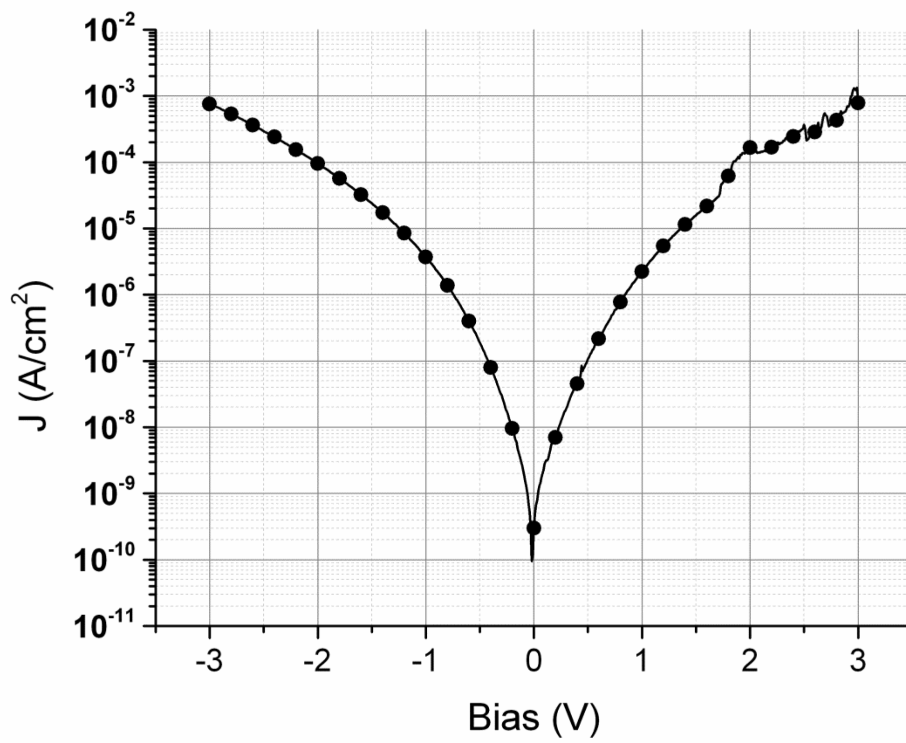

Figure 5.12: J-V characteristic of the Cu_2O/p-Si diode.

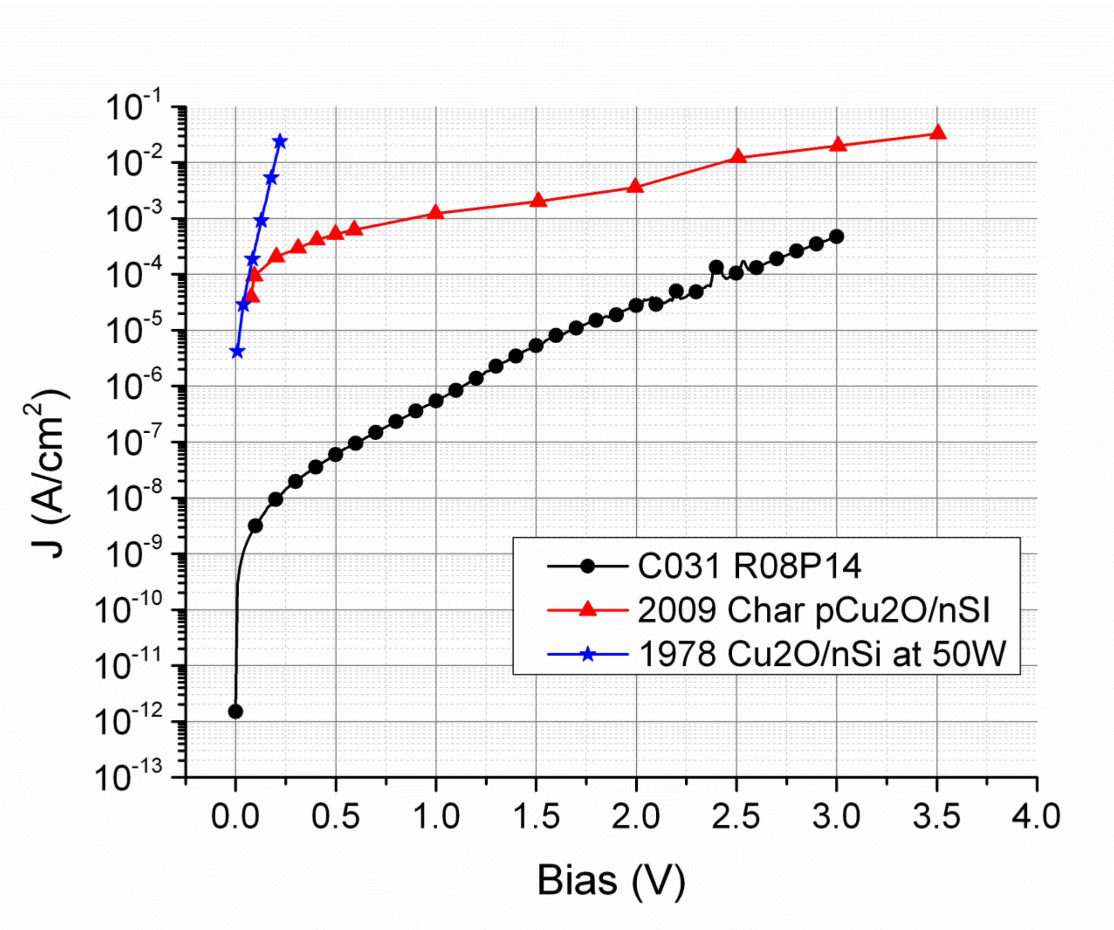

Figure 5.13: Comparison of dark J-V characteristics of Cu_2O/n-Si diodes literature data [34, 35] and present work.

CHAPTER SIX

CONCLUSION

A photo-assisted thermal processing system is developed and used to processed semiconductor core fiber and thin-films of dielectric and semiconductor materials. Single crystal x-ray diffraction, Raman spectroscopy and Schottky diodes have revealed that ex-situ rapid photothermal annealing is shown to enhance the structural homogeneity of silicon optical fibers. Photons in UV and VUV regions play an important role in improving the bulk and surface carrier transport properties of RPP treated silicon fibers. Optimization of annealing parameters can further improve the structural homogeneity of silicon fibers thereby further advancing their optoelectronic performance and moving semiconductor core optical fiber technology closer to practical device implementation.

CCTO thin film has been deposited on the Si/SiO_2 substrate using a photo-assisted MOCVD process in a custom designed non-commercial automated system. The process was optimized by controlling the flow rate of precursors, process temperatures, and deposition time. The optimized process still had some impurities of rutile TiO_2 and Cu_2O, but high energy photon assisted MOCVD has showed CCTO grains with grain sizes as large as 410 nm. The CCTO film has been characterized with ellipsometry, powder XRD, and SEM techniques. Ellipsometry indicates the refractive index of the film is 3.03±0.06.

Cu_2O thin films have been deposited on n-type and p-type silicon substrates. Cu_2O/n-Si device shows a rectifying junction behavior while Cu_2O/p-Si shows ohmic

current-voltage characteristics. The XRD analysis revealed a single major peak of Cu_2O. Based on UV-Vis-NIR spectroscopy measurements, the calculated optical band gap is about 2.44 eV. TEM spectroscopy showed nanocrystalline growth of the film. Electrical characterization of Cu_2O/nSi devices showed the lowest saturation current density at zero bias of $1.5x10^{-12}$ A/cm^2.

The significance of this work is that a custom designed non-commercial automated photo-assisted thermal processing system is developed for in-situ cleaning, deposition and annealing of various semiconductor devices and materials. The developed system has the advantage of lower processing cost, higher throughput, and improved device performance with ease to be integrated within manufacturing line. The present system can be further used for processing and development of various novel materials and devices.

APPENDIX A

LABVIEW AUTOMATION

A.1 Introduction

The system used in this work was automated with LabView. In order to automate the system with LabView, a low cost NI PCI-6025E multifunction I/O board and NI-DAQ for Win 2000/NT/9x was used with SH1006868 shielded cable assembly and split 100-pin to two 68-pin shielded cable connectors. All LabView modules were developed in LabView 8.2. LabView was used to control individual valves and cycles. All the solenoid and pneumatic valves were connected through LabView and SCC-68 breakout box to solid state relays. A solid state relay operates as a switch which is controlled with a binary control signal sent by LabView module. Since there is no moving part involved, it provides quick response, no wear-n-tear and long operational life. Following LabView modules were developed to control processes developed in this work.

A.2 The Ultimate Reader with Control VI

Figure AX.1 shows the front panel of the ultimate reader with control VI. The function of this VI read all the thermocouples associated in the system. This VI reads all the thermocouple by running a task and store in respective global variables in order to provide current temperature to oven heater VIs. The reason behind to read thermocouples simultaneously using a single task is that LabView is not able to initiate overlapping read command for analog inputs. The entire analog read command has to be done all together

using the same task. The same VI also provides temperature monitoring and on-off control to the oven heaters. This is very helpful when multiple ovens are being used in the process like CCTO deposition.

A.3 Delivery Line And Oven Temperature Control VIs

Temperature of delivery line and precursor oven heaters was controlled by Oven temperature control VIs which uses a real time automatic proportional–integral–derivative controller (PID controller) and generates pulse width modulated (PWM) output. The pulse generated by PID controller based with feedback, is sent to the solid state relay through SCC 68 box. Each tape heater wrapped on oven heater and delivery line is connected to a solid state relay. Figure AX.2 shows front panel of a typical temperature control VI. One can input desired set point directly on the front panel of the VI. As described in the last section, all the temperature control Vis can be controlled by the ultimate reader with control VI. It is important that the ultimate reader with control VI should be running before temperature control VIs. Also, the temperature control VIs should be stopped by using switch on the front-panel. The stop switch reset the VI and put all the outputs to zero.

A.4 UV Control with Timer.VI

UV control with timer VI was used in cleaning cycle of the processes. VI controls the UV lamp with an incorporated timer within the VI. Figure AX.3 shows front panel of

the VI. The desired UV lamp ON time in seconds can be entered on the front panel. After running the VI, the UV control switch is used in order to turn ON the lamp power supply.

A.5 Deposition Cycle VI

Deposition cycle VI were developed to automate the process of deposition. This VI controls solenoid and pneumatic valves, UV lamp and MFCs required in the process. The desired deposition time in seconds can be entered on the front panel of the VI as shown in Figure AX.4. Also, it is worth noting that the user needs to enter desired gas flow rates of the gases except for oxygen (CH04) on the 647B multi gas controller itself. Desired flow rate for oxygen (CH04) can be entered in the block diagram of the VI. Two separate VIs were developed for CCTO and Cu_2O deposition. Since there are few manual valves are also used in the system, therefore it is important two open those before the deposition cycle. To remind this, VI prompts the user open those manual required in the process.

A.6 O_2 Annealing with UV Control VI

In CCTO thin-film deposition, CCTO film was annealed in O_2 environment. To automate annealing cycle, the deposition cycle VI was modified to develop O_2 annealing with UV control VI. Figure AX.5 shows front panel of O_2 annealing with UV control VI. Similar to deposition cycle VI, this VI also prompts user to open O_2 manual valve and UV cooling line valve. User can input the desired annealing time on the front panel of the VI.

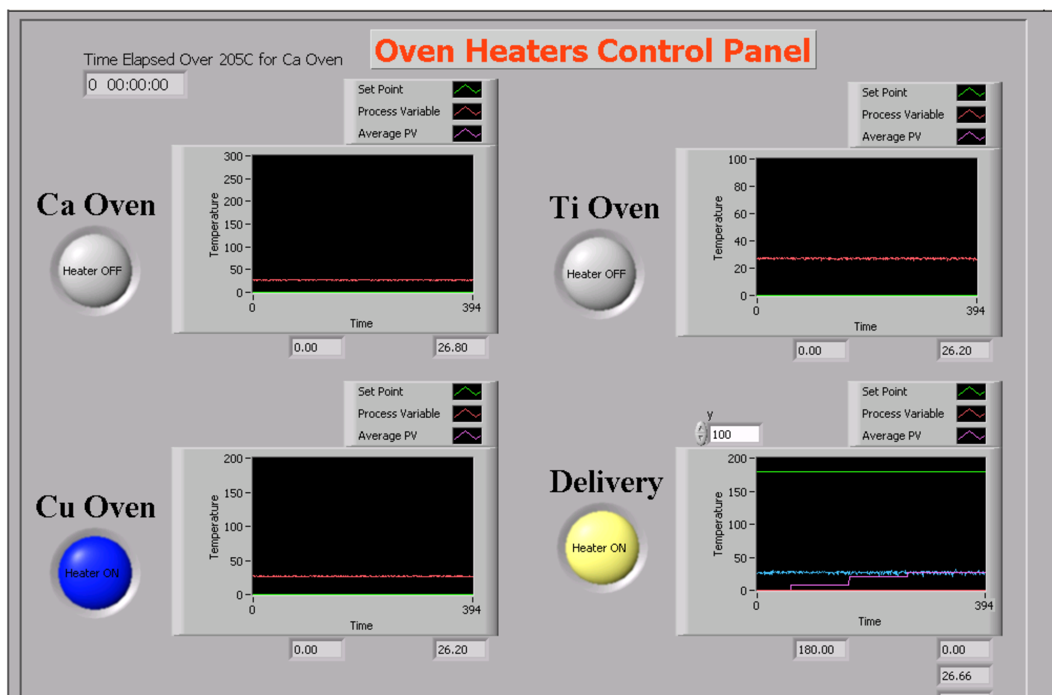

Figure AX.1: Front panel of the ultimatereaderwithcontrol.vi

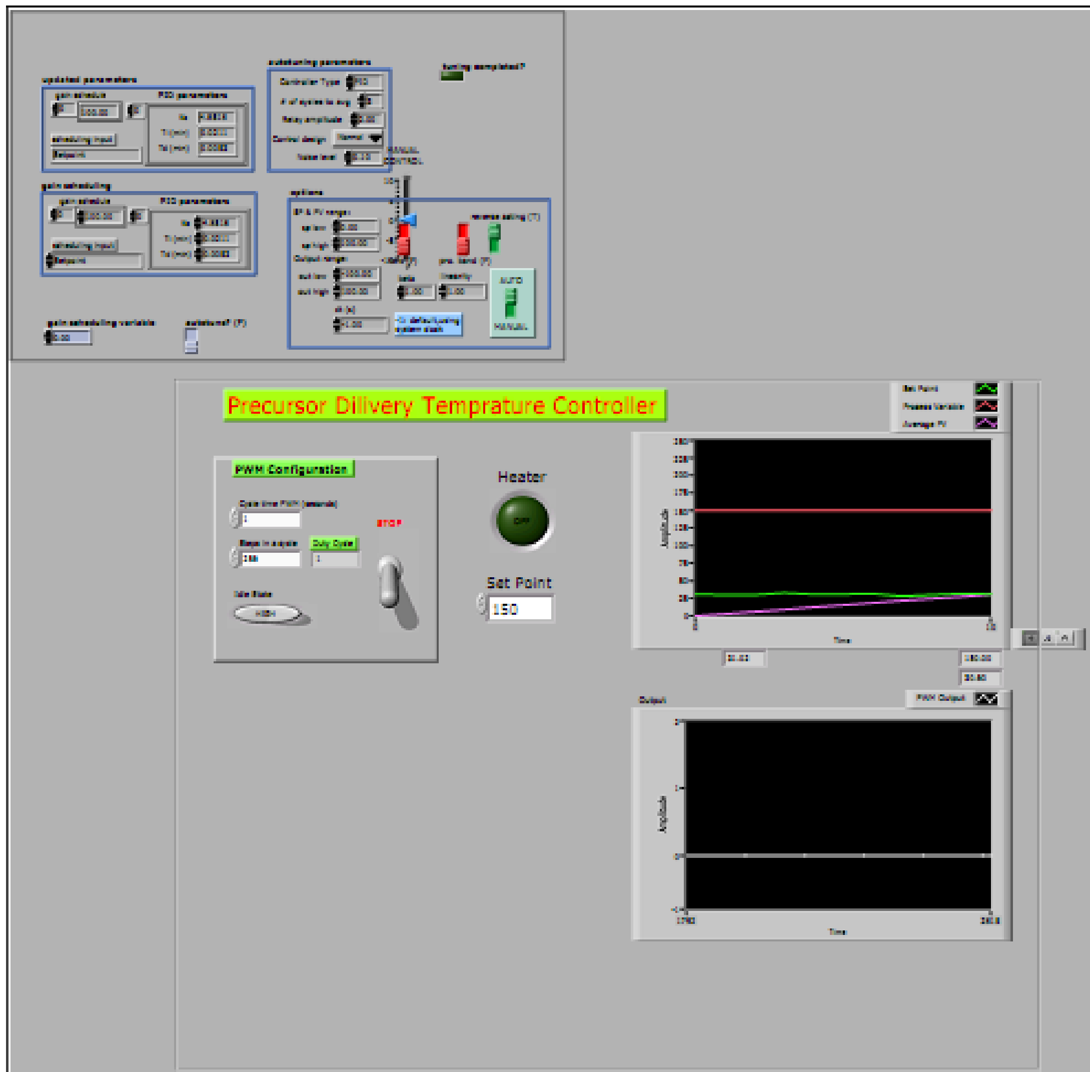

Figure AX.2: Front panel of precursor delivery line heater control VI

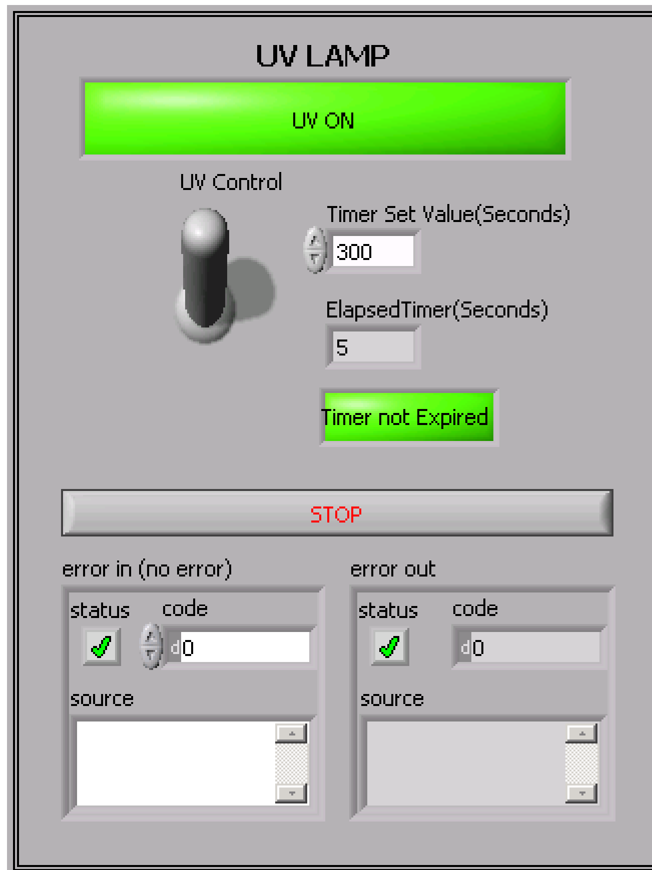

Figure AX.3: Front panel of UV lamp control with timer VI

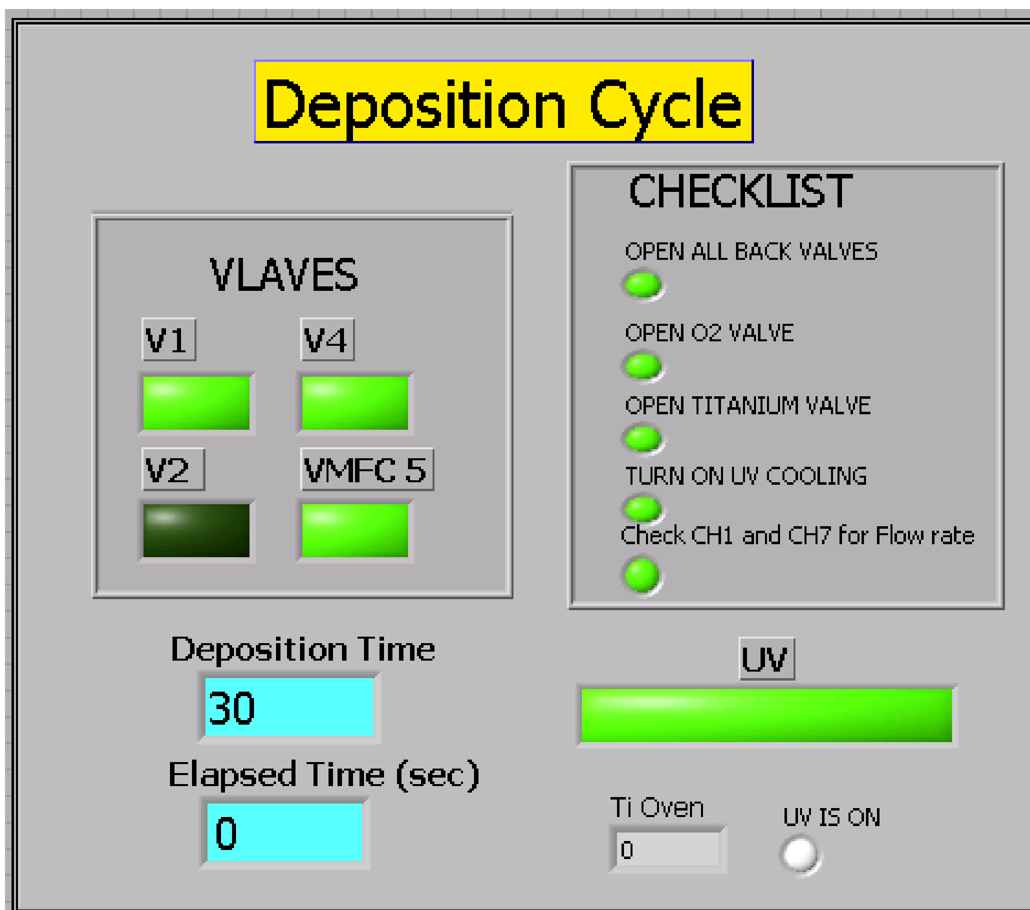

Figure AX.4: Front panel of precursor deposition cycle VI for CCTO and Cu_2O

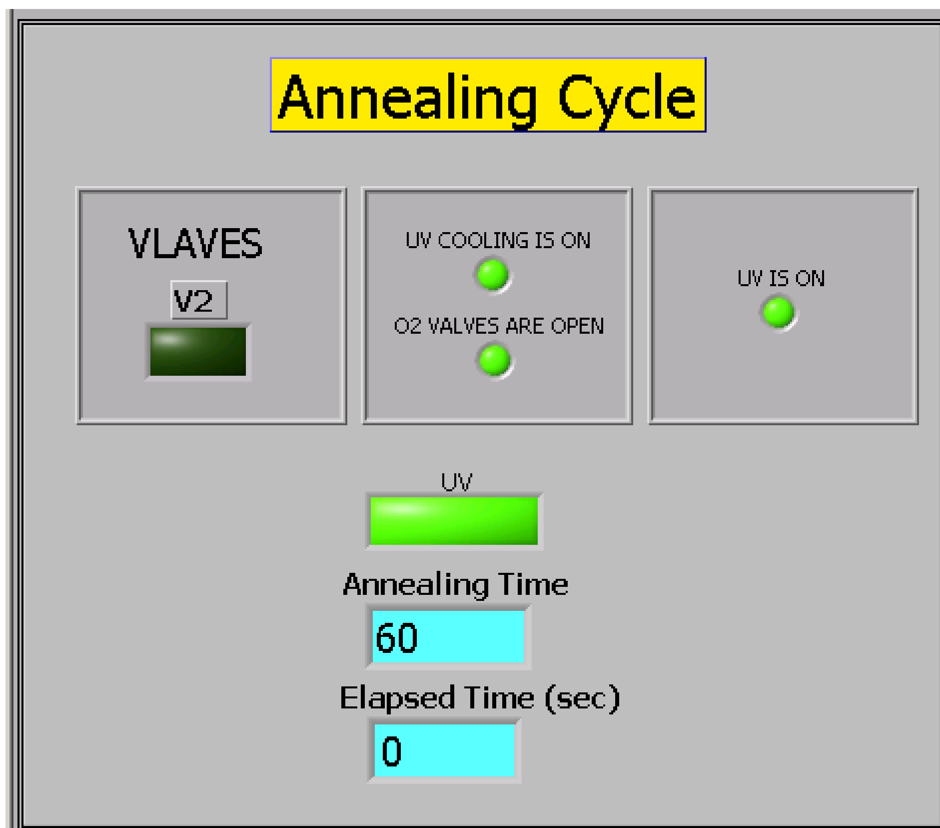

Figure AX.5: Front panel of oxygen annealing VI